SPECIMEN THESIS TITLE PAGE

Development of novel hybrid method and geometrical configuration-based active noise control system for circular cylinder and slat noise prediction and reduction applications

Tongrui Peng

A thesis submitted in partial fulfilment of the requirements of the University of the West of England, Bristol for the degree of *Doctor of Philosophy

Department of Engineering Design and Mathematics, Faculty of Environmental and Technology, University of the West of England, Bristol July 2020

Abstract

This thesis presents a study about the application of a geometrical configuration-based feedforward adaptive active noise control (ANC) system in the low-frequency range of flow-induced (aeroacoustics) noise cancellation and the investigation on the effects of different geometrical configurations on the cancellation performance in the presence of the residual noise signal magnitude (in decibel) or the average amount of cancellation (in decibel). The first motivation is that according to the literature review, the passive flow control is limited in the practical consideration and the active flow control performs better than the passive flow control, especially for the low-frequency range. Consider the principle of the active flow control is the same as the ANC technique, therefore, it is feasible to apply the ANC technique in cancelling the low-frequency range of the far-field (aeroacoustics) noise, which provides instructions on the future practical experiments. The second motivation is that we want to explore the effects of different geometrical configurations on the cancellation performance and it provides instructions on the implementation in future practical experiments. To predict the far-field (aeroacoustics) noise, the computational fluid dynamics (CFD) and the Ffowcs Williams and Hawkings (FW-H) equations are used separately for unsteady flow calculation and far-field (aeroacoustics) noise prediction. The proposed ANC system is used for the low-frequency range of the far-field (aeroacoustics) noise cancellation. Soft computing techniques and evolutionary-computing-based techniques are employed as the parameter adjustment mechanism to deal with nonlinearities existed in microphones and loudspeakers. The case study about the landing gear noise cancellation in the two-dimensional computational domain is completed. Simulation results validate the accuracy of the obtained acoustic spectrum with reasonable error because of the mesh resolution and computer capacity. It is observed that the two-dimensional approach can only predict discrete values of sound pressure level (SPL) associated with the fundamental frequency (Strouhal number) and its harmonics. Cancellation results demonstrate the cancellation capability of the proposed ANC system for the low-frequency range of far-field (aeroacoustics) noise and reflect that within the reasonable physical distance range, the cancellation performance will be better when the detector is placed closer to the secondary source in comparison with the primary source. This conclusion is the main innovative contribution of this thesis and it provides useful instructions on future practical experiments, but detailed physical distance values must be dependent on individual cases.

Acknowledgement

List of Publications

Conference papers:

1. Peng, T, Yao, Y, and Zhu, Q (2018). Slat broadband noise prediction of multi-element 30P30N airfoil by a hybrid RANS-LES method. In: 53rd 3AF International Conference on Applied Aerodynamics, Salon de Provence, France, 26 – 28 March 2018, Salon de Provence, France, 26–28 March 2018.

2. Tongrui Peng, Quanmin Zhu, M. Osman Tokhi, and Yufeng, Yao (2018). Simulated Tests of Feedforward Active Noise Control (ANC) for Building Noise Cancellation. 2018 International Conference on Smart City and Intelligent Building, September 15-16, 2018, Hefei, China. (Published by Springer).

3. Peng T., Zhu Q., M. Osman T., Yao Y. (2020) A Study on PD-like Fuzzy Logic Control Based Active Noise Control for Narrowband Noise Cancellation with Acoustic Feedback and Distance Ratio. In: Wang R., Chen Z., Zhang W., Zhu Q. (eds) Proceedings of the 11th International Conference on Modelling, Identification and Control (ICMIC2019). Lecture Notes in Electrical Engineering, vol 582. Springer, Singapore.

Journal papers:

1. Peng, T.R., Zhu, Q.M., Tokhi, M.O., Yao, Y.F. (2019) Fuzzy logic feedforward active noise control with distance ratio and acoustic feedback using Takagi–Sugeon–Kang inference. Journal of Low Frequency Noise, Vibration and Active Control, 39 (1), pp. 174-189.

2. Peng, T.R., Zhu, Q.M., Tokhi, M.O., Yao, Y.F. (2020) Physical configuration-based feedforward Active Noise Control using adaptive second-order truncated Volterra filter. Journal of Low Frequency Noise, Vibration and Active Control. 1461348419897644.

Content

Abbreviations and Nomenclatures

Abbreviations

ANC	Active noise control
ANFIS	Adaptive-Network-based Fuzzy Inference System
ADC	Analogue-to-digital converter
CAA	Computational aeroacoustics analogy
CFD	Computational fluid dynamics
CML	Continuous moldline link
dB	Decibel
DES	Detached eddy simulation
DBD	Dielectric barrier discharge
DAC	Digital-to-analogue converter
FxLMS	Filtered-x least mean square
FuLMS	Filtered-u least mean square
FLANN	Functional link artificial neural network
FW-H	Ffowcs Williams and Hawkings
HLDs	High-lift devices
LES	Large Eddy Simulation
LMS	Least mean square
LSE	Least square estimation
MmLBFE-LMS	M-max partial update leaky bilinear filtered-error least mean square
OASPL	Overall sound pressure level
PNC	Passive noise control
PID	Proportional-integral-derivative
PD-like FLC	Proportional-derivative-like fuzzy logic control
PSO	Particle swarm optimization
RANS	Reynolds-Averaged Navier-Stokes
RLS	Recursive least mean square
SC	Subtractive clustering

SPL	Sound pressure level
SOV	Second-order truncated Volterra series
SI	Swarm intelligence
SISO	Single-input, single-output
SIMO	single-input, multiple-output
TSK	Takagi–Sugeno–Kang

Nomenclatures

p	Pressure (pascal)
A_p	Sound pressure amplitude
ω	Angular frequency (radians per second)
Ω	Discrete-time frequency (radians per sample)
ϕ	Phase-shift (radians)
k	Wave number (cycles per distance or radian per unit distance)
λ	Wavelength (metres)
c	Sound velocity (metres per second)
f	Frequency (cycles per second)
F_s	Sampling frequency (cycles per sample)
Δp	Unsteady sound pressure/Acoustic pressure fluctuation (pascal)
p_{steady}	Ambient pressure (pascal)
p_{rms}	Root mean square of p (pascal)
p'	Sound pressure in the far-field area (pascal)
z	Specific acoustic impedance (pascal second per metre)
u	Particle velocity (metres per second)
I	Sound intensity (watt per metre-squared)
W	Sound power (watt)
L_p	Sound pressure level (dB)
h_1	Physical distance between the primary source and the detector
h_2	Physical distance between the secondary source and the detector

h_3	Physical distance between the primary source and the receiver
h_4	Physical distance between the secondary source and the receiver
d	Physical distance between the primary source and the secondary source
D	Diameter of the circular cylinder
ρ	Density of the fluid (kilogram per cubic metre)
P_{ij}	Compressive stress sensor
St	Strouhal number
L	Filter order
w	Weight vector
n	Time index
N	Memory length
η	Learning rate
μ	Step size
μ_s	Dynamic viscosity (pascal-second)
$H(f)$	Heaviside function
$\delta(f)$	Dirac delta function

List of Figures

List of Tables

Chapter 1. Introduction

1.1. Background

Noise, defined as unwanted sound, has a wide range of negative effects on people's health (George and Panda, 2013) and the extent of negative effects greatly depend on the noise pressure/intensity level and the situation in which people live or work (Fahy and Walker, 1998). The negative effects can be categorized into two aspects, the auditory effect, and the non-auditory effect, based on the criteria whether it is related to hearing (Peters et al., 2013). The noise can be divided into many different types, e.g. industrial equipment noise, and mechanical-type system noise, and the aircraft noise is one of the most important research and development field.

With the fast development of air traffic, aircraft noise, generated during the phase of take-off and landing (Khorrami, et al., 2004; Ling et al., 2017), is gradually becoming a challenging problem for people especially those who live near the airport (Li et al, 2013) and the resultant environmental concern makes the attenuation of the aircraft noise a very important topic. Figure 1.1a presents several noise sources of the aircraft noise and Figure 1.1b presents the percentage of each component contributing to the overall aircraft noise.
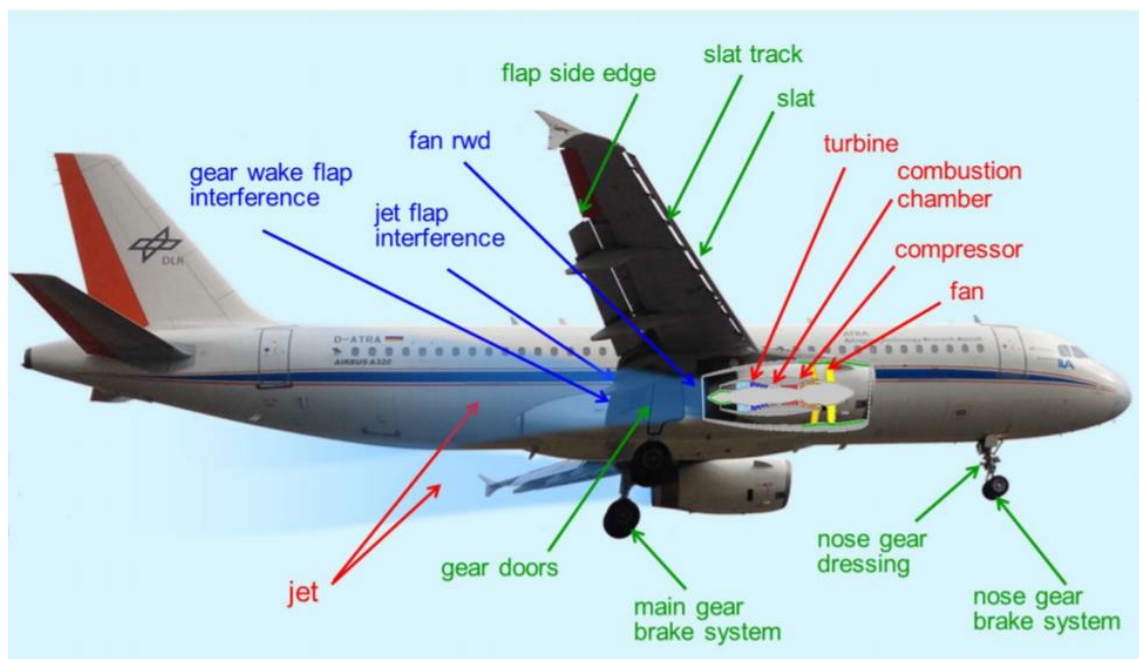
(a)
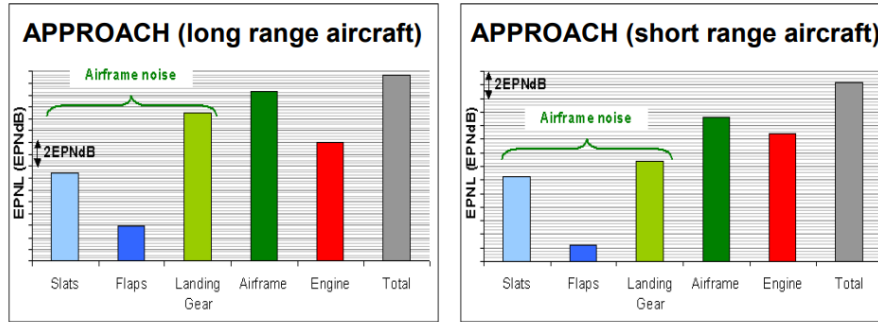
(b)

Figure 1.1. Aircraft noise components. ((a). Bertsch et al., 2019; (b). Dobrzynski, 2008))

The research on the aircraft noise attenuation can be mainly divided into two parts, aero-engine noise attenuation, and airframe noise attenuation. Since the 1970s, with the introduction of the high-bypass ducts and serrated nozzle (Dobrzynski, 2010; Li et al., 2013; Ling et al., 2017), the attenuation of aero-engine noise is significantly and the airframe noise is becoming the major part, which contributes almost 60% of the total noise emission of aircraft (Guo et al., 2006) during take-off and landing phases. Based on Crighton's definition (Crighton, 1991), the airframe noise is generated by all non-propulsive components of an aircraft, which implies that the airframe noise is generated through the interactions between turbulent flow with aircraft components like the landing gear and the high-lift devices (HLDs) (Dobrzynski, 2010). Therefore, the landing gear and the HLDs including the slat, main element, and flap, are two major components contributing to the airframe noise. The landing gear noise is normally broadband in nature, and several noise sources have already been investigated through a full-scale landing gear in the wind tunnel experiment test. The HLDs noise consists of the slat leading-edge noise and the flap trailing-edge noise and the physical phenomenon is complex in comparison with the landing gear noise. Besides, because of the limitation of the wind tunnel size, a full-scale wind tunnel test is not available for the HLDs noise, therefore, the noise sources are not fully understood. Related summary about the noise generation mechanisms, the noise prediction methods, and the noise control strategies can be found in Chapter 2.

In Europe, aircraft noise is a major concern for communities, which leads a great pressure on policymakers to issue legislations and regulations for noise control. The aim of the EU 'Visions 2020' is to reduce noise impact by 50% per operation relative to 2000 technology (Leylekian et al., 2014). Meanwhile, in America, NASA research centre also proposes 'pillar goals' aimed at reducing the perceived noise impact of future aircraft by 50% relative to 1997 technology within 10 years (Dobrzynski, 2010). To attenuate the noise pressure level, the passive noise control (PNC) technique and the active noise control (ANC) technique are widely used. In contrast

to the PNC technique, the ANC is an electro-acoustic/electro-mechanical approach, which is based on the principle of superposition. A secondary acoustic wave with the same amplitude and an opposite phase with respect to the primary acoustic wave is generated by the secondary source and superimpose the primary acoustic wave at the receiver point to cancel/attenuate the primary acoustic wave pressure level. The history of the ANC can date back to the early 1930s when Lueg first used a loudspeaker to generate the secondary acoustic wave to realize the ANC technique (Lueg, 1936). Following Lueg's work, many researchers devote their contributions to the development of ANC and a summary of their contributions can be found in several review papers (Leitch and Tokhi, 1987; Kajikawa et al., 2012; George and Panda, 2013; Li and Jiang, 2018). A detailed introduction about the ANC technique is provided in Chapter 2.

1.2. Challenges

The challenges of this thesis can be acknowledged as follows:

1.   The physical implementation constraints during the process of applying the ANC technique in cancelling the low-frequency part of far-field (aeroacoustics) noise of the turbulent flow over the circular cylinder in the two-dimensional computational domain.

2.   The nonlinearity problem.

1.3. Motivations

There are two motivations of this thesis:

1.   According to the literature review, the passive flow control is limited in the practical consideration and the active flow control performs better than the passive flow control, especially for the low-frequency range. Consider the principle of the active flow control is the same as the ANC technique, therefore, it is feasible to apply the ANC technique in cancelling the low-frequency range of the far-field (aeroacoustics) noise, which provides support for the future practical experiments.

2.   Physical distance constraints have a significant effect on the cancellation performance of an ANC system. In this thesis, we aim at numerically exploring the appropriate geometrical configuration corresponding to the optimal cancellation performance, and it provides instructions on the future experiments.

1.4. Contributions

There are two contributions to knowledge in this paper:

1.   Detailed descriptions and mathematical expressions of the application of the geometrical configuration-based feedforward adaptive ANC system in cancelling the low-frequency range of far-field

(aeroacoustics) noise, which is generated by the turbulent flow around a circular cylinder in the two-dimensional computational domain, are provided.

2.   Simulation results reveal that in the future physical experiments, within the reasonable physical constraints range, we need to place the detector closer to the secondary source in comparison with the primary source to achieve a better cancellation performance.

1.5. Thesis organization

The rest of the thesis is arranged as follows: Chapter 2 is the literature review about the airframe noise and the ANC technique. Chapter 3 introduces fundamental concepts of acoustics and basic knowledge about the adaptive control, which paves the way for further numerical analysis. Chapter 4 firstly presents the proposed geometrical configuration-based feedforward adaptive single-input, single-output (SISO) ANC system for the point source (e.g. the low-frequency part of the landing gear noise) cancellation and the finite impulse response (FIR) filter is used as the digital filter. Secondly, the geometrical constraints are provided both in the form of scalar quantities and vector quantities. Meanwhile, the corresponding locus of system components including the primary source, the secondary source, the detector, and the receiver in the three-dimensional Euclidean space is provided. Thirdly, the filter identification method, the employment of the nonlinear adaptive filter, and the soft computing techniques are discussed. Finally, several simulation experiments are executed to illustrate the principle of the ANC system, demonstrate the cancellation capability of the proposed ANC system, and explore the effects of different geometrical configurations on the cancellation performance. Chapter 5 presents the procedures and simulation results of the application of the proposed ANC system in cancelling the low-frequency range of far-field (aeroacoustics) noise generated by the turbulent flow over a circular cylinder in the two-dimensional computational domain. Besides, it also discusses the effects of different geometrical configurations on the cancellation performance, which paves the way for further practical experiments. Chapter 6 summarizes the whole thesis.

Chapter 2. Literature review

2.1. Introduction

This chapter consists of two parts. The first part is to review the airframe noise including noise generation mechanisms, noise prediction methods, noise control approaches, and the corresponding cancellation performance. The second part is to review the ANC technique including the general introduction, the description of physical constraints, and the nonlinear problem explanation.

2.2. Airframe noise review

2.2.1. Airframe noise generation mechanisms

The first introduced component of the airframe noise is the landing gear noise, which is normally broadband in nature (Li et al., 2013) and contains several narrowband noise components. The generation mechanisms of the landing gear noise are identical and can be categorized into two parts (Cai et al., 2018):

1. Turbulence flow separation off the bluff-body components.

2. Interaction of such turbulent wake flows with downstream located gear elements.

The landing gear noise greatly depends on two factors, the flow turbulence characteristics, and the local impinging flow velocity (Dobrzynski, 2010). The wheels and main struts are the sources of the low-frequency noise and smaller details like hoses and dressings are the sources of the high-frequency noise (Li et al., 2013).

The second introduced component of the airframe noise is the HLDs noise, which consists of the slat leading-edge noise and the flap trailing-edge noise. According to results from the model scale tests (Dobrzynski, 1998; Storms et al., 1999) and the flyover noise measurements (Chow et al., 1998), the slat leading-edge noise is the dominant noise source of the airframe noise during the aircraft approach and landing (Khorrami et al., 2004; Lockard and Choudhari, 2009). Figure 2.2.1.1 presents several potential noise source generation mechanisms for both slat and flap parts.
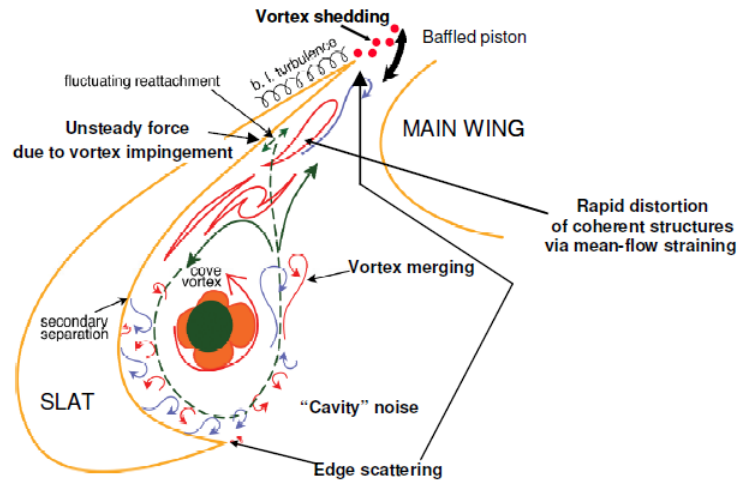
(a) slat component
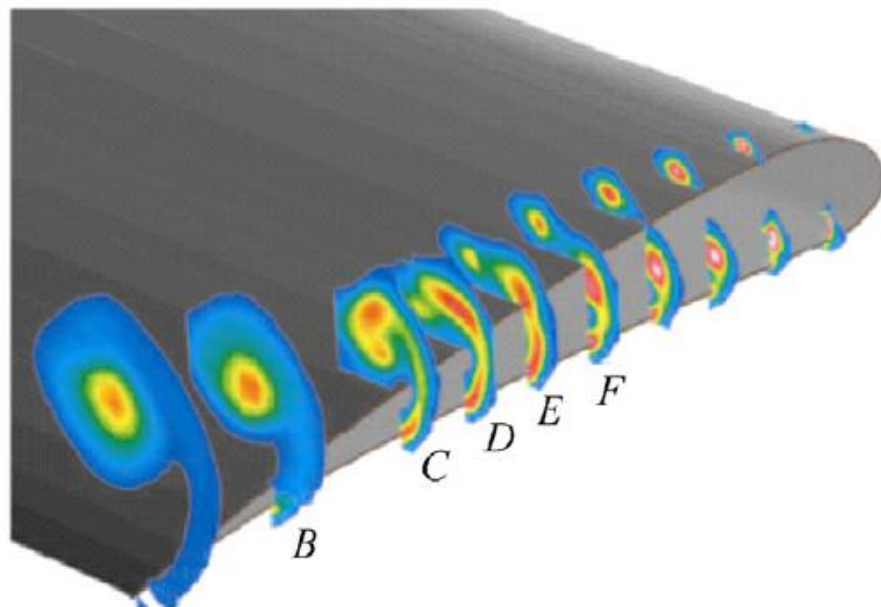
(b) flap component

Figure 2.2.1.1. Noise source generation mechanisms for the slat and the flap component (Radezrsky et al., 1998; Choudhari and Khorrami, 2006; Li et al., 2013)

It can be found that the slat noise is a complex aeroacoustics problem (Lockard and Choudhari, 2009), which is composed of several different noise generation mechanisms. In the salt cove area, the vortex flow is developing due to the flow through the slat slot. An unsteady shear layer is generated between the vortex and the undisturbed slot surface. Besides, the impingement of the vertical shear flow on the downstream cove surfaces and the unsteady flow shedding off the trailing edge (Choudhari and Khorrami, 2006; Dobrzynski, 2010; Li et al., 2013) denotes another two potential slat noise sources. Generally, the slat noise contains two parts, the broadband

part covering the middle and the lower frequencies and the high-frequency tonal part (Khorrami et al., 2000; Singer et al., 2000). For flap trailing-edge noise, the vortex flow and its interaction with the flap upper surface is the main noise generation mechanism.

2.2.2. Airframe noise prediction methods

Table 2.2.2.1 summarizes prediction models for the landing gear noise.

Table 2.2.2.1. Prediction models for the landing gear noise

Name of the prediction model	Year
The first empirical landing gear noise prediction	1977
Smith and Chow's model	2002
Guo et al's noise prediction approaches	2004, 2006
Computational model	N/A

Currently, prediction methods of the HLDs noise can be classified as four categories, semi-empirical methods, fully analytical methods, advanced computational fluid dynamics (CFD) methods, e.g. Reynolds-Averaged Navier-Stokes (RANS) model, and Large eddy simulation (LES) model, coupled with computational aeroacoustics (CAA) methods, e.g. Lighthill's analogy and Ffowcs Williams and Hawkings (FW-H) equations, and fully numerical methods. The prediction method strongly depends on the mesh quality and the capacity of computers. Besides, the experimental measurement includes the flight test and the wind tunnel experiment is another way to obtain the aeroacoustics noise data.

2.2.3. Airframe noise control approaches

The noise control approaches for the airframe noise can be categorized into two parts, the passive flow control approach, and the active flow control approach.

Table 2.2.3.1 and Table 2.2.3.2 present several recent successful control approaches developed for the landing gear noise and the HLDs noise separately. Table 2.2.3.3 summarizes active flow control approaches for the airframe noise including both landing gear noise and HLDs noise.

Table 2.2.3.1. Passive flow control approaches for the landing gear noise

Name of the approach	Cancellation Performance
Fairing / Individually customized fairing	10 dB for the entire gear structure 2 dB to 3 or 3.5 dB for the full-scale tow bar and axle
Plate	4 dB for far-field noise

Splitter plate	1-2 dB for various gear components

Table 2.2.3.2. Passive flow control approaches for the HLDs noise

Name of the approach	Cancellation Performance
Add-on devices for noise source in the slat cove/slot area	4-5 dB for the broadband noise 2 dB to 3 or 3.5 dB for the full-scale tow bar and axle
Transparent edge replacements	effective for trailing-edge noise reduction
Side-edge treatments	significant reduction
Continuous moldline link (CML) technology	a large reduction

Table 2.2.3.3. Active flow control approaches for the airframe noise

Name of the approach	Cancellation Performance
Plasma actuator (mainly for landing gear noise)	13.3 dB for near-field sound pressure level
Air blowing (for both landing gear noise and HLDs noise) Air suction (mainly for slat noise)	3-10 dB depends on the angle noise reduction of 3–4 dB for the flap-edge noise a massive amount of reduction on the slat cove noise

2.3. Active Noise Control

2.3.1. Background

The industrial noise is a challenging problem and noise sources are mainly coming from two parts, the industrial equipment, and the mechanical system. Engines, blowers, fans, transformers, and compressors are common types of the industrial equipment (Kajikawa et al., 2012; George and Panda, 2013; Jiang and Li, 2018; Nunez et al., 2019), and transportation systems, electrical appliances, and medical systems are classical representatives of the mechanical system (Kajikawa et al., 2012; Jiang and Li, 2018). According to published documents from the World Health Organization (WHO) in 1999[1], adverse effects of noise[2] on health mainly from physical and psychological aspects like noise-induced hearing loss, interference with speech communication, and disturbance of sleep. Therefore, noise control is a widespread topic and currently, the source-transmission path-receiver (S-T-R) model is the commonly used noise control model because of simplicity (see Figure 2.3.1.1).

---

[1] *Peters, R J., Smith, B J., and Hollins, N. Acoustics and Noise Control, 3rd ed., Pearsons Education Limited. London, UK, 2011, pp. 34-53.*
[2] Adverse effects of noise can be further divided into auditory and non-auditory fields. Auditory effects are related to the hearing and the representative examples are annoyance and sleep disturbance. Typical examples of non-auditory effects are performance effects and physiological responses.
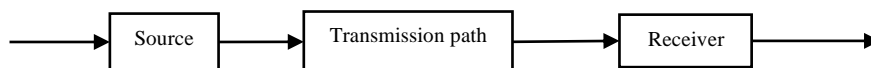
Figure 2.3.1.1. S-T-R model

It reflects that noise control can be implemented at three stages, e.g. at the source, during the propagation medium, and at the receiver point. Currently, the noise control fields are classified as two main domains, the passive domain, and the active domain. The PNC technique relies on absorbers or barriers to attenuate the noise pressure level, e.g. the sound absorption[3], and the sound insulation[4] are used for airborne sound[5] attenuation, the isolation[6], and the damping[7] are used for structure-borne sound[8] attenuation. Besides, hearing protection is another form of the PNC technique, which is normally employed at the receiver. Although the PNC technique performs better for the high-frequency noise cancellation, for the low-frequency noise, the requirement of increasing wavelength and heavier intervening barrier make the PNC technique bulky, inconvenient, and costly. To solve the problem, the ANC technique is proposed for low-frequency noise (normally below 1000 *Hz*) cancellation[9] (Mazur et al., 2019; Nunez et al., 2019).

The advantages of the ANC technique over the PNC technique can be summarized as follows (Jiang and Li, 2018):

1.   Design or amend the parameters of the control system based on the types of noise.

2.   Better cancellation performance for the low-frequency noise (normally below 1000 *Hz*).

3.   Flexible, cheaper, and no negative impacts on the structure and performance of the machine.

In 1936, Lueg firstly used an electronically driven loudspeaker and a microphone to achieve the active noise control (Lueg, 1936) for the monopole source in the duct. The microphone was used for detecting the primary acoustic wave and transferring to the electrical signal, which is processed through the digital filter to produce the output signal to drive the loudspeaker to generate the secondary acoustic wave. Lueg defined two concepts, the electrical delay, and the acoustical delay, to illustrate the physical phenomenon. The acoustic delay is defined as the delay from the primary source to the receiver point and the electrical delay is defined as the amount of time consumed during the propagation path through the electrical devices including the microphone,

---

[3] It is the process that sound energy is converted to heat energy leading to a reduction of sound pressure level.
[4] It is the process that sound energy is converted to heat energy.
[5] Sound radiated from the loudspeaker or machine into the surrounding air.
[6] The employment of resilient materials between source and receiver to reduce noise.
[7] The vibration energy is converted into heat energy via several frictional mechanisms.
[8] Sound reaches the receiver via building or machine structure, efficiently in building and hard to predict.
[9] The low-frequency range of the landing gear noise is approximately between 0 Hz and 950 Hz, which is the reason for using the ANC technique.

the amplifier, the analogue-to-digital converter (ADC), the digital-to-analogue converter (DAC), and the loudspeaker. In 1953, Olson and May designed an electronic sound absorber, a feedback system consisting of a loudspeaker, an amplifier, and a microphone, to reduce the sound pressure level (SPL) near the microphone. In 1955, Conover and Ringlee relied on large transformers to cancel the noise, which is recognized as a pioneering work in the ANC field. However, the characteristic of this period is not mature and there is a long quite period between the 1950s and the 1980s until the rapid development of digital signal processing and large-scale integrated circuit technology, which contributes the fast development of practical implementation (Jiang and Li, 2018) and a summary of these works can be found in several review papers (Kajikawa et al., 2012; George and Panda, 2013; Jiang and Li, 2018). In recent three years, researchers focus on expanding the application area of the ANC system, e.g. from the ANC headset to the residual building, and improving the cancellation performance of the ANC system by adjusting the geometrical configuration of detectors and loudspeakers based on the evolutionary-computing-algorithm, applying the online secondary path modelling or virtual secondary path algorithm, increasing the number of microphones and loudspeakers (from single-channel to multi-channel), designing advanced adaptive filters, and proposing more complex signal processing algorithms with the advancement of low-cost, fast-computation hardware, e.g. In 2018, Luo et al. proposed an improved functional link artificial neural network (FLANN) filter for the nonlinear active noise control system (Leo et al., 2018). In 2019, Mazur et al. applied the ANC technique to make a quiet washing machine (Mazur et al., 2019). In 2020, Niu et al. evaluated the influence of active noise cancelling headphones on speech recognition (Niu et al., 2020).

From the perspective of the control structure, the ANC system can be categorized into two parts, feedforward, and feedback. In the feedforward control system, the detector is placed upstream of the secondary source to detect the primary acoustic wave and transfer to the electrical signal. The adaptive controller is used for processing the electrical signal and its output is used for driving the loudspeaker to generate the secondary acoustic wave. The receiver is placed downstream of the secondary source, aimed at monitoring the cancellation performance in terms of the amplitude of the residual noise signal in the time domain or the magnitude in the frequency domain. Besides, the residual noise signal can also be used for tuning the coefficients of the adaptive controller to adjust the cancellation performance. Consider that the frequency content of the primary acoustic wave may be broadband or narrowband, therefore, the feedforward ANC system can be further categorized as broadband and narrowband. In the broadband feedforward ANC system, the microphone is usually selected as the detector and for the narrowband feedforward ANC system, the accelerometer is usually selected as the detector and the primary acoustic wave signal is internally generated using the information available from a detector that

is not affected by a control field. The most popular application in the industrial field is single-channel feedforward ANC scheme consisting of one detector, one loudspeaker, and one receiver. In the feedback ANC system, only the secondary loudspeaker, the adaptive controller, and the receiver exist, which is widely used in the application of headset (Kuo et al., 2006). Currently, the main weakness of the feedback ANC system is that it cannot reduce broadband noise and the reason is that the large delay due to the ADC and the DAC.

2.3.2. System configuration

Physical distance is an important factor when designing the ANC system. In 1981, Eghtesadi and Leventhall discussed the conventional monopole system, which consists of a microphone, a loudspeaker, the primary source, and the secondary source. The conventional monopole system is constructed based on the duct model and the microphone is located upstream of the secondary source. The feedforward path is modelled by an electrical time delay and anti-phase. The acoustic feedback path, defined the upstream radiation from the secondary path, is modelled by a pure time delay. The mathematical expression of the time delay τ is:

$$\tau = \frac{l}{c} \tag{2.3.2.1}$$

Where l represents the distance between the microphone and the loudspeaker and c is the sound velocity in the propagation medium.

In 1987, Leitch and Tokhi stated that there was little literature considering the effects of the geometrical configuration, especially the acoustic feedback phenomenon, and the best geometrical arrangement was lack. In fact, the superimposing of two acoustic waves at the receiver point will generate two zones in the propagation medium, the cancellation zone, and the reinforcement zone. It means in some areas, the noise pressure level is reduced and in other areas, the noise pressure level is reinforced. The region of the cancellation zone greatly depends on the maximum frequency of the noise and the physical separation between two sources. To quantitatively describe the phenomenon of cancellation for the point source in the free-field acoustic environment, they firstly proposed a concept of the filed cancellation factor, K.

The primary source emits a primary acoustic wave and it generates a primary sound field $p(h_3, n)$ in the propagation medium. The secondary source emits the secondary acoustic wave and it generates a secondary sound field $s(h_4, n)$ in the propagation medium. We use $e(n)$ to represent the observed signal/the residual noise signal at the receiver point (see Figure 2.3.2.1).
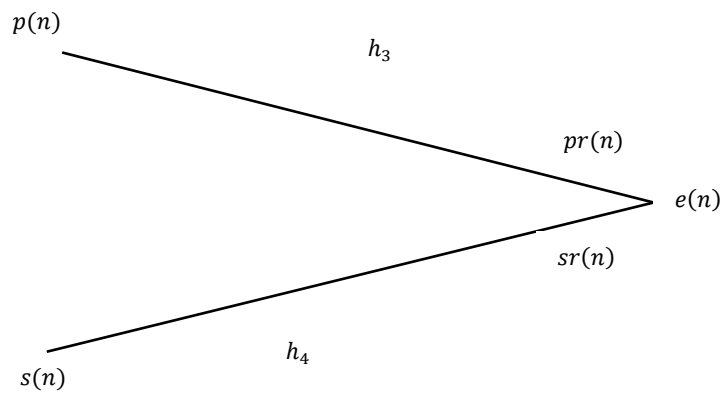
Figure 2.3.2.1. Point source cancellation (free-field acoustic environment)

Where:

$p(n)$: the primary acoustic wave signal at the primary source

$s(n)$: the secondary acoustic wave signal at the secondary source

$pr(n)$: the primary acoustic wave signal at the receiver

$sr(n)$: the secondary acoustic wave signal at the receiver

$e(n)$: the observed signal/the residual noise signal at the receiver

n: the time index

h_3: the physical distance between the primary source and the receiver

h_4: the physical distance between the secondary source and the receiver

The basic system of Figure 2.3.2.1 can be drawn as Figure 2.3.2.2.
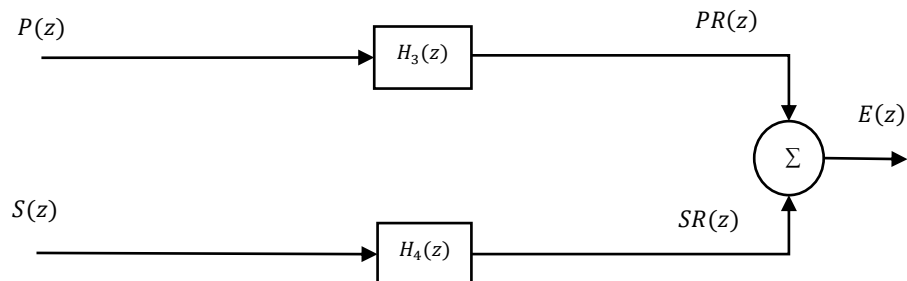
Figure 2.3.2.2. Transfer function description of acoustic paths

Where:

$P(z)$: Z-transform of $p(n)$

$PR(z)$: Z-transform of $pr(n)$

$S(z)$: Z-transform of $s(n)$

$SR(z)$: Z-transform of $sr(n)$

$H_3(z)$: Z-transform of the acoustic path between the primary source and the receiver through distance h_3

$H_4(z)$: Z-transform of the acoustic path between the secondary source and the receiver through distance h_4

$E(z)$: Z-transform of $e(n)$

$H_3(z)$ and $H_4(z)$ are defined as:

$$\begin{cases} H_3(z) = \dfrac{A}{h_3} e^{-F_s \ln Z t_3} \\ H_4(z) = \dfrac{A}{h_4} e^{-F_s \ln Z t_4} \end{cases} \tag{2.3.2.2}$$

F_s denotes the sampling frequency and A denotes a constant.

Remark 1: Here, we assume the constant is the same for both signals. In practice, its value depends on the practical situation.

t_3 and t_4 are time constant, which are defined as

$$\begin{cases} t_3 = \dfrac{h_3}{c} \\ t_4 = \dfrac{h_4}{c} \end{cases} \tag{2.3.2.3}$$

c denotes the sound velocity in the propagation medium and detailed descriptions are provided in Chapter 3.

The field cancellation factor is defined as the ratio of the cancelled spectrum to the primary spectrum, it follows that:

$$K = \frac{GPR(\Omega) - GE(\Omega)}{GPR(\Omega)} \tag{2.3.2.4}$$

Ω means the discrete-time frequency in radians per sample. $GPR(\Omega)$ represents the autopower spectral density of $pr(n)$ and $GE(\Omega)$ represents the autopower spectral density of $e(n)$.

Based on the cancellation requirement that $GPR(\Omega) > GE(\Omega)$, it follows that for cancellation to occur, K must lie between zero and unity, where zero corresponds to no cancellation and a unity corresponds to complete cancellation.

According to the statement provided by Leitch and Tokhi, the value of the field cancellation depends on the phase difference[10] Δh_{34} and the physical distance difference[11] $\Delta\theta(\omega)$, which is specified as:

$$K = -\frac{GSR(\Omega)}{GPR(\Omega)} - \sqrt{\frac{GSR(\Omega)}{GPR(\Omega)}}\cos\left(\Omega\frac{\Delta h_{34}}{c}{}^{12} - \Delta\theta(\Omega)\right) \qquad (2.3.2.5)$$

$GSR(\Omega)$ represents the autopower spectral density of $sr(n)$.

Remark 2: A detailed procedures for obtaining Eq. (2.3.2.5) can be found in Tokhi and Leitch's published paper in 1987.

Eq. (2.3.2.5) reveals that the introduction of K gives an analytical relationship between the relative phase $\Delta\theta(\Omega)$, the relative amplitudes $\frac{GSR(\Omega)}{GPR(\Omega)}$, and the degree of cancellation (the cancellation performance).

Based on the concept of K, Leitch and Tokhi proposed a physical distance-based ANC system (see Figure 2.3.2.3).
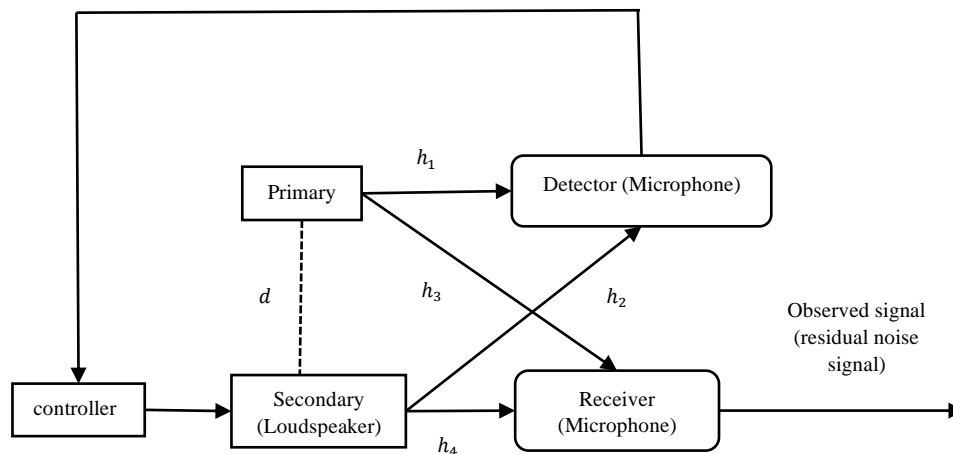
Figure 2.3.2.3. Schematic diagram of Feedforward ANC System (Tokhi and Leitch, 1987)

Where:

h_1: the physical distance between the primary source and the detector

h_2: the physical distance between the secondary source and the detector

d: the physical distance between the primary source and the secondary source

Remark 3: Explanations of h_3 and h_4 are provided above.

---

[10] Defined as the difference between $p(t)$ and $s(t)$

[11] Defined as the difference between h_p and h_s

[12] $\Delta h_{34} = h_3 - h_4$

Figure 2.3.2.4 presents the corresponding block diagram in z domain.
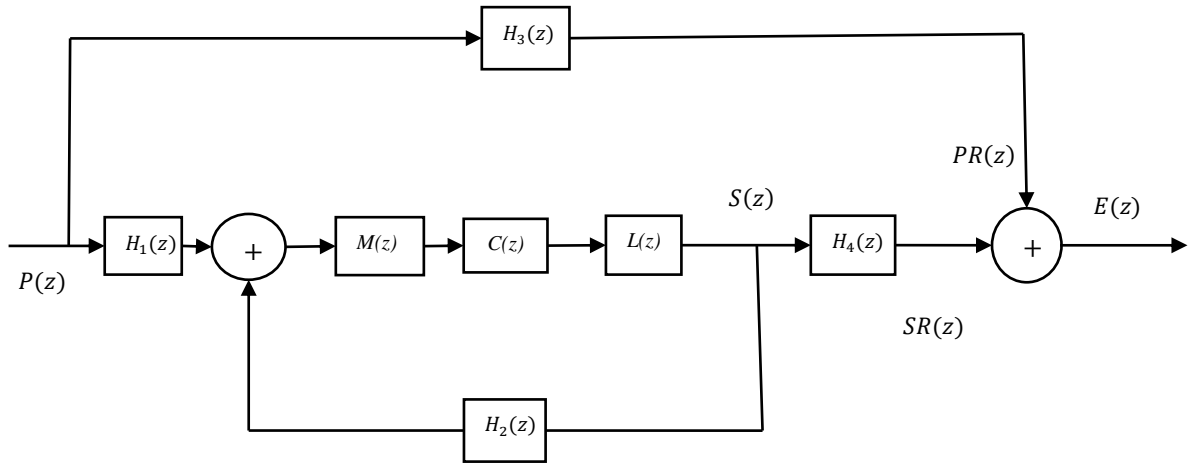
Figure 2.3.2.4. The corresponding block diagram in z domain

Where:

$H_1(z)$: Z-transform of the acoustic path between the primary source and the detector through distance h_1

$H_2(z)$: Z-transform of the acoustic path between the secondary source and the detector through distance h_2

$M(z)$: transfer function of the microphone

$L(z)$: transfer function of the loudspeaker

$C(z)$: transfer function of the controller

Remark 4: Explanations of $P(z)$, $PR(z)$, $S(z)$, $SR(z)$, $E(z)$, $H_3(z)$, and $H_4(z)$ are provided above.

The objective of the proposed system is to reduce the noise pressure level at the receiver point to zero and we can obtain that:

$$PR(z) + SR(z) = 0 \qquad (2.3.2.6)$$

$PR(z)$ can be written as:

$$PR(z) = P(z)H_3(z) \qquad (2.3.2.7)$$

$SR(z)$ can be expressed as:

$$SR(z) = S(z)H_4(z) \qquad (2.3.2.8)$$

From Figure 2.3.2.4, $S(z)$ can be expressed as follows:

$$S(z) = \frac{M(z)C(z)L(z)H_1(z)}{1 - M(z)C(z)L(z)H_2(z)} P(z) \qquad (2.3.2.9)$$

Combine Eq. (2.3.2.8) and Eq. (2.3.2.9), one can obtain that:

$$SR(z) = \frac{M(z)C(z)L(z)H_1(z)H_4(z)}{1 - M(z)C(z)L(z)H_2(z)} P(z) \qquad (2.3.2.10)$$

Using Eq. (2.3.2.7) and Eq. (2.3.2.10) to substitute $PR(z)$ and $SR(z)$ in Eq. (2.3.2.6) respectively and we can obtain that:

$$P(z)H_3(z) + \frac{M(z)C(z)L(z)H_1(z)H_4(z)}{1 - M(z)C(z)L(z)H_2(z)} P(z) = 0 \qquad (2.3.2.11)$$

Solve Eq. (2.3.2.11) and we can obtain the mathematical expression of the controller as:

$$C(z) = \frac{H_3(z)}{M(z)L(z)(H_2(z)H_3(z) - H_1(z)H_4(z))} \qquad (2.3.2.12)$$

Eq. (2.3.2.12) reveals that the controller greatly depends on the geometrical configuration of system components including the primary source, the secondary source, the detector, and the receiver. Based on Leitch and Tokhi's works, in 1997 Hansen and Snyder described the sources and sensor (detector and receiver) geometry for a single-channel system in three-dimensional Euclidean space. In 2006, Kaymak et al discussed the application of the geometrical configuration-based ANC system in the dental drill noise cancellation and they pointed that the distance ratio[13] of the receiver must greater than the distance ratio[14] of the detector to guarantee the causality[15]. They concluded that to design a successful ANC system, we need to follow four procedures, which are specified as follows:

1. Determine the control source (secondary source) arrangement

2. Determine the receiver arrangement

3. Maximum the quality of the detected signal (in feedforward systems)

4. Evaluate the cancellation performance

In 2010, Raja Ahmad and Tokhi presented an analysis of the geometry-related constraints of a single-input single-output (SISO) minimum effort active noise control system with feedback inclusion architecture which

---

[13] $distance\ ratio = \frac{distance\ between\ the\ receiver\ and\ the\ primary\ source}{distance\ between\ the\ receiver\ and\ the\ secondary\ source}$

[14] $distance\ ratio = \frac{distance\ between\ the\ detector\ and\ the\ primary\ source}{distance\ between\ the\ detector\ and\ the\ secondary\ source}$

[15] The acoustic delay must longer than the electrical delay and this is the essential condition for broadband noise cancellation.

includes the feedback path in the controller formulation. In recent three years, based on Leitch and Tokhi's works, researchers prefer to focus on the effects of geometrical configuration during the application process. For example, in 2018, Wrona et al stated that the performance of an ANC system strongly depends on the spatial arrangement of the microphone(s) and the loudspeaker(s), especially in the enclosure. Therefore, they proposed a complete method for enhancing the noise reduction (NR) levels and shaping zones of quiet generated with an ANC system by optimization of the microphone(s) and the loudspeaker(s) arrangement (Wrona et al., 2018). Besides, in 2018, Lam et al designed an open window ANC system to preserves natural ventilation in dwellings. They explored the effect of the quantity and the position of the control sources (the secondary sources) and conclude that the best attenuation is achieved by placing the control sources away from the edges of the window (Lam et al., 2018).

2.3.3. Nonlinearity

The nonlinearity problem is a challenging task and it degrades the cancellation performance of the transversal-filter-based ANC system. The nonlinearities are coming from three parts, the noise source, the propagation path, and the actuators including both loudspeakers and microphones. The nonlinearity of the noise source denotes the dynamic system, used for noise generation, is nonlinear. The nonlinearities that existed in the propagation path are mainly due to the nonlinear impulse response. The nonlinearity in the loudspeaker and the microphone is due to the saturation[16] effect and detailed descriptions can be found in many published journals (Kuon and Morgan, 1999; Kuo et al., 2004; Zhang et al., 2010).

2.4. Summary

This chapter presents a brief review of the airframe noise and the ANC technique. It can be found that airframe noise generation mechanisms are complex. For the airframe noise prediction methods, both prediction models and experimental measurements are applied by different researchers to obtain aeroacoustics noise data. For the airframe noise control approaches, the active flow control approach performs better than the passive flow control approach. For the ANC technique, the physical constraints of practical implementation and the nonlinearity problem are two main factors affecting the cancellation performance. For the physical constraints, in the early stage, developments focused on the fundamental physical constraints, and in recent three years, researchers pay more attention to more complicated physical constraints during the process of applying the ANC technique in solving real world problems. For the nonlinearity problem, we understand that the nonlinearities are coming from three parts and the generation mechanisms are quite different.

---

[16] Due to the high level of the reference noise

Chapter 3. Fundamental concepts

3.1. Fundamental concepts of acoustic

3.1.1. Nature of sound

Sound is a wave motion and it can transmit the changes or disturbances in some physical properties of the medium through that medium. In acoustical terminology, we use concepts of wavefront and ray to describe a wave. The wavefront denotes the leading edge of the acoustic wave and it reflects how far the wave can arrive. The ray is perpendicular to the wavefront and it is used for indicating the direction of the wave.

From the perspective of dimension, the sound wave can be categorized as the plane wave (one-dimension) and the spherical wave (three-dimensions), which can be used for explaining the concept of frequency and wavelength. From the perspective of the relationship between the direction of particles and the direction of wave propagation, the wave can be divided into transverse waves and longitudinal waves.

The character of the transverse wave is that the oscillation is perpendicular to the direction of the wave and its mathematical expression in terms of the sound pressure p is a function of time, which is specified as:

$$p = A_p sin(\omega t + \phi) \tag{3.1.1.1}$$

A_p denotes the sound pressure amplitude, ω represents the angular frequency in radians per second, and ϕ means the phase-shift in radians.

The longitudinal wave[17] refers that the displacement of the medium is parallel to the direction of the wave and its mathematical expression in terms of the sound pressure p is a function of distance, which is specified as:

$$p = A_p sin(kx + \phi) \tag{3.1.1.2}$$

k is the wavenumber in cycles per distance or radian per unit distance, which is specified as:

$$k = \frac{2\pi}{\lambda} \tag{3.1.1.3}$$

λ means the wavelength in metres, which is the minimum distance between points on the wave where the air particles are vibrating in step or in phase, and its mathematical expression is:

$$\lambda = \frac{c}{f} \tag{3.1.1.4}$$

---

[17] The displacement of particles in the medium will cause the phenomenon of compression and rarefaction, which leads to the pressure fluctuations

f represents the frequency in cycles per second (Hz). The frequency of the sound wave is only determined by the sound source. c means the sound velocity and it is only determined by the nature of wave and the property of the propagation medium (e.g. air, water). Normally, the sound velocity in air is approximately between $330m/s$ and $340m/s$, depending upon the air temperature.

Sometimes, we need to express the sound pressure p at any time, any position, therefore, mathematical equations are specified as:

$$p = A_p sin(\omega t - kx) \tag{3.1.1.5}$$

$$p = A_p sin(\omega t + kx) \tag{3.1.1.6}$$

Eq. (3.1.1.5) represents the sound pressure wave propagating in the positive direction of the *x*-axis and Eq. (3.1.1.6) represents the sound pressure wave propagating in the negative direction of the *x*-axis.

3.1.2. Acoustic quantity

The first acoustic quantity is sound pressure p (measured in pascal (Pa)). For human beings, the perception of sound is the response to the unsteady sound pressure[18] Δp, the variation compared to the ambient pressure, to the ear and the expression of the unsteady sound pressure is:

$$\Delta p = p - p_{steady} \tag{3.1.2.1}$$

Δp is the acoustic pressure fluctuation (unsteady sound pressure) caused by the passage of the acoustic wave. Normally the microphone is used to detect Δp in air and the hydrophone is used to detect Δp in water.

p_{steady} is the ambient pressure, which is obtained as:

$$p_{steady} = \lim_{T \to \infty} \int_{-T/2}^{T/2} p(t + t')dt' \tag{3.1.2.2}$$

In practice, the root-mean-square value p_{rms} is employed to represent the strength of the sound pressure, it is defined as:

$$p_{rms} = \sqrt{\overline{p(t)^2}} = \sqrt{\lim_{T \to \infty} \frac{1}{T} \int_{-T/2}^{T/2} p(t)^2 dt} \tag{3.1.2.3}$$

---

[18] The audible sound pressure range is from $2 \times 10^{-5} Pa$ to $20 Pa$

T denotes the average period and in practice, the value of T should be large enough when compared to the period of the fluctuation. The reason for using p_{rms} is that it can be related to the average intensity of the sound and the loudness of the sound.

The second acoustic quantity is sound intensity. Sound intensity, defined as the power carried by sound waves per unit area in a direction perpendicular to that area, is used for describing the magnitude and direction of the rate of transfer energy per unit cross-sectional area.

The symbol of sound intensity is I and the unit is W/m^2, it is defined as:

$$I = \frac{1}{T}\int_{-T/2}^{T/2} p(t)u(t)dt \tag{3.1.2.4}$$

$u(t)$ represents the particle velocity (measured in $m/_S$). The difference between the particle velocity and the sound velocity is that the former is used for the acoustic signal and the latter is used for describing the process of the compression propagating through the medium.

In fact, the human auditory system can cope with sound pressure variations over a range of more than a million times, therefore, the sound pressure and other acoustic quantities are usually measured on a logarithmic scale. Besides, a logarithmic measure of the sound pressure is more appropriate for describing the subjective impression of how loud noise sounds in comparison with the sound pressure itself.

The logarithmic measure is specified as:

$$L_I = 10\log_{10}\frac{I}{I_{ref}} \tag{3.1.2.5}$$

L_I is called as the sound intensity level and its unit is decibel[19] (dB). Eq. (3.1.2.5) reveals that dB is a power-related ratio which requires a reference quantity.

The mathematical relationship between sound intensity and sound pressure is:

$$I = \frac{p^2}{z} \tag{3.1.2.6}$$

z represents the specific acoustic impedance (measured in pascal second per metre), which only depends on the nature of the medium.

Combine Eq. (3.1.2.5) and Eq. (3.1.2.6), we can obtain the sound pressure level (SPL) L_p as:

---

[19] The decibel scale is a logarithmic scale for measuring or comparing energies or powers, or related quantities such as sound intensity and sound pressure.

$$L_p = 20 \log_{10} \frac{p}{p_{ref}} \tag{3.1.2.7}$$

$p_{ref} = 20 \times 10^{-6} pa.$

3.1.3. Inverse square law

The inverse square law is a fundamental principle of describing the geometrical spreading of sound in the propagation medium. There are many different types of sound source, monopole source, dipole source, and quadrupole source. The monopole source is a source that radiates sound equally in all directions or the source radiates the spherical waves into the surrounding medium. The monopole source is also called as a simple source or a point source. A dipole source consists of two monopole sources of equal strength but opposite phase and separated by a small distance compared with the wavelength of sound. The quadrupole source consists of two opposite phase dipole sources. To simplify the complexity of analysis, we focus on the inverse square law for an idealized point source (monopole source) in the free field[20] environment.

According to the definition of sound intensity, one can obtain that:

$$I = \frac{W}{S} \tag{3.1.3.1}$$

W means sound power (measured in watt) and S denotes the surface area.

For the point source in the free-field environment, the wavefront radiated by the source will be spherical and we can obtain the surface area of a sphere as:

$$S = 4\pi r^2 \tag{3.1.3.2}$$

r is the radius of the sphere.

Combine Eq. (3.1.3.1) and Eq. (3.1.3.2), we can obtain that:

$$I \propto \frac{1}{r^2} \tag{3.1.3.3}$$

Eq. (3.1.3.3) is called the inverse square law and it describes that the sound intensity is inversely proportional to distance squared. Besides, based on the inverse square law, we can also find the relationship between the sound pressure and the distance.

Combine Eq. (3.1.2.6) and Eq. (3.1.3.3), one can obtain that:

---

[20] The free-field condition means that there are no reflections.

$$p \propto \frac{1}{r} \qquad\qquad (3.1.3.4)$$

Eq. (3.1.3.4) reveals that the sound pressure is inversely proportional to the distance.

3.2. Adaptive filter

3.2.1. Introduction

The filter is a device that passing or amplifying several frequencies while attenuating other frequencies. Conventional filters are time-invariant, which performs linear operations on the input signal to generate the output signal. However, in practice, the characteristics of the noise source and acoustic environment are time-varying, which directly causes characteristics of the primary noise, e.g. the frequency content, amplitude, and phase, are changing with time (Kuo and Morgan, 1999; Kajikawa et al., 2012). To solve the time-varying issue, Burgess (1981) firstly applied the adaptive filter in the ANC system to track these variations and unknown plants. Since then, the development of the application of the adaptive filter in the ANC system is growing rapidly.

The adaptive filter consists of two parts, a digital filter, and a parameter adjustment mechanism. In the ANC system, the digital filter is to performs the desired signal processing and they can be categorized as two main categories, linear digital filters, and nonlinear digital filters. For linear digital filters, the finite impulse response (FIR) filter and the infinite impulse response (IIR) filter are two outstanding representatives and they have gained substantial popularity owing to their simplicity. For nonlinear digital filters, second-order Volterra (SOV) series (Tan and Jiang, 1997), bilinear filter (Kuo and Wu, 2005), FLANN (Das and Panda, 2004), and some soft computing engineering techniques, e.g. fuzzy systems (Chang and Shyu, 2003), fuzzy neural networks (Zhang and Gan, 2004), and recurrent neural networks (Bambang, 2008) are proposed by different researchers during the past three decades. In recent three years, researchers prefer to make several amendments based on previous proposed digital filters to improve the cancellation performance in the presence of nonlinearities, e.g. improved FLANN (IFLANN) filter and simplified IFLANN (SIFLANN) filter (Luo et al., 2018), reweighted adaptive bilinear filters (Zhu et al., 2019), and multi-channel spline adaptive filter (Patel and George, 2020).

The parameter adjustment mechanism is used for adjusting the coefficients of digital filters to minimize the residual noise signal, aims at achieving a better performance. The parameter adjustment mechanism can be classified as two domains, the linear domain, and the nonlinear domain. For the linear parameter adjustment mechanism, the least mean square (LMS) algorithm is widely used at the earlier stage due to its advantages of simplicity. However, because of the effects of the secondary path, the observed signal cannot correctly 'align' with the primary acoustic wave signal and it causes the LMS algorithm instability. Therefore, to solve this

problem, the popular filtered-x least mean square (FxLMS) algorithm was firstly proposed by Morgan in 1981, applied for ANC applications by Burgess in 1982, and derived in the context of adaptive control by Widrow and Stearns in 1985 (Kajikawa et al., 2012). The basic FxLMS algorithm is used for tuning the FIR filter and there are many kinds of variants developed by different researchers to satisfy different requirements, e.g. multidimensional ANC problems (Elliott et al., 1987), increase the convergence speed without considerably the computational load increment (Paillard et al., 1995), and improve the cancellation performance. Besides, the filtered-u least mean square (FuLMS) algorithm is another form of linear parameter adjustment mechanism and it is mainly used for tuning the IIR filter. In recent three years, researchers mainly focus on the real world application of the ANC system employed with the FxLMS algorithm and its variants, e.g. washing machine (Mazur et al., 2018), vibro-acoustic cavity (Puri et al., 2019), and vehicle interior noise (Wang et al., 2020). For the nonlinear parameter adjustment mechanism, various forms are proposed by different researchers., e.g. Volterra FxLMS algorithm, Bilinear FxLMS algorithm, radial basis function networks, fuzzy systems, fuzzy neural networks, recurrent neural networks, and the evolutionary-computing-based algorithm. A detailed summary of these nonlinear parameter adjustment mechanisms can be found in George and Panda's review paper (George and Panda, 2013). In recent three years, researchers continuously focus on proposing novel nonlinear parameter adjustment mechanisms aimed at speeding up the convergence speed and improve the cancellation performance, e.g. M-max partial update leaky bilinear filtered-error least mean square (MmLBFE-LMS) algorithm (Le et al., 2019).

3.2.2. Adaptive filter

Currently, the most common form of the adaptive filter used in the ANC field is the FIR filter using the LMS algorithm (see Figure 3.2.2.1). The FIR filter is used as the digital filter and the LMS algorithm is employed as the parameter adjustment mechanism.
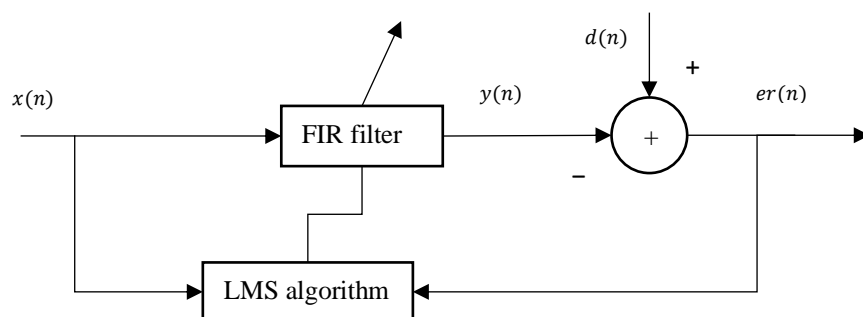
Figure 3.2.2.1. A block diagram of adaptive filter

$x(n)$ represents the reference input signal and $y(n)$ represents the output of the digital filter driven by $x(n)$.

The FIR filter output $y(n)$ can be expressed as:

$$y(n) = w_0(n)x(n) + w_1(n)x(n-1) + \cdots + w_{L-1}(n)x(n-L+1) = \sum_{i=0}^{L-1} w_i(n)x(n-i) \quad (3.2.2.1)$$

Where, the filter coefficients $w_i(n)$ are time varying and updated by the parameter adjustment mechanism. L denotes the order of the filter and n means the time index.

To simplify the Eq. (3.2.2.1), we define the input vector $X(n)$ at time n as:

$$X(n) = [x(n), x(n-1), \cdots, x(n-L+1)]^T \quad (3.2.2.2)$$

and the weight vector $w(n)$ at time n as:

$$w(n) = [w_0(n), w_1(n), \cdots, w_{L-1}(n)]^T \quad (3.2.2.3)$$

Then the output signal $y(n)$ in Eq. (3.2.2.1) can be expressed using the vector operation, which is specified as:

$$y(n) = w^T(n)X(n) \quad (3.2.2.4)$$

The $d(n)$ represents the desired signal, $er(n)$ is the difference between $d(n)$ and $y(n)$, named as the error signal, which is expressed as:

$$er(n) = d(n) - y(n) = d(n) - w^T(n)X(n) \quad (3.2.2.5)$$

To evaluate the system performance, normally, we choose the mean square value of the error signal as the cost function and it is defined as:

$$J(n) \equiv E[er^2(n)] \quad (3.2.2.6)$$

Where E represents the statistical expectation operator.

The objective is to determine the weight vector that the cost function (expressed in Eq. (3.2.2.6)) is minimized.

Substitute Eq. (3.2.2.5) into Eq. (3.2.2.6), it can be obtained that:

$$J(n) \equiv E[er(n)]^2 = E[d(n) - w^T(n)X(n)]^2$$
$$= E[d(n)]^2 - 2E[d(n)X(n)]w^T(n) + w^T(n)w(n)E[X(n)X^T(n)] \quad (3.2.2.7)$$

Eq. (3.2.2.7) illustrates that the cost function $J(n)$ is a quadratic equation of the weight vector $w(n)$ and we can obtain the minimum $w(n)$ through minimizing $J(n)$.

$\frac{\partial J(n)}{w(n)}$ is specified as:

$$\frac{\partial J(n)}{w(n)} = -2E[d(n)X(n)] + 2w^T(n)E[X(n)X^T(n)] \tag{3.2.2.8}$$

The optimal $w(n)$ minimizes the value of $J(n)$ and it can be obtained when Eq. (3.2.2.8) equals to zero, which is specified as:

$$w_{optimal}(n) = E[d(n)X(n)](E[X(n)X^T(n)])^{-1} \tag{3.2.2.9}$$

Eq. (3.2.2.9) is called as Wiener-Hoof equation and the filter whose coefficient vector satisfies Eq. (3.2.2.9) is called as Wiener filter.

In practice, we use the LMS algorithm to update the coefficients of the FIR filter to minimize the $er(n)$. A detailed description of procedures is specified as follows.

The cost function is estimated by the instantaneous squared error, which is specified as:

$$J(n) \equiv er^2(n) \tag{3.2.2.10}$$

$\frac{\partial J(n)}{w(n)}$ is specified as:

$$\frac{\partial J(n)}{w(n)} = -er(n)\frac{\partial er(n)}{w(n)} = X(n)er(n) \tag{3.2.2.11}$$

The updating equation of the weight vector $w(n)$ is achieved through a gradient-based algorithm:

$$w(n+1) = w(n) - \mu\frac{1}{2}\frac{\partial J(n)}{w(n)} \tag{3.2.2.12}$$

Substitute Eq. (3.2.2.11) into Eq. (3.2.2.12), one can obtain that:

$$w(n+1) = w(n) + \mu er(n)X(n) \tag{3.2.2.13}$$

Eq. (3.2.2.13) is called as the LMS algorithm and μ is the step size or convergence rate and its value satisfies the equation as:

$$0 < \mu < \frac{2}{L \times E[x(n)]^2} \tag{3.2.2.14}$$

3.3. Summary

This chapter provides a brief review of several relevant fundamental concepts of acoustic, e.g. sound pressure, sound intensity, and the inverse square law, and an introduction of the adaptive filter including the concept and its application in the ANC system.

In summary, the inverse square law provides solid fundamental theory for the mathematical modelling of physical paths in Chapter 4 and Chapter 5. The introduction of the adaptive filter provides an instruction on the selection of the digital filter and the parameter adjustment mechanism in Chapter 4.

Chapter 4. An adaptive feedforward ANC system for point (monopole) source cancellation

4.1. A single-input single-output (SISO) feedforward ANC system description

Figure 4.1.1 presents a schematic diagram of the proposed adaptive single-input, single-output (SISO)[21] feedforward ANC system, which is constructed based on the physical process of noise control, for point source cancellation in the free field acoustic environment. In contrast to Figure 2.3.2.3, the proposed adaptive ANC system has two novel points. The first novel point is that the system is adaptive, and it can deal with the time-varying issue, which is a big challenging problem in the application area. The second novel point is that the FIR filter is employed as the digital filter, which is simple and easy to implement. Besides, the FIR filter can also satisfy the requirement of processing the detected primary acoustic wave signal.
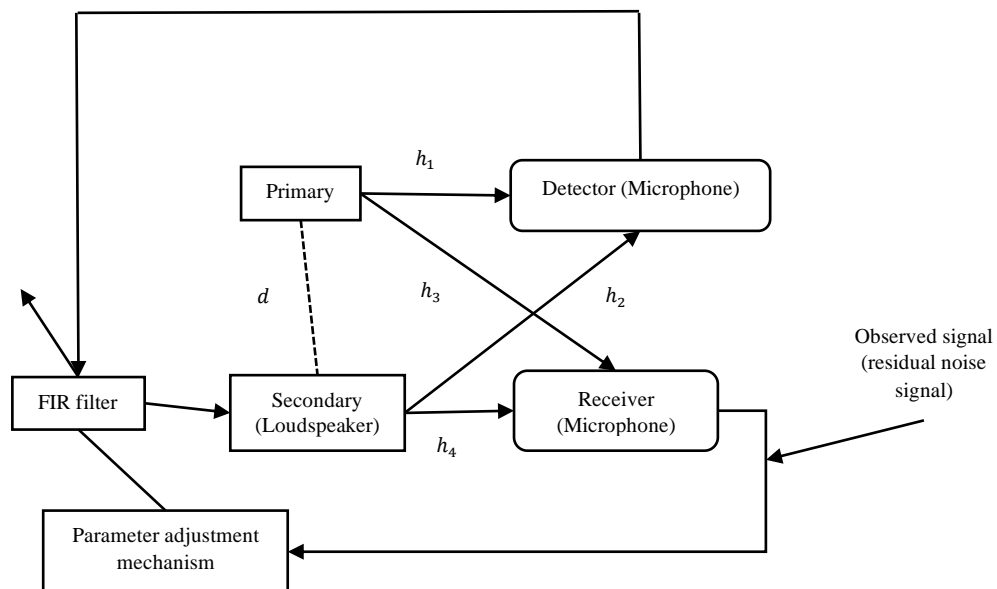
Figure 4.1.1. Schematic diagram of the adaptive SISO feedforward ANC system

The primary source emits the primary acoustic wave into the linear (non-dispersive) propagation medium to generate a primary sound field. The detector[22], placed upstream of the secondary source[23] and at a distance of h_1 and h_2 relative to the primary source and the secondary source respectively, detects the primary acoustic wave and transforms to the electrical signal, which feeds into the FIR filter for the amplitude and the phase adjustment.

---

[21] The SISO system means only one detected sensor, one error sensor is available in this ANC system, and we name it as a single-channel ANC system.

[22] Normally, the microphone is used as the detector.

[23] It is also called as the control source.

The output of the FIR filter is used for driving the loudspeaker to generate the secondary (anti-noise) acoustic wave, which superimposes the primary acoustic wave at the receiver point, placed downstream of the secondary source and at a distance of h_3 and h_4 relative to the primary source and the secondary source respectively, to generate the observed signal (the residual noise signal). The observed signal is used to evaluate the cancellation performance of the ANC system for the primary acoustic wave and if the cancellation performance is not good, it will be used as the inputs for the parameter adjustment mechanism to continuously update the coefficients of the FIR filter.

To analyse the system conveniently, we present an equivalent block diagram in Z domain (see Figure 4.1.2) and all expressions are treated as a 1×1 single element matrix.
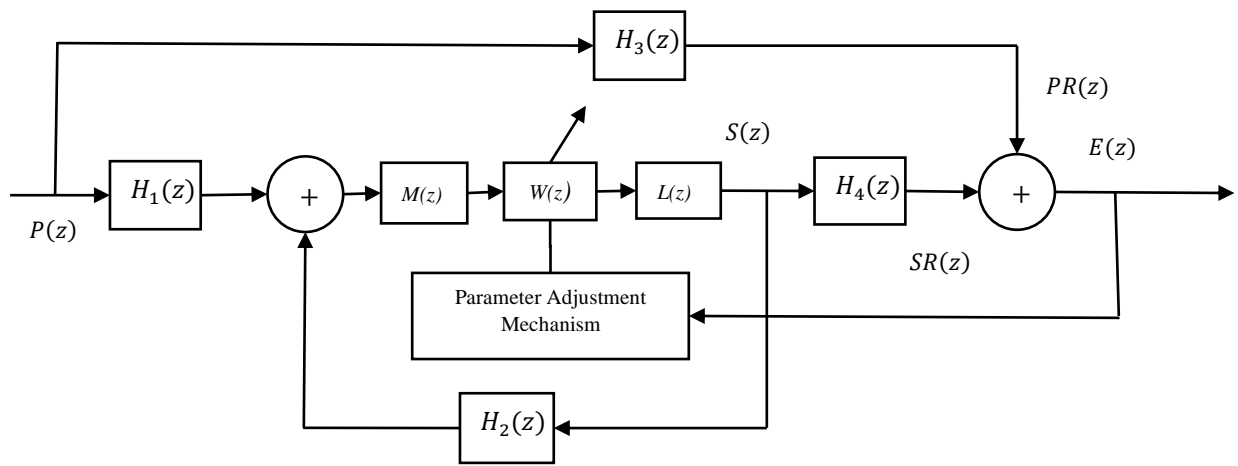
Figure 4.1.2. Block diagram of the proposed ANC system

Remark 1: Explanations of all mathematical expressions can be found in section 2.3.

The proposed adaptive ANC system is a multi-loop feedback control system, one is the acoustic feedback loop, and another is the parameter adjustment loop. With the above arrangement (see Figure 4.1.1), the secondary acoustic wave radiates to both upstream and downstream directions. The upstream radiation of the secondary acoustic wave acts as the feedback signal, and the detector detects both this signal and that from the primary source. The parameter adjustment loop is constructed based on the control law of the feedback system.

To reflect the geometric spreading of sound in the ANC system, $H_1(z)$, and $H_2(z)$ are specified as:

$$H_i(z) = \frac{constant}{h_i} e^{-F_s \ln Z t_i}, i = 1 \ and \ 2 \tag{4.1.1}$$

$$t_i = \frac{h_i}{c}, i = 1 \text{ and } 2 \tag{4.1.2}$$

F_s denotes the sampling frequency and it depends on the Nyquist–Shannon sampling theorem[24]. c is the sound velocity in the propagation medium.

Remark 2: $H_3(z)$ and $H_4(z)$ are expressed in Eq. (2.3.2.2).

Remark 3: Models of acoustic paths used in this thesis are deriving from the theoretical level. In practical experiments, we need firstly use the microphone to measure both input and output data and then construct the mathematical model based on the measured data (Janocha and Liu, 1998).

To give an analytical relationship between the geometrical configuration and the degree of cancellation (the cancellation performance), we introduce the concept of the field cancellation factor K (defined in Eq. (2.3.2.4)) into the proposed ANC system, which is specified as:

$$K = \frac{\big(PR(z)\big)^2 - \big(E(z)\big)^2}{\big(PR(z)\big)^2} = \frac{(H_3(z)P(z))^2 - \big(H_3(z)P(z) + H_4(z)S(z)\big)^2}{(H_3(z)P(z))^2} \tag{4.1.3}$$

From Figure 4.1.2, $S(z)$ can be expressed as:

$$S(z) = \frac{M(z)L(z)W(z)H_1(z)P(z)}{1 - M(z)L(z)W(z)H_2(z)} \tag{4.1.4}$$

$W(z)$ represents the Z-transform of $w^T(n)$ (expressed in Eq. (3.2.2.3)), one can obtain that:

$$W(z) = \sum_{i=0}^{L-1} w_i(n)z^{-k} \tag{4.1.5}$$

Where L is the filter order.

Combine Eq. (4.1.3) and Eq. (4.1.4), K can be expressed as:

$$K = -2\frac{H_4(z)\dfrac{M(z)L(z)W(z)H_1(z)P(z)}{1 - M(z)L(z)W(z)H_2(z)}}{H_3(z)P(z)} - \frac{\left(H_4(z)\dfrac{M(z)L(z)W(z)H_1(z)P(z)}{1 - M(z)L(z)W(z)H_2(z)}\right)^2}{\big(H_3(z)P(z)\big)^2} \tag{4.1.6}$$

Rearrange the right side of Eq. (4.1.6) and we can obtain that:

---

[24] In the field of digital signal processing, the sampling theorem is a fundamental bridge between continuous-time signals and discrete-time signals. A sufficient sample-rate is therefore anything larger than two times of the highest frequency of the original signal.

$$K = 2\frac{H_4(z)}{H_3(z)}\frac{H_1(z)}{H_2(z)}\frac{1}{1 - \frac{1}{M(z)L(z)W(z)H_2(z)}} - \left(\frac{H_4(z)}{H_3(z)}\frac{H_1(z)}{H_2(z)}\frac{1}{1 - \frac{1}{M(z)L(z)W(z)H_2(z)}}\right)^2 \quad (4.1.7)$$

Eq. (4.1.7) reveals that the K can be treated as a complex quadratic function of the $\frac{H_4(z)}{H_3(z)}\frac{H_1(z)}{H_2(z)}\frac{1}{1 - \frac{1}{M(z)L(z)W(z)H_2(z)}}$ and the value of K greatly depends on physical distance ratios $\left|\frac{h_3 h_2}{h_1 h_4}\right|$.

4.2. Geometrical constraints

In this section, we briefly discuss geometrical constraints in the form of scalar quantities.

Firstly, according to definition, the value of K is between 0[25] and 1[26], therefore, we can re-write Eq. (4.1.7) as:

$$0 < 2\frac{H_4(z)}{H_3(z)}\frac{H_1(z)}{H_2(z)}\frac{1}{1 - \frac{1}{M(z)L(z)W(z)H_2(z)}} - \left(\frac{H_4(z)}{H_3(z)}\frac{H_1(z)}{H_2(z)}\frac{1}{1 - \frac{1}{M(z)L(z)W(z)H_2(z)}}\right)^2 \quad (4.2.1)$$

$$\leq 1$$

Eq. (4.2.1) can be decomposed into two sub-equations as:

$$0 < 2\frac{H_4(z)}{H_3(z)}\frac{H_1(z)}{H_2(z)}\frac{1}{1 - \frac{1}{M(z)L(z)W(z)H_2(z)}} - \left(\frac{H_4(z)}{H_3(z)}\frac{H_1(z)}{H_2(z)}\frac{1}{1 - \frac{1}{M(z)L(z)W(z)H_2(z)}}\right)^2 \quad (4.2.2)$$

$$2\frac{H_4(z)}{H_3(z)}\frac{H_1(z)}{H_2(z)}\frac{1}{1 - \frac{1}{M(z)L(z)W(z)H_2(z)}} - \left(\frac{H_4(z)}{H_3(z)}\frac{H_1(z)}{H_2(z)}\frac{1}{1 - \frac{1}{M(z)L(z)W(z)H_2(z)}}\right)^2 \leq 1 \quad (4.2.3)$$

Solve Eq. (4.2.2) and Eq. (4.2.3), one can obtain that[27]:

$$0 < \left|\frac{H_4(z)}{H_3(z)}\frac{H_1(z)}{H_2(z)}\frac{1}{1 - \frac{1}{M(z)L(z)W(z)H_2(z)}}\right| < 2 \quad (4.2.4)$$

---

[25] No cancellation

[26] Full cancellation

[27] We use the Euclidean norm of $\frac{H_4(z)}{H_3(z)}\frac{H_1(z)}{H_2(z)}\frac{1}{1 - \frac{1}{M(z)L(z)W(z)H_2(z)}}$ to express.

$$1 - \sqrt{2} \leq \left| \frac{H_4(z)}{H_3(z)} \frac{H_1(z)}{H_2(z)} \frac{1}{1 - \frac{1}{M(z)L(z)W(z)H_2(z)}} \right| \leq 1 + \sqrt{2} \tag{4.2.5}$$

Combine Eq. (4.2.4) and Eq. (4.2.5), we can obtain that:

$$0 < \left| \frac{H_4(z)}{H_3(z)} \frac{H_1(z)}{H_2(z)} \frac{1}{1 - \frac{1}{M(z)L(z)W(z)H_2(z)}} \right| < 2 \tag{4.2.6}$$

Consider that the value of K greatly depends on physical distance ratios $\left| \frac{h_3 h_2}{h_1 h_4} \right|$, therefore, we approximately use $\left| \frac{h_3 h_2}{h_1 h_4} \right|$ to replace $\left| \frac{H_4(z)}{H_3(z)} \frac{H_1(z)}{H_2(z)} \frac{1}{1 - \frac{1}{M(z)L(z)W(z)H_2(z)}} \right|$ and one can obtain that:

$$0 < \left| \frac{h_3 h_2}{h_1 h_4} \right| < 2 \tag{4.2.7}$$

Eq. (4.2.7) is consistence with the statement provide by Kaymak et al (2006) that to have a stable ANC system, the value of $\left| \frac{h_3 h_2}{h_1 h_4} \right|$ should be smaller than 2.

Secondly, to cancel broadband random noise, the basic requirement is that the acoustic delay is longer than the electrical delay, which is specified as:

$$|h_3|^{28} > |h_1| + |h_4| \tag{4.2.8}$$

Remark 4: The physical separation between the primary source and the secondary source determines the range of the cancellation field or the range of the reinforcement field. In the duct model, the time travelled by the acoustic wave to cover the physical separation can be approximately equal to the electrical delay. In this section, we ignore the physical separation between two sources and will do a detailed analysis in the following section.

According to the relationship between the geometric mean and arithmetic mean, one can obtain that:

$$|h_3| > |h_1| + |h_4| \geq 2\sqrt{|h_1 h_4|} \tag{4.2.9}$$

Where only $h_1 = h_4$, then the notation $=$ exist.

Based on the property of inequality, multiplication, we can obtain that:

$$|h_3 h_2| > 2|h_2|\sqrt{|h_1 h_4|} \tag{4.2.10}$$

---

[28] Here, the minimum value of $|h_3|$ is $d + |h_1| + |h_4|$

Then $\left|\frac{h_3 h_2}{h_1 h_4}\right|$ can be written as:

$$\left|\frac{h_3 h_2}{h_1 h_4}\right| > \frac{2|h_2|\sqrt{|h_1 h_4|}}{|h_1 h_4|} \tag{4.2.11}$$

Consider that $\frac{2|h_2|\sqrt{|h_1 h_4|}}{|h_1 h_4|}$ can be simplified as $\frac{2|h_2|}{\sqrt{|h_1 h_4|}}$, Eq. (4.2.11) can be simplified as:

$$\left|\frac{h_3 h_2}{h_1 h_4}\right| > \frac{2|h_2|}{\sqrt{|h_1 h_4|}} \tag{4.2.12}$$

Eq. (4.2.7) and Eq. (4.2.12) are two basic and main principles of geometrical constraints.

According to Eq. (4.2.9), it is clear that $|h_3|$ is greater than $|h_4|$ but we do not have a clear relationship between $|h_1|$ and $|h_2|$, which causes an uncertainty value of $\left|\frac{h_3 h_2}{h_1 h_4}\right|$. Therefore, the following section will provide detailed discussions about geometrical constraints under different values of $\left|\frac{h_3 h_2}{h_1 h_4}\right|$.

4.2.1. The distance ratio greater than one

Combine Eq. (4.2.7), we can obtain the following mathematical equation under this condition as:

$$1 < \left|\frac{h_3 h_2}{h_1 h_4}\right| < 2 \tag{4.2.13}$$

Re-write Eq. (4.2.13), we can obtain that:

$$\left|\frac{h_1}{h_2}\right| < \left|\frac{h_3}{h_4}\right| < 2\left|\frac{h_1}{h_2}\right| \tag{4.2.14}$$

Consider $\left|\frac{h_3}{h_4}\right| > 1$, it follows that:

$$1 < 2\left|\frac{h_1}{h_2}\right| \tag{4.2.15}$$

Solve Eq. (4.2.15), we can obtain that:

$$|h_1| > \frac{|h_2|}{2} \tag{4.2.16}$$

Now, we need consider two conditions that $|h_1| > |h_2|$ and $|h_1| < |h_2|$.

$\boldsymbol{|h_1| > |h_2|}$: Under this condition, we can obtain that:

$$1 < \left|\frac{h_1}{h_2}\right| < \left|\frac{h_3}{h_4}\right| < 2 < 2\left|\frac{h_1}{h_2}\right| \tag{4.2.17}$$

Combine Eq. (4.2.12) and Eq. (4.2.17), to obtain the range of $\left|\frac{h_3}{h_4}\right|$, it is necessary to compare $\left|\frac{h_1}{h_2}\right|$ and

$\frac{2|h_2|}{\sqrt{|h_1 h_4|}}$.

The first condition is $\frac{2|h_2|}{\sqrt{|h_1 h_4|}} \geq \left|\frac{h_1}{h_2}\right|$, it follows that:

$$2|h_2|^2 \geq |h_1|\sqrt{|h_1 h_4|} \tag{4.2.18}$$

Consider that $|h_1| > |h_2|$, it can obtain that:

$$|h_1|\sqrt{|h_1 h_4|} > |h_2|\sqrt{|h_2 h_4|} \tag{4.2.19}$$

Combine Eq. (4.2.18) and Eq. (4.2.19), we can obtain the relationship between $|h_2|$ and $|h_4|$ as:

$$2|h_2|^2 > |h_2|\sqrt{|h_2 h_4|} \Rightarrow |h_4| < 4|h_2| \tag{4.2.20}$$

Then the range of $\left|\frac{h_3}{h_4}\right|$ can be expressed as:

$$\frac{2|h_2|}{\sqrt{|h_1 h_4|}} < \left|\frac{h_3}{h_4}\right| < 2\left|\frac{h_1}{h_2}\right|, when\ |h_1| > |h_2| \& |h_4| < 4|h_2| \tag{4.2.21}$$

The second condition is $\frac{2|h_2|}{\sqrt{|h_1 h_4|}} < \left|\frac{h_1}{h_2}\right|$, we can obtain that:

$$\frac{2|h_2|}{\sqrt{|h_1 h_4|}} < \left|\frac{h_1}{h_2}\right| \Rightarrow 2|h_2|^2 < |h_1|\sqrt{|h_1 h_4|} \tag{4.2.22}$$

Then the range of $\left|\frac{h_3}{h_4}\right|$ can be expressed as:

$$\left|\frac{h_1}{h_2}\right| < \left|\frac{h_3}{h_4}\right| < 2\left|\frac{h_1}{h_2}\right|, when\ |h_1| > |h_2| \& 2|h_2|^2 < |h_1|\sqrt{|h_1 h_4|} \tag{4.2.23}$$

$\boldsymbol{|h_1| < |h_2|}$: Combine Eq. (4.2.16), we can obtain that:

$$\frac{|h_2|}{2} < |h_1| < |h_2| \tag{4.2.24}$$

Eq. (4.2.17) can be re-expressed as:

$$\frac{1}{2} < \left|\frac{h_1}{h_2}\right| < 1 < \left|\frac{h_3}{h_4}\right| < 2\left|\frac{h_1}{h_2}\right| < 2 \tag{4.2.25}$$

Combine Eq. (4.2.12) and Eq. (4.2.25), to obtain the range of $\left|\frac{h_3}{h_4}\right|$, we need to compare the value of

$\frac{2|h_2|}{\sqrt{|h_1 h_4|}}$ and 1.

The first condition is $\frac{2|h_2|}{\sqrt{|h_1 h_4|}} \geq 1$, it follows that:

$$\frac{2|h_2|}{\sqrt{|h_1 h_4|}} \geq 1 \Rightarrow |h_2| \geq \frac{\sqrt{|h_1 h_4|}}{2} \tag{4.2.26}$$

Substitute $|h_1| > \frac{|h_2|}{2}$ into Eq. (4.2.26), we can obtain that:

$$|h_4| < 8|h_2| \tag{4.2.27}$$

Then we can obtain the range of $\left|\frac{h_3}{h_4}\right|$ as:

$$\frac{2|h_2|}{\sqrt{|h_1 h_4|}} < \left|\frac{h_3}{h_4}\right| < 2\left|\frac{h_1}{h_2}\right|, when\ |h_1| < |h_2| \& |h_4| < 8|h_2| \tag{4.2.28}$$

The second condition is $\frac{2|h_2|}{\sqrt{|h_1 h_4|}} < 1$, we can obtain that:

$$\frac{2|h_2|}{\sqrt{|h_1 h_4|}} < 1 \Rightarrow |h_2| < \frac{\sqrt{|h_1 h_4|}}{2} \tag{4.2.29}$$

Consider the condition of $|h_2| > |h_1|$, we can obtain that:

$$|h_4| > 4|h_1| \tag{4.2.30}$$

Then we can obtain the range of $\left|\frac{h_3}{h_4}\right|$ as:

$$1 < \left|\frac{h_3}{h_4}\right| < 2\left|\frac{h_1}{h_2}\right|, when\ |h_1| < |h_2| \& |h_4| > 4|h_1| \tag{4.2.31}$$

4.2.2. The distance ratio equal to one

Under this condition, one can obtain that:

$$\left|\frac{h_3}{h_4}\right| = \left|\frac{h_1}{h_2}\right| \tag{4.2.32}$$

Combine Eq. (4.2.12) and Eq. (4.2.32), it follows that:

$$|h_1 h_4| = |h_2 h_3| > 2|h_2|\sqrt{|h_1 h_4|} \Rightarrow |h_2| < \frac{\sqrt{|h_1 h_4|}}{2} \tag{4.2.33}$$

Consider the condition of $|h_1| > |h_2|$, one can obtain:

$$\begin{cases} |h_2| \le \dfrac{\sqrt{|h_1 h_4|}}{2}, when\ 4|h_1| \ge |h_4| \\ |h_2| < |h_1|, when\ 4|h_1| < |h_4| \end{cases} \tag{4.2.34}$$

4.2.3. The distance ratio smaller than one

The relationship between these two distance ratios under this condition is that:

$$\left| \dfrac{\left|\dfrac{h_3}{h_4}\right|}{\dfrac{h_1}{h_2}} \right| < 1 \tag{4.2.35}$$

Consider Eq. (4.2.12) and Eq. (4.2.35), we can obtain that:

$$|h_1 h_4| = |h_2 h_3| > 2|h_2|\sqrt{|h_1 h_4|} \Rightarrow |h_2| < \dfrac{\sqrt{|h_1 h_4|}}{2} \tag{4.2.36}$$

Where results are the same as Eq. (4.2.34).

In summary, constraints for physical distance are summarized as follows:

$$\left|\dfrac{h_3 h_2}{h_1 h_4}\right| = \begin{cases} 1 < \left|\dfrac{h_3 h_2}{h_1 h_4}\right| < 2 \begin{cases} |h_1| > |h_2|, \begin{cases} \dfrac{2|h_2|}{\sqrt{|h_1 h_4|}} < \left|\dfrac{h_3}{h_4}\right| < 2\left|\dfrac{h_1}{h_2}\right|, |h_4| < 4|h_2| \\ \left|\dfrac{h_1}{h_2}\right| < \left|\dfrac{h_3}{h_4}\right| < 2\left|\dfrac{h_1}{h_2}\right|, 2|h_2|^2 < |h_1|\sqrt{|h_1 h_4|} \end{cases} \\ \dfrac{|h_2|}{2} < |h_1| < |h_2|, \begin{cases} \dfrac{2|h_2|}{\sqrt{|h_1 h_4|}} < \left|\dfrac{h_3}{h_4}\right| < 2\left|\dfrac{h_1}{h_2}\right|, |h_4| < 8|h_2| \\ \left|\dfrac{h_1}{h_2}\right| < \left|\dfrac{h_3}{h_4}\right| < 2\left|\dfrac{h_1}{h_2}\right|, |h_4| > 4|h_1| \end{cases} \end{cases} \\ \left|\dfrac{h_3 h_2}{h_1 h_4}\right| = 1 \begin{cases} |h_2| \le \dfrac{\sqrt{|h_1 h_4|}}{2}, when\ 4|h_1| \ge |h_4| \\ |h_2| < |h_1|, when\ 4|h_1| < |h_4| \end{cases} \\ \left|\dfrac{h_3 h_2}{h_1 h_4}\right| < 1 \begin{cases} |h_2| \le \dfrac{\sqrt{|h_1 h_4|}}{2}, when\ 4|h_1| \ge |h_4| \\ |h_2| < |h_1|, when\ 4|h_1| < |h_4| \end{cases} \end{cases} \tag{4.2.37}$$

4.3. Locus of system components in the two-dimensional Euclidean space

Physical constraints provided in Eq. (4.2.37) are in the form of scalar quantities and they can only reflect variations on magnitude. However, in practice, different geometrical configurations cause changes in both magnitude and direction, therefore, in this section, we aim to employ vector quantities to express physical constraints (described in Eq. (4.2.37)), which provides a clearer insight on the locus of system components under different geometrical constraints in the two-dimensional Euclidean space.

Remark 5: System components contain the primary source, the secondary source, the detector, and the receiver. We will use the concept of system components in the following discussion.

Based on introductions of the proposed adaptive ANC system provided in section 4.1, we define the primary source as the original point and coordinates of the secondary source, the detector and the receiver are (u, v), (x_1, y_1) and (x_2, y_2, z_2) respectively. Figure 4.3.1 presents geometrical configuration of system components according to the practical process of the active noise control.
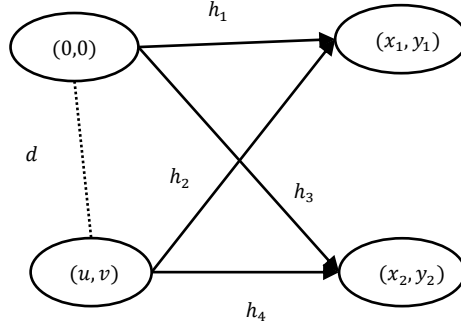
Figure 4.3.1. Coordinates of system components in the two-dimensional Cartesian coordinate system

To describe physical distance precisely, we define four vector quantities and they are specified as:

$$\begin{cases} \vec{h_1} = (x_1)\vec{m} + (y_1)\vec{n} \\ \vec{h_2} = (x_1 - u)\vec{m} + (y_1 - v)\vec{n} \\ \vec{h_3} = (x_2)\vec{m} + (y_2)\vec{n} \\ \vec{h_4} = (x_2 - u)\vec{m} + (y_2 - v)\vec{n} \end{cases} \tag{4.3.1}$$

Where $\vec{m}$, and $\vec{n}$ are standard vectors in the positive x, and y axis respectively.

Assume the physical separation between two sources is d and d is known, one can obtain that:

$$\sqrt{u^2 + v^2 + w^2} = d \tag{4.3.2}$$

Where, the range of u, and v is $(0, d)$.

Remark 6: The physical separation between two sources in the feedforward ANC system determines the phase delay and the value of d should be determined according to the practical problems.

4.3.1. The distance ratio is greater than one

Define the distance ratio of $\left|\frac{\vec{h_3}}{\vec{h_4}}\right|$ is a and the distance ratio of $\left|\frac{\vec{h_1}}{\vec{h_2}}\right|$ is b, where $a, b \epsilon R^+$.

Combine Eq. (4.3.1), one can obtain that:

$$\frac{\sqrt{(x_2)^2 + (y_2)^2}}{\sqrt{(x_2 - u)^2 + (y_2 - v)^2}} = a \qquad (4.3.3)$$

$$\frac{\sqrt{(x_1)^2 + (y_1)^2}}{\sqrt{(x_1 - u)^2 + (y_1 - v)^2}} = b \qquad (4.3.4)$$

According to statements in section 4.2, we can obtain that:

$$1 < \frac{a}{b} < 2 \qquad (4.3.5)$$

Where $a > 1$ and the value of b is unknown.

Therefore, the relationship between a and b can be broadly classified into three categories, $2b > a > b > 1$, $2 > a > b \& b = 1$ and $2b > a > 1 > b > \frac{1}{2}$.

$\boldsymbol{2b > a > b > 1}$: Apply the condition into Eq. (4.3.3) and Eq. (4.3.4), one can obtain that:

$$\left(x_2 - \frac{a^2 u}{a^2 - 1}\right)^2 + \left(y_2 - \frac{a^2 v}{a^2 - 1}\right)^2 = \frac{a^2}{(a^2 - 1)^2} d^2 \qquad (4.3.6)$$

$$\left(x_1 - \frac{b^2 u}{b^2 - 1}\right)^2 + \left(y_1 - \frac{b^2 v}{b^2 - 1}\right)^2 = \frac{b^2}{(b^2 - 1)^2} d^2 \qquad (4.3.7)$$

Eq. (4.3.6) is the locus equation of the receiver, Eq. (4.3.7) is the locus equation of the detector and both equations are circle equations.

We assume symbol A is the central point of the circle governed by Eq. (4.3.6) and r_A represents the radius. Symbol B is the central point of the circle governed by Eq. (4.3.7) and r_B represents the radius. The coordinates of A and B are $(\frac{a^2 u}{a^2 - 1}, \frac{a^2 v}{a^2 - 1})$ and $(\frac{b^2 u}{b^2 - 1}, \frac{b^2 v}{b^2 - 1})$ respectively. Both A and B are in the positive octant because of $a > b > 1$.

To identify the relationship between these two circles, firstly, we define two vector quantities as:

$$\begin{cases} \overrightarrow{OA} = \left(\dfrac{a^2 u}{a^2 - 1}, \dfrac{a^2 v}{a^2 - 1}\right) = \dfrac{a^2}{a^2 - 1}(u, v) \\ \overrightarrow{OB} = \left(\dfrac{b^2 u}{b^2 - 1}, \dfrac{b^2 v}{b^2 - 1}\right) = \dfrac{b^2}{b^2 - 1}(u, v) \end{cases} \qquad (4.3.8)$$

According to the property of vector quantities, we can obtain that:

$$\overrightarrow{OA} = \frac{a^2 b^2 - a^2}{a^2 b^2 - b^2} \overrightarrow{OB} \tag{4.3.9}$$

Eq. (4.3.9) implies that B, A, and O are collinear and we can find that A is closer to O in comparison with B because of $a > b$.

Secondly, we compare r_A and r_B. The difference between r_A and r_B is specified as:

$$r_A - r_B = \frac{(ab + 1)(b - a)d}{(a^2 - 1)(b^2 - 1)} \tag{4.3.10}$$

It is easy to obtain that $r_A < r_B$ because of $a > b$.

Thirdly, we need to check whether these two circles have any intersection parts.

The distance between A and B is:

$$\left|\overrightarrow{AB}\right| = \frac{(a^2 - b^2)d}{(a^2 - 1)(b^2 - 1)} \tag{4.3.11}$$

The summation of two radius is:

$$r_A + r_B = \frac{(ab - 1)(a + b)d}{(a^2 - 1)(b^2 - 1)} \tag{4.3.12}$$

The difference between Eq. (4.3.11) and Eq. (4.3.12) is:

$$r_A + r_B - \left|\overrightarrow{AB}\right| = \frac{(ab - a + b - 1)(a + b)d}{(a^2 - 1)(b^2 - 1)} = \frac{(a + 1)(b - 1)(a + b)d}{(a^2 - 1)(b^2 - 1)} > 0 \tag{4.3.13}$$

Eq. (4.3.13) illustrates there is no intersection part between these two circles.

Combine Eq. (4.3.8) to Eq. (4.3.13), we present the relationship between these two circles in Figure 4.3.2.
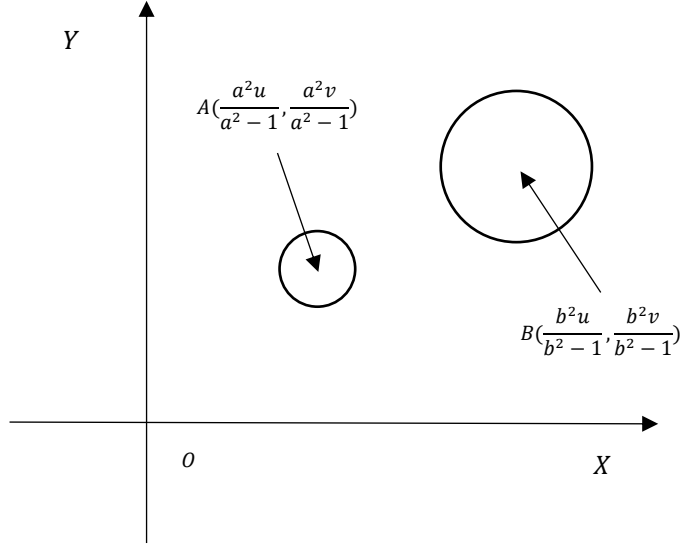
Figure 4.3.2. Relationship between two loci ($2b > a > b > 1$)

Remark 7: In this thesis, we do not consider the condition that the circle have any intersections with *x*-axis or *y*-axis.

$2 > a > b$ & $b = 1$: Substitute $b = 1$ in Eq. (4.3.4), one can obtain that:

$$\frac{\sqrt{(x_1)^2 + (y_1)^2}}{\sqrt{(x_1 - u)^2 + (y_1 - v)^2}} = 1 \tag{4.3.14}$$

Simplify Eq. (4.3.14), one can obtain that:

$$\frac{2u}{d^2}x_1 + \frac{2v}{d^2}y_1 = 1 \tag{4.3.15}$$

Eq. (4.3.15) is the locus equation of the detector when $b = 1$. It describes a line in two-dimensional space and coordinates of intersects points located within the positive octant are $(\frac{d^2}{2u}, 0)$, and $(0, \frac{d^2}{2v})$ respectively.

Now, we need to identify the relationship between the line described in Eq. (4.3.15) and the circle described in Eq. (4.3.6).

The shortest distance d_A from the point A to the line is:

$$d_A = \frac{\left| 2u \times \left(\frac{a^2 u}{a^2 - 1}\right) + 2v \times \frac{a^2 v}{a^2 - 1} - d^2 \right|}{\sqrt{4u^2 + 4v^2}} = \frac{(a^2 + 1)d}{2(a^2 - 1)} \tag{4.3.16}$$

The difference between d_A and r_A is:

52

$$difference = d_A - r_A = \frac{(a^2 + 1)d}{2(a^2 - 1)} - \frac{ad}{a^2 - 1} = \frac{(a - 1)^2 d}{2(a^2 - 1)} \tag{4.3.17}$$

Consider that $2 > a > 1$, the difference is positive, and it implies that there are no intersection points between the line and the circle.

Figure 4.3.3 presents the relationship between the line and the circle.
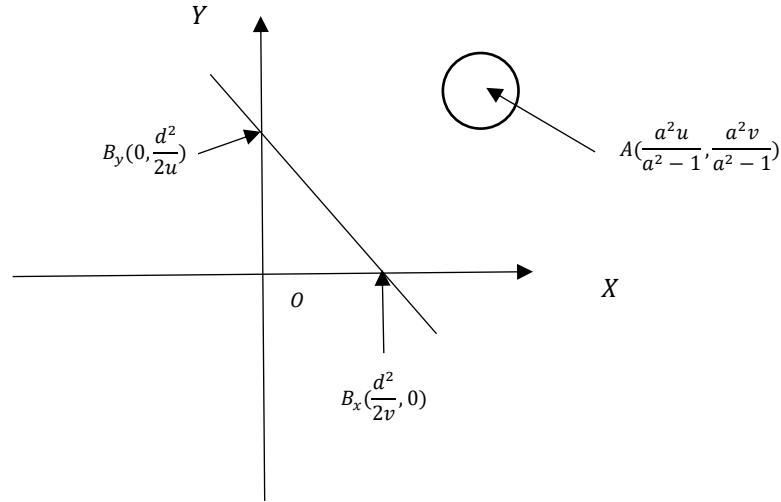
Figure 4.3.3. Relationship between two loci ($2 > a > b$ & $b = 1$)

$2b > a > 1 > b > \frac{1}{2}$: Apply $b < 1$ in Eq. (4.3.4), the locus equation of the detector is:

$$\left(x_1 + \frac{b^2 u}{1 - b^2}\right)^2 + \left(y_1 + \frac{b^2 v}{1 - b^2}\right)^2 = \frac{b^2}{(1 - b^2)^2} d^2 \tag{4.3.18}$$

Eq. (4.3.18) describes a circle equation.

We assume the center point as B_1 and the radius is r_{B_1}. The coordinate of B_1 is $(-\frac{b^2 u}{1-b^2}, -\frac{b^2 v}{1-b^2})$, which implies that the center point is located within the negative quadrant because of $b < 1$.

Now, we need to identify the relationship between the circle governed in Eq. (4.3.6) and the circle governed in Eq. (4.3.18).

The difference between two central points is:

$$|AB_1| = \frac{(a^2 - b^2)d}{(a^2 - 1)(1 - b^2)} \tag{4.3.19}$$

The summation of two radius is:

53

$$|r_A + r_{B_1}| = \frac{(ab+1)(a-b)d}{(a^2-1)(1-b^2)} \qquad (4.3.20)$$

The difference between $|r_A + r_{B_1}|$ and $|AB_1|$ is:

$$|r_A + r_{B_1}| - |AB_1| = \frac{(ab+1)(a-b)d}{(a^2-1)(1-b^2)} - \frac{(a^2-b^2)d}{(a^2-1)(1-b^2)} = \frac{(a-1)(1-b)(a-b)d}{(a^2-1)(1-b^2)} > 0 \quad (4.3.21)$$

Eq. (4.3.21) implies that there are no intersection points of these two circles (see Figure 4.3.4).
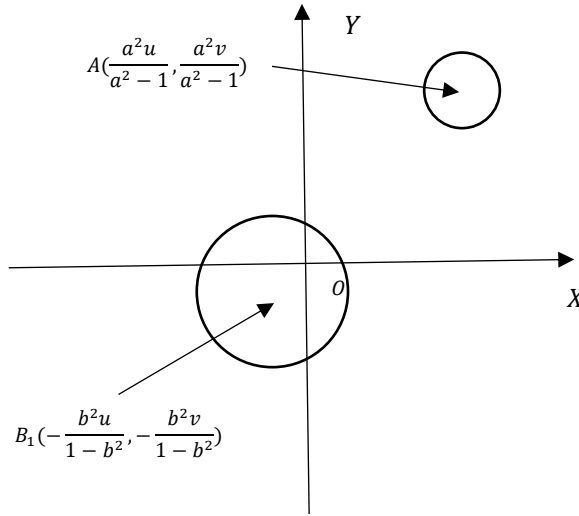
Figure 4.3.4. Relationship between two loci $(2b > a > 1 > b > \frac{1}{2})$

4.3.2. The distance ratio is one

Under this condition, we can obtain that $a = b > 1$, therefore, both detector and receiver satisfy the same locus equation as:

$$\left(x_i - \frac{c^2 u}{c^2-1}\right)^2 + \left(y_i - \frac{c^2 v}{c^2-1}\right)^2 = \frac{c^2}{(c^2-1)^2}d^2, \text{where i} = 1,2 \qquad (4.3.22)$$

Where $c = a = b$ and we present in Figure 4.3.5.
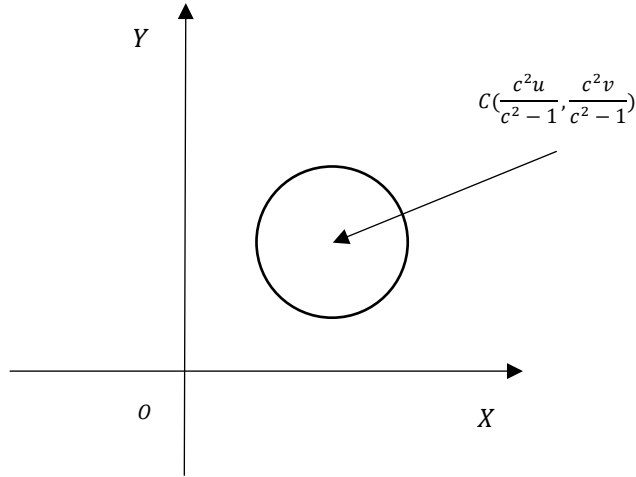
Figure 4.3.5. The locus equation ($a = b > 1$)

Remark 8: Under this distance condition, the detector and the receiver cannot be overlapped as the proposed ANC system is feedforward and we do not consider the feedback ANC system in this paper.

4.3.3. The distance ratio is smaller than one

Under this condition, the relationship between a and b is $2 > b > a > 1$.

Consider Eq. (4.3.6) to Eq. (4.3.13), we present the relationship between two loci in Figure 4.3.6.
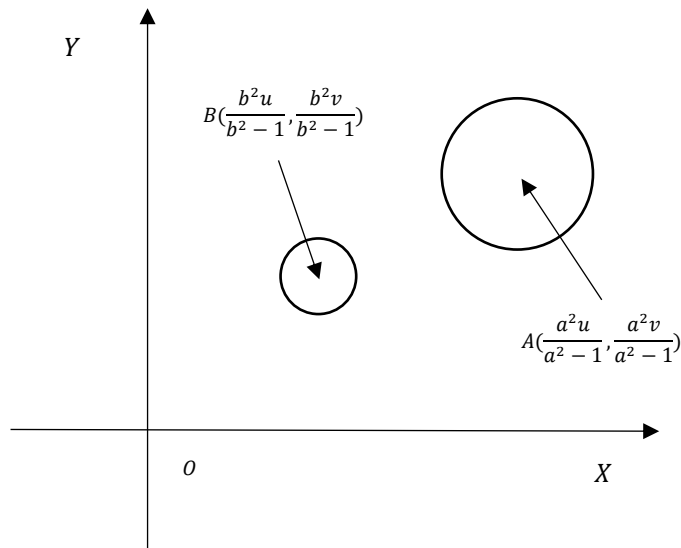
Figure 4.3.6. Relationship between two loci ($2 > b > a > 1$)

4.4. Adaptive filter identification

Instead of random initialization, we adopt the recursive least mean square (RLS) algorithm to obtain the coefficients and use them as the initial coefficients of the adaptive filter. This step aims to reduce computational resources and increase the cancellation performance.

In this section, we use the FIR filter as an example.

Define a cost function as:

$$J(w) = \sum_{n=0}^{L-1} (y(n) - w^T(n)X(n))^2 \tag{4.4.1}$$

$X(n)$ is the input vector[29] and $w(n)$ is the weight vector[30].

Eq. (4.4.1) reveals that $J(w)$ is a quadratic function of w. To obtain the optimal value of w, we do the first derivative of $J(w)$ with respect to w, it follows that:

$$\frac{\partial J(w)}{\partial w} = 2 \sum_{n=0}^{L-1} (y(n) - w^T(n)X(n)) (-\sum_{n=0}^{L-1} X(n)) \tag{4.4.2}$$

Let Eq. (4.4.2) equals to zero and we can obtain the estimated weight vector $\widehat{w(n)}$, which is given as:

$$\widehat{w(n)} = (\sum_{n=0}^{L-1} w^T(n)w(n))^{-1} \sum_{n=0}^{L-1} w^T(n)w(n) = (W_n^T W_n)^{-1} W_n Y_n \tag{4.4.3}$$

W_n and Y_n are expressed as:

$$W_n = [w(0), w(1), \dots, w(n)]^T \tag{4.4.4}$$

$$Y_n = [y(0), y(1), \dots, y(n)]^T \tag{4.4.5}$$

Define a new matrix $P(n)$, it follows that:

$$P^{-1}(n) = \sum_{n=0}^{L-1} w^T(n)w(n) \tag{4.4.6}$$

Substitute Eq. (4.4.6) into Eq. (4.4.3), one can obtain that:

$$\widehat{w(n)} = P^{-1}(n)W_n Y_n = P^{-1}(n)[W_{n-1}, w(n)]^T [Y_{n-1}, y(n)] \tag{4.4.7}$$

After iteration process, we can obtain the RLS algorithm (Ding and ding, 2010) of the FIR filter identification is:

$$\begin{cases} \widehat{w}(n) = \widehat{w}(n-1) + L(n)[y(n) - \widehat{w}^T(n-1)X(n)] \\ L(n) = P(n-1)X(n)[1 + X^T(n)P(n-1)X(n)]^{-1} \\ P(n) = [I - L(n)X^T(n)]P(n-1), P(0) = 10^6 I \end{cases} \tag{4.4.8}$$

---

[29] Defined in Eq. (3.2.2.2)

[30] Defined in Eq. (3.2.2.3).

4.5. Nonlinear filter and nonlinear parameter adjustment mechanism

4.5.1. Nonlinear filter

It is well-known that Volterra filters have an excellent performance in noise reduction in the presence of the nonlinearities. The Volterra filter[31] is based on an input-output relation expressed in the form of a discrete Volterra series, which can be regarded as a Taylor series with memory in practice.

The input-output relationship of a discrete, and causal second-order truncated Volterra (SOV) series in the time domain is specified as (He et al., 2019):

$$y(n) = \sum_{i=0}^{N-1} w_1(i)x(n-i) + \sum_{i=0}^{N-1}\sum_{j=i}^{N-1} w_2(i,j)x(n-i)x(n-j) \qquad (4.5.1.1)$$

Where $x(n)$ and $y(n)$ represent the input and the output signals of the SOV respectively, $w_1(i)$ and $w_2(i,j)$ represent the coefficients, n denotes the time index, and N represents the memory length.

Consider the definition of causality, one can obtain that:

$$\begin{cases} w_1(i) = 0, for\ i < 0 \\ w_2(i,j) = 0, for\ i,j < 0 \end{cases} \qquad (4.5.1.2)$$

The input signal vector $X(n)$ in Eq. (4.5.1.1) can be specified as:

$$X(n) = [\sum_{i=0}^{N-1} x(n-i), \sum_{i=0}^{N-1}\sum_{j=i}^{N-1} x(n-i)x(n-j)]^T$$

$$\qquad (4.5.1.3)$$

$$= [x(n),\cdots,x(n-N+1),x^2(n),\cdots,x^2(n-N+1),x(n)x(n-1),\cdots,x(n$$

$$-N+2)x(n-N+1)]^T$$

The weight vector $w(n)$ in Eq. (4.5.1.1) can be specified as:

$$w(n) = [\sum_{i=0}^{N-1} w_1(i), \sum_{i=0}^{N-1}\sum_{j=i}^{N-1} w_2(i,j)]^T$$

$$\qquad (4.5.1.4)$$

$$= [w_1(0),\cdots,w_1(N),w_2(0,0),\cdots,w_2(N,N),w_2(0,1),\cdots,w_2(N-1,N)]^T$$

Obviously, the length of $\sum_{i=0}^{N-1} x(n-i)$ is N and the length of $\sum_{i=0}^{N-1}\sum_{j=i}^{N-1} x(n-i)x(n-j)$ is $\frac{N(N+1)}{2}$. It is noted that the length of $X(n)$ is $\frac{N(N+3)}{2}$.

If we re-write Eq. (4.5.1.1) as:

---

[31] The Volterra filter belongs to the field of nonlinear filer and sometimes it is called as polynomial filter.

$$y(n) = \sum_{i=0}^{N-1} w_1(i)x(n-i) + \sum_{i=0}^{N-1} w_{2,0}(i)x^2(n-i) + \sum_{i=0}^{N-2} w_{2,1}(i)x(n-i)\,x(n-i-1) + \cdots$$
$$+ w_{2,N-1}(0)\,x(n)x(n-N+1) \tag{4.5.1.5}$$

Apply *Z*-transformation in Eq. (4.5.1.5), it yields (Tan and Jiang, 1997):

$$Y(z) = W_1(z)X_1(z) + \sum_{m=0}^{N-1} W_{2,m}(z)X_{2,m}(z) \tag{4.5.1.6}$$

Eq. (4.5.1.6) realizes the SOV filter by FIR multichannel[32].

Compare Eq. (4.5.1.1) and Eq. (3.2.2.1), we can find that the length of the weight vector of the SOV is larger than the FIR filter under the condition of the same memory length.

4.5.2. Adaptive network-based fuzzy inference system (ANFIS) technique

Firstly, we use the adaptive network-based fuzzy inference system (ANFIS) technique, proposed by Jang in 1993, as the parameter adjustment mechanism. The ANFIS is a kind of neuro-fuzzy technique and it uses Takagi–Sugeno–Kang (TSK)-type fuzzy inference system (FIS) in a five-layered network structure. The TSK-type FIS is the most useful fuzzy inference system and is a powerful tool for modelling of nonlinear dynamic systems. The main advantage of TSK system modelling is that it is a 'multimodal' approach which can combine linear submodels to describe the global behaviour of a complete complex nonlinear dynamic system (Shihabudheen and Pillai, 2018). The ANFIS technique defines two sets of parameters namely premise parameters and consequent parameters and the fuzzy if–then rules define the relationship between the two sets of parameters.

Figure 4.5.2.1 presents a classical structure of the ANFIS technique with two inputs and one output. The first order TSK-type FIS is employed and the fuzzy if-then rules are specified as:

$$\begin{aligned} Rule\ 1{:}\ &If\ x\ is\ M_1\ and\ y\ is\ N_1, then\ f_1 = p_1 \times x + q_1 \times y + s_1 \\ Rule\ 2{:}\ &If\ x\ is\ M_2\ and\ y\ is\ N_2, then\ f_2 = p_2 \times \mathrm{x} + q_2 \times \mathrm{y} + s_2 \end{aligned} \tag{4.5.2.1}$$

---

[32] It transforms the nonlinear second-order Volterra filter to a multichannel input linear filter.
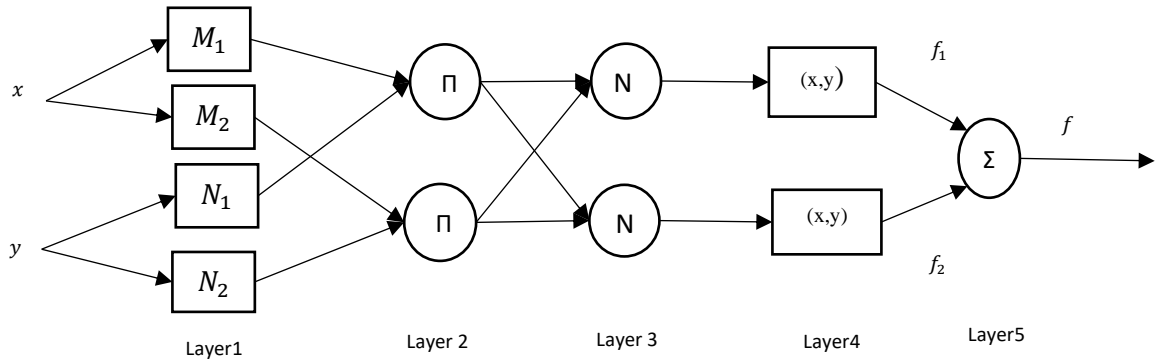
Figure 4.5.2.1. The architecture of the ANFIS

In practice, the ANFIS technique has a broad range of applications because of its efficiency, e.g. medical service (Abbas, 2018) and fault diagnosis (Zhao et al., 2014), and several kinds of variants are proposed by different researchers, e.g. hybrid particle swarm optimization (PSO) and subtractive clustering (SC)-based ANFIS technique (Chen et al., 2013) and regularized extreme learning adaptive neuro-fuzzy algorithm (Shihabudheen and Pillai, 2020).

In this paper, to low the computational load, we choose the conventional type-I ANFIS technique as the parameter adjustment mechanism to adjust the coefficients of the digital filter. The residual noise signal e and the change of the residual noise signal Δe are used as two inputs for the ANFIS technique, and the output is the change in filter coefficients Δw. Table 4.5.2.1, Table 4.5.2.2, and, Table 4.5.2.3 presents the linguistic values of $e, \Delta e,$ and Δw respectively.

Table 4.5.2.1. Linguistic values of e

Negative Big	Negative Medium	Negative Small	Zero	Positive Small	Positive Medium	Positive Big
NB	NM	NS	Z	PS	PM	PB

Table 4.5.2.2. Linguistic values of Δe

Decreasing Fast	Decreasing Slow	No Change	Increasing Slow	Increasing Fast
DF	DS	NC	IS	IF

Table 4.5.2.3. Linguistic values of $\varDelta w$

Negative Big	Negative Small	Zero	Positive Small	Positive Big
NB	NS	Z	PS	PB

The following section provides a detailed introduction of each layer.

Layer 1: Function of node in this layer is to accept the external crisp value and use the Gaussian-shaped membership functions (MFs) to obtain the corresponding membership value. Type-I indicates that the MFs value are crisp. Expressions of the Gaussian-shaped MFs for e and $\varDelta e$ are:

$$\mu_{M_i}(e) = \exp\left(-\left(\frac{e - c_i}{2\delta_i}\right)\right), i = 1,2,3,4,5,6,7 \qquad (4.5.2.2)$$

$$\mu_{N_j}(\varDelta e) = \exp\left(-\left(\frac{\varDelta e - c_j}{2\delta_j}\right)\right), j = 1,2,3,4,5 \qquad (4.5.2.3)$$

M_i and N_j are linguistic labels of e and $\varDelta e$ respectively (see Table 4.5.2.1 and Table 4.5.2.2), c_j and δ_j are parameters of the Gaussian-shaped MFs and $\{c_j, \delta_j\}$ is the premise parameter set.

The output for each node in this layer is:

$$L_i^1 = \mu_{M_i}(e), i = 1,2,3,4,5,6,7 \qquad (4.5.2.4)$$

$$L_j^1 = \mu_{N_j}(\varDelta e), j = 1,2,3,4,5 \qquad (4.5.2.5)$$

L_i^1 and L_j^1 are the MFs of M_i and N_j respectively. L_i^1 specifies the degree to which the given e satisfies the quantifier M_i and L_j^1 specifies the degree to which the given $\varDelta e$ satisfies the quantifier N_j.

Layer 2: In this layer, each node output represents the firing strength of each rule, one can obtain that:

$$L_t^2 = w_t = \mu_{M_i}(e) \times \mu_{N_j}(\varDelta e), t = i \times j = 1,2,3 \ldots \ldots,35 \qquad (4.5.2.6)$$

Layer 3: Each node in this layer is to normalize the firing strength.

$$\overline{w}_t = \frac{w_t}{\sum w_t} \ for \ t = 1,2, \ldots \ldots,35 \qquad (4.5.2.7)$$

Layer 4: Obtain the output for each node.

$$L_t^4 = \overline{w}_t \times f_t = \overline{w}_t \times (p_t \times e + q_t \times \varDelta e + s_t), for \ t = 1,2 \ldots,35 \qquad (4.5.2.8)$$

Where $\{p_t, q_t, s_t\}$ is the consequent parameter set and L_t^4 represents the output for each node.

Layer 5: Calculate the final output.

$$L_t^5 = w = \sum_{t=1}^{35} \overline{w}_t \times f_t = \frac{\sum_{t=1}^{35} \overline{w}_t \times f_t}{\sum_{t=1}^{35} \overline{w}_t} = \sum_{t=1}^{35} \overline{w}_t \times (p_t \times e + q_t \times \Delta e + s_t) \qquad (4.5.2.9)$$

Now, we need to optimize both premise parameters and consequent parameters. As stated in Jang's paper, the hybrid approach, composed of a forward pass and a backward pass, is much faster than the strict gradient descent approach, therefore, we adopt the hybrid approach for parameter tuning.

In the feedforward pass, the consequent parameters are identified based on the least square estimation (LSE) technique when the premise parameters are fixed. Eq. (4.5.2.9) reveals that the overall output can be expressed as a linear combination of the consequent parameters when the values of the premise parameters are given. Therefore, we can re-write Eq. (4.5.2.9) as:

$$L_t^5 = (\overline{w}_1 \times e) \times p_1 + (\overline{w}_1 \times \Delta e) \times q_1 + \overline{w}_1 \times s_1 + \cdots + (\overline{w}_{35} \times e) \times p_{35} + (\overline{w}_{35} \times \Delta e) \times q_{35} + \overline{w}_{35} \times s_{35} \qquad (4.5.2.10)$$

Define two vectors as:

$$\begin{cases} \theta = [p_1, \cdots, p_{35}, q_1, \cdots, q_{35}, s_1, \cdots s_{35}]^T, \text{paramter vector} \\ \varphi = [\overline{w}_1 \times e, \cdots, \overline{w}_{35} \times e, \overline{w}_1 \times \Delta e, \cdots, \overline{w}_{35} \times \Delta e, \overline{w}_1, \cdots, \overline{w}_{35}]^T, \text{information vector} \end{cases} \qquad (4.5.2.11)$$

Then Eq. (4.5.2.10) can be expressed as:

$$L_t^5 = \varphi^T \theta \qquad (4.5.2.12)$$

Then the LSE technique can be applied to obtain the optimal consequent parameter set[33].

In the backward pass, the error rates propagate backward, and the premise parameters are updated by the gradient descent technique.

The cost function is:

$$E = \frac{1}{2}(L_t^5 - \Delta w_{desired})^2 \qquad (4.5.2.13)$$

where, L_t^5 and $\Delta w_{desired}$ refer to obtained results from Eq. (4.5.2.10) and desired values respectively.

Gradients for c_i, δ_i c_j, and δ_j are:

---

[33] Besides, we can also apply the least mean square (LMS) algorithm to obtain the optimal values.

$$\frac{\Delta E}{\Delta c_i} = \frac{\Delta E}{\Delta L_t^5} \times \frac{\Delta L_t^5}{\Delta L_t^4} \times \frac{\Delta L_t^4}{\Delta L_t^2} \times \frac{\Delta L_t^2}{\Delta c_i}$$

$$= (L_t^5 - w_{desired}) \times \frac{1}{\sum_{t=1}^{35} \overline{w}_t} \times f_t \times \exp\left(-\left(\frac{e - c_i}{2\delta_i}\right)\right) \qquad (4.5.2.14)$$

$$\times \exp\left(-\left(\frac{\Delta e - c_j}{2\delta_j}\right)\right) \times \frac{1}{2\delta_i}$$

$$\frac{\Delta E}{\Delta \delta_i} = \frac{\Delta E}{\Delta L_t^5} \times \frac{\Delta L_t^5}{\Delta L_t^4} \times \frac{\Delta L_t^4}{\Delta L_t^2} \times \frac{\Delta L_t^2}{\Delta \delta_i}$$

$$= (L_t^5 - w_{desired}) \times \frac{1}{\sum_{t=1}^{35} \overline{w}_t} \times f_t \times \exp\left(-\left(\frac{e - c_i}{2\delta_i}\right)\right) \qquad (4.5.2.15)$$

$$\times \exp\left(-\left(\frac{\Delta e - c_j}{2\delta_j}\right)\right) \times \frac{e - c_i}{2\delta_i{}^2}$$

$$\frac{\Delta E}{\Delta c_j} = \frac{\Delta E}{\Delta L_t^5} \times \frac{\Delta L_t^5}{\Delta L_t^4} \times \frac{\Delta L_t^4}{\Delta L_t^2} \times \frac{\Delta L_t^2}{\Delta c_j}$$

$$= (L_t^5 - w_{desired}) \times \frac{1}{\sum_{t=1}^{35} \overline{w}_t} \times f_t \times \exp\left(-\left(\frac{e - c_i}{2\delta_i}\right)\right) \qquad (4.5.2.16)$$

$$\times \exp\left(-\left(\frac{\Delta e - c_j}{2\delta_j}\right)\right) \times \frac{1}{2\delta_j}$$

$$\frac{\Delta E}{\Delta \delta_j} = \frac{\Delta E}{\Delta L_t^5} \times \frac{\Delta L_t^5}{\Delta L_t^4} \times \frac{\Delta L_t^4}{\Delta L_t^2} \times \frac{\Delta L_t^2}{\Delta \delta_j}$$

$$= (L_t^5 - w_{desired}) \times \frac{1}{\sum_{t=1}^{35} \overline{w}_t} \times f_t \times \exp\left(-\left(\frac{e - c_i}{2\delta_i}\right)\right) \qquad (4.5.2.17)$$

$$\times \exp\left(-\left(\frac{\Delta e - c_j}{2\delta_j}\right)\right) \times \frac{e - c_j}{2\delta_j{}^2}$$

Updating equations of c_i, δ_i c_j and δ_j are:

$$c_i(t + 1) = c_i(t) + \eta \frac{\Delta E}{\Delta c_i} \qquad (4.5.2.18)$$

$$\delta_i(t + 1) = \delta_i(t) + \eta \frac{\Delta E}{\Delta \delta_i} \qquad (4.5.2.19)$$

$$c_j(t+1) = c_j(t) + \eta \frac{\Delta E}{\Delta c_j} \tag{4.5.2.20}$$

$$\delta_j(t+1) = \delta_j(t) + \eta \frac{\Delta E}{\Delta \delta_j} \tag{4.5.2.21}$$

where, η represents the learning rate.

According to Jang (1993), the relationship between the learning rate η and the step size μ is as follows:

$$\eta = \frac{\mu}{\sqrt{\sum \beta (\frac{\alpha E}{\alpha \beta})^2}} \tag{4.5.2.22}$$

where, E represents the statistical expectation operator and β denotes any parameter needed to be tuned. Here, the choice of the step size is related to the speed of convergence.

4.5.3. Proportional-derivative (PD)-like fuzzy logic control (FLC) technique

The proportional-integral-derivative (PID) controller is a mature technique and plays an important role in the industry. The subject of the PID controller is the error signal, which denotes the difference between the actual output and the desired output (set point). The PID controller has three parts, the proportional part k_p, the integral part k_i and the derivative part k_d, it follows that:

$$u(t) = k_p e(t) + k_i \int_0^t e(\tau)d\tau + k_d \frac{de(t)}{dt} \tag{4.5.3.1}$$

According to Eq. (4.5.3.1), the form of a conventional PD controller, in discrete form, is:

$$u(k) = k_p e(k) + k_d \Delta e(k) \tag{4.5.3.2}$$

k_p and k_d are proportional and derivative gains, respectively.

The $e(k)$ and $\Delta e(k)$ are defined as:

$$\begin{cases} e(k) = r - y(k) \\ \Delta e(k) = e(k) - e(k-1) \end{cases} \tag{4.5.3.3}$$

Where r means the desired value and k means the sampling time.

The FLC technique employing fuzzy if-then rule can model the qualitative aspects of human knowledge and reasoning processes without employing precise quantitative analyses. In comparison with conventional mathematical modelling, the FLC technique is good at dealing with ill-defined and uncertain systems. An FLC consist of four parts, fuzzification, knowledge base, decision-making unit, and defuzzification. Depending on the

63

types of fuzzy reasoning and fuzzy if-then rules employed, the FLC can be classified into three types, Mamdani, TSK, and Tsukamoto types (Tokhi and Azad, 2017).

The PD-like FLC technique is to construct the fuzzy rule based on the form of the PD controller, a bridge to build up connections between the error signal and the control signal. In this paper[34], we use the TSK-type fuzzy models and the reason has already provided above. The change in filter coefficients is used as the control signal $u(k)$ and the conventional PD controller is used to connect it with the residual noise signal $e(k)$ and the change of the residual noise signal $\Delta e(k)$, which is given as:

$$if\ (\ e(k)\ is\ M_i)\ and\ (\Delta e(k)\ is\ N_j), then\ (u(k) = f(e(k), \Delta e(k))) \tag{4.5.3.4}$$

Where M_i, and N_j are all linguistic variables (see Table 4.5.2.1 and Table 4.5.2.2).

4.5.4. Inertial particle swarm optimization (PSO) technique

The PSO algorithm, firstly proposed by Eberhart and Kennedy in 1995, is a stochastic optimization technique based on swarm and it belongs to the field of swarm intelligence (SI). It simulates animals' social behaviours, including insects, herds, birds, and fishes (Wang et al., 2018). These swarms find food in a cooperative way, and everyone in the swarms keeps changing the search pattern based on the learning experiences of its own and other members (Zhang et al., 2015; Wang et al., 2018). The main idea of the PSO algorithm contains two parts, the first part is the evolutionary algorithm that the PSO uses a swarm mode which makes it to simultaneously search large region in the solution space of the optimized objective function and the second part is artificial life that it studies the artificial systems with life characteristics (Wang et al., 2018).

To apply the inertial PSO algorithm, we re-express the coefficient as:

$$w = \begin{bmatrix} w_1^1\ w_1^2\ ...\ w_1^Q \\ w_2^1\ w_2^2\ ...\ w_2^Q \\ ...\ ...\ ...\ ... \\ w_S^1\ w_S^2\ ...\ w_S^Q \end{bmatrix} \tag{4.5.4.1}$$

Where the coefficient vector is an $S \times Q$ matrix. The symbol S represents the size of the dimensional search space and the symbol Q denotes the number of particles in the dimensional search space. Each column of the matrix represents the coefficient value of an adaptive filter in the filter bank and the relationship between the S and Q in this case is:

---

[34] In Simulink, the 'Discrete Derivative' block is used for computing discrete-time derivative.

$$Q = S + 1 \qquad (4.5.4.2)$$

In comparison with the original PSO algorithm, the inertial PSO algorithm introduces a new parameter, named as the inertia weight parameter ψ, to strike a better balance between global exploration and local exploitation. ψ is designed to adjust the influence of the previous particle velocities on the optimization process. The main steps of the inertial particle swarm optimization (PSO) algorithm can be explored below.

Firstly, initialize the swarm by randomly assigning velocity and position to each particle in the search space. Secondly, the velocity and position of each particle are adjusted according to the information from its previous experience and neighbours in each iteration. Assume v_n^d and p_n^d denote the velocity and position of the nth particle in d^{th} dimension. Thirdly, the velocity and position of each particle are updated as:

$$v_n^d = \psi * v_n^d + c1 * r_1^d * (PB_n^d - p_n^d) + c2 * r_2^d * (GB^d - p_n^d), n = 1,2,3,\cdots,N; d$$
$$= 1,2,3,\cdots D \qquad (4.5.4.3)$$

$$p_n^d = p_n^d + v_n^d, \qquad j = 1,2,3,\cdots,J; q = 1,2,3,\cdots Q \qquad (4.5.4.4)$$

Where, ψ represents the inertia weight and r_1^d, r_2^d are two random numbers. In this paper, it is assumed that ψ is 0.6 (Shi and Eberhart, 1998). PB_n^d represents the best previous position of the nth particle in d^{th} dimension and its position is determined by the best fitness value Jp_n^d calculated from fitness function. Here, the mean square error is used as the cost function. The smallest value of Jp_n^d is recorded as Jg^d and the corresponding best-so-far position is recorded as GB^d. The velocity and position of each particle cannot exceed the maximum value.

4.6. Case studies

This section contains several case studies, illustrates the principle of ANC systems, explore the effects of Δh_{34} and $\Delta\theta(\Omega)$ on K, demonstrates the cancellation capability of the proposed geometrical configuration-based adaptive feedforward ANC system, and explores the effects of different geometrical configurations on the cancellation performance. For all simulations, the sampling frequency is 2000 Hz (Chang and Shyu, 2003; Zhang and Gan, 2004) and the simulation time is 1 second.

The sound transfer time is calculated as:

$$d = \frac{Physical\ distance}{sound\ velocity} \times sampling\ frequency \qquad (4.6.1)$$

Where d is presented as the parameter for the pure time delay block in MATLAB SIMULATION.

The nonlinearities are assumed deriving from the microphone and the loudspeaker, modelled by the second-order Butterworth high-pass filter with a cut-off frequency[35] of 80 *Hz* (Janocha and Liu, 1998).

4.6.1 Illustrate the superposition principle of the ANC system

As stated in section 2.3, the ANC system is constructed based on the principle of superposition, therefore, this case study aims to illustrate this principle.

Assume the primary acoustic wave signal is a sine 100 *Hz* signal with amplitude 1.
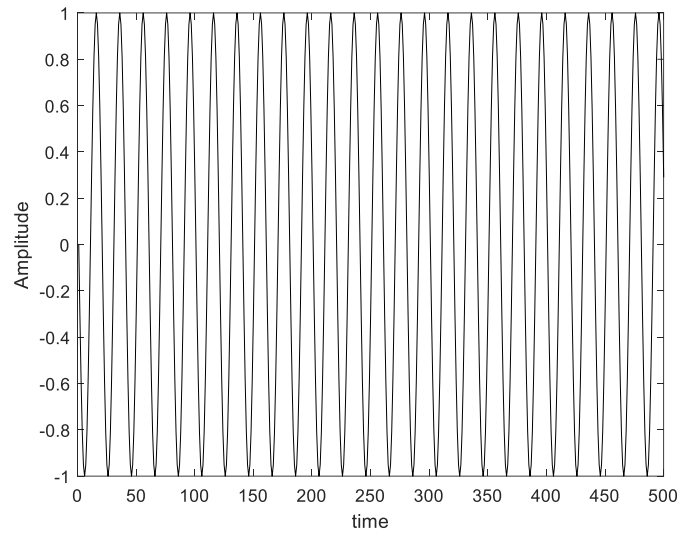
Figure 4.6.1.1 presents the time history of the primary acoustic wave signal, the secondary acoustic wave signal, and the residual noise signal.
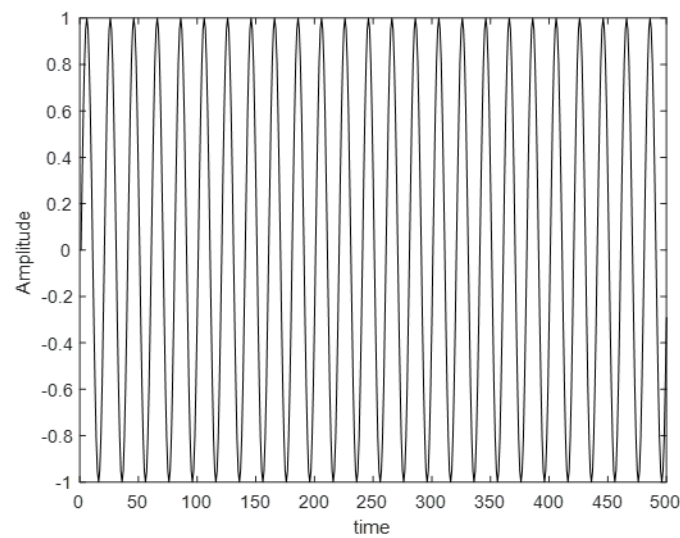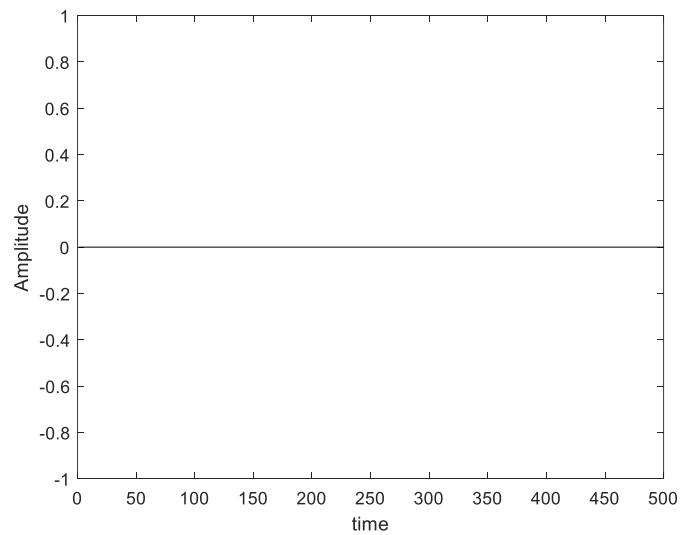

(a)

---

[35] In the system frequency response, the cut-off frequency/corner frequency/break frequency is a boundary at which energy flowing through the system begins to be reduced (attenuated or reflected) rather than passing through.

(b)

(c)

Figure 4.6.1.1. The time history of each signal ((a). primary acoustic wave signal; (b). secondary acoustic wave

signal; (c). residual error noise signal)

The *x*-axis represents the time and the *y*-axis represents the amplitude. To make the simulation results

clearly, we narrow the time domain from 0 to 500.

Figure 4.6.1.1a reflects the primary acoustic wave signal and Figure 4.6.1.1b reflects the secondary

acoustic wave signal. Combine Figure 4.6.1.1a and Figure 4.6.1.1b, we can find that the secondary acoustic wave

signal has the same amplitude but an opposite phase in comparison with the primary acoustic wave signal.

Figure 4.6.1.1c reflects the residual noise signal, which is the result of the destructive interference and we can find that the primary acoustic wave signal is completed cancelled.

### 4.6.2. Investigate the effects of Δh_{34} and $\Delta\theta(\Omega)$ on K

As mentioned in section 2.3, Δh_{34} and $\Delta\theta(\Omega)$ are two main factors affecting the K. Therefore, the object of this case study is to investigate the effects of these two factors on the K.

Remark 9: The K is an indicator of the cancellation performance, which can be directly reflected in the presence of the residual noise signal magnitude (measured in dB).

Firstly, we keep $\Delta\theta(\Omega) = \pi$ and explore the effects of different Δh_{ps} on the K.

The sine 100 Hz signal with amplitude 1 is used as the primary acoustic wave signal and the secondary acoustic wave signal with the same amplitude but opposite phase ($\Delta\theta(\Omega) = \pi$). The values of both h_3 and h_4 are multiple of 3.4 because the sound velocity in air is 340 $^m/_s$ and we want to simplify the calculation process.

Figure 4.6.2.1 qualitatively presents the cancellation performance in the presence of the residual noise signal magnitude (measured in dB) under different Δh_{34} and Table 4.6.2.1 quantitatively provides the value of the residual noise signal magnitude (measured in dB).
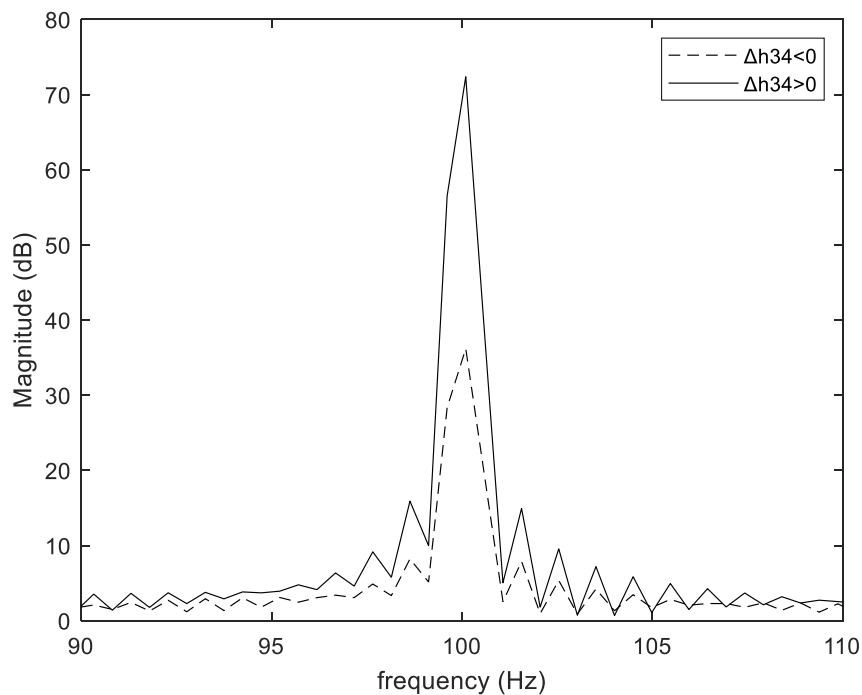
Figure 4.6.2.1. Cancellation performance under different Δh_{34}[36]

---

[36] Here Δh34 means Δh_{34}

Table 4.6.2.1. The residual noise signal magnitude

$\Delta h_{34} > 0$	$\Delta h_{34} < 0$
72.37 dB	36.19 dB

Remark 10: Under this condition, we assume the value of $\omega \frac{\Delta h_{34}}{c}$ is between zero and π, which is convenient for further results analysis.

The simulation results from Figure 4.6.2.1 and Table 4.6.2.1 reveal that the residual noise signal magnitude is lower when $\Delta h_{34} < 0$, which implies a bigger K.

Consider Eq. (2.3.2.5) and the opposite phase condition, we can obtain the expression of K as:

$$K = -\frac{GSR(\Omega)}{GPR(\Omega)} + \sqrt{\frac{GSR(\Omega)}{GPR(\Omega)}} \cos{(\Omega \frac{\Delta h_{34}}{c})} \qquad (4.6.2.1)$$

Consider the monotonic property of the cosine function between zero and π, we can obtain that a smaller Δh_{34} corresponding to a bigger K, which corresponds to a lower residual noise signal magnitude.

Secondly, we explore the effects of different $\Delta\theta(\Omega)$ on the K when Δh_{34} is constant.

In Matlab Simulink, the phase shift is achieved through the time delay and the relationship between the phase shift and the time delay is expressed as:

$$\Phi = 360^0 \times f \times \Delta t \qquad (4.6.2.2)$$

Where f is the system frequency, Δt is the time delay, and Φ is the phase difference in degrees.

Like Figure 4.6.2.1 and Table 4.6.2.1, we present the simulation results under different $\Delta\theta(\Omega)$ in Figure 4.6.2.2 and Table 4.6.2.2 respectively.
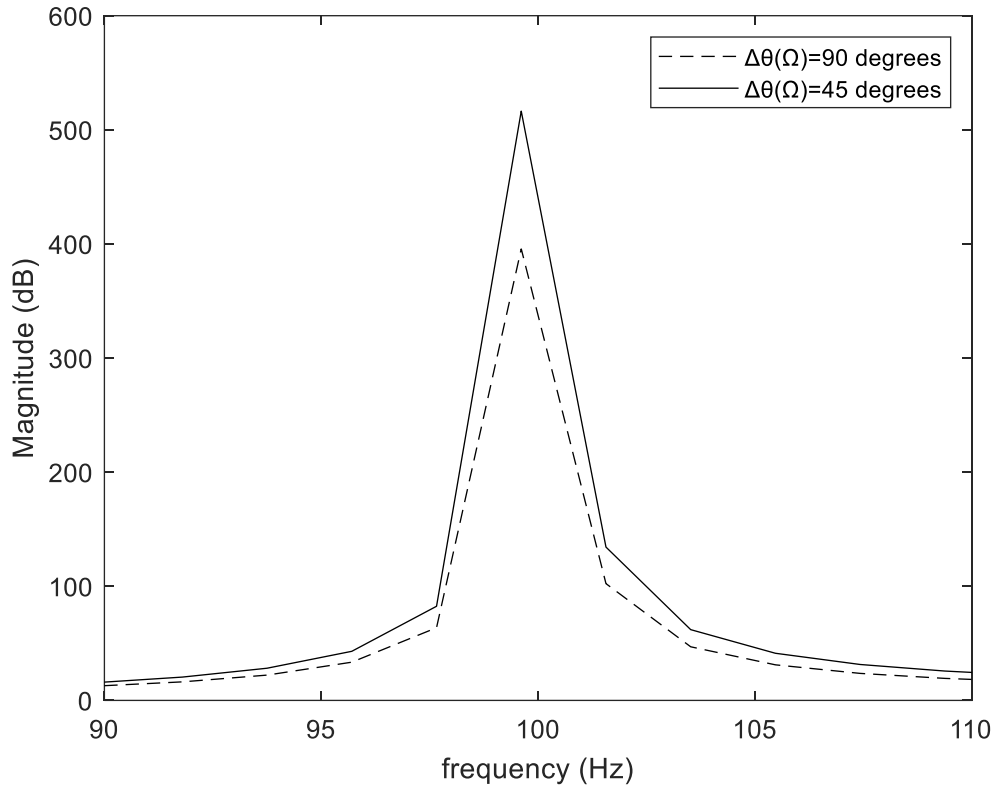
Figure 4.6.2.2. Cancellation performance under different $\Delta\theta(\Omega)$

Table 4.6.2.2. The magnitude of the residual noise signal

| $\Delta\theta(\Omega) = 90\ degrees$	$\Delta\theta(\Omega) = 45\ degrees$
395.73 dB	516.36 dB

The simulation results from Figure 4.6.2.2 and Table 4.6.2.2 reveal that the residual noise signal magnitude is smaller when $\Delta\theta(\Omega)$ is bigger, which implies a bigger K. From the perspective of physical phenomenon, the residual noise signal is the superposition of the primary acoustic wave signal and the secondary acoustic wave signal. Within the reasonable physical constraints range, the increment of $\Delta\theta(\Omega)$ implies that the amplitude of the secondary acoustic wave signal is increasing in the anti-direction and the residual noise signal magnitude is decreasing, which corresponds the K is increasing.

4.6.3. Compare the time-consuming and the cancellation performance with and without identification

This case is to demonstrate that reduced simulation time and better cancellation performance can be achieved when the adaptive filter is identified before the beginning of the adaptive control.

Here, we use the FIR filter as an example because of its simple structure.

Firstly, we choose a sine 100 Hz wave signal as the representative of the narrowband noise and comparison results are presented qualitatively and quantitatively in Figure 4.6.3.1 and Table 4.6.3.1 separately.
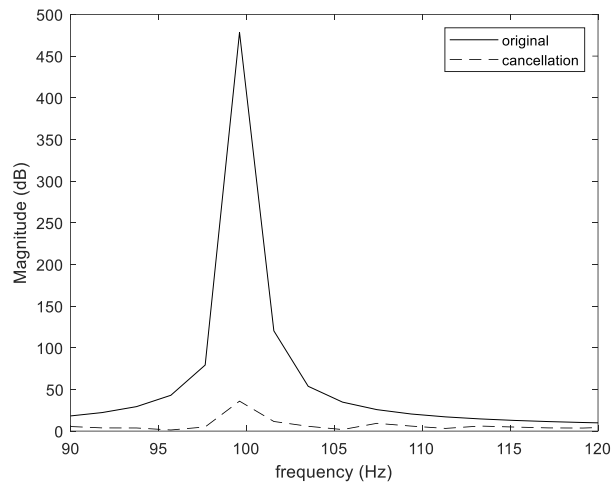
(a). without identification
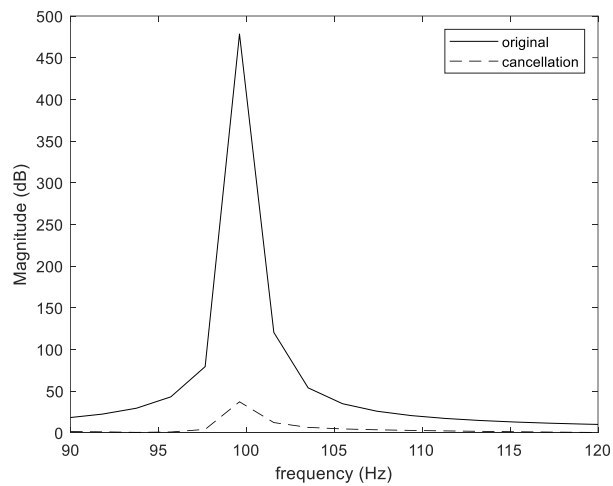
(b). with identification

Figure 4.6.3.1. Simulation results

Table 4.6.3.1. Comparison results of simulation time (in seconds)

Name	Simulation time (seconds)
Without identification	223.09
With identification	173.56

Secondly, we choose the Gaussian white noise with zero mean and unit variance as the primary acoustic wave and repeat the same procedures mentioned above. The comparison results are presented qualitatively and quantitatively in Figure 4.6.3.2 and Table 4.6.3.2 separately.
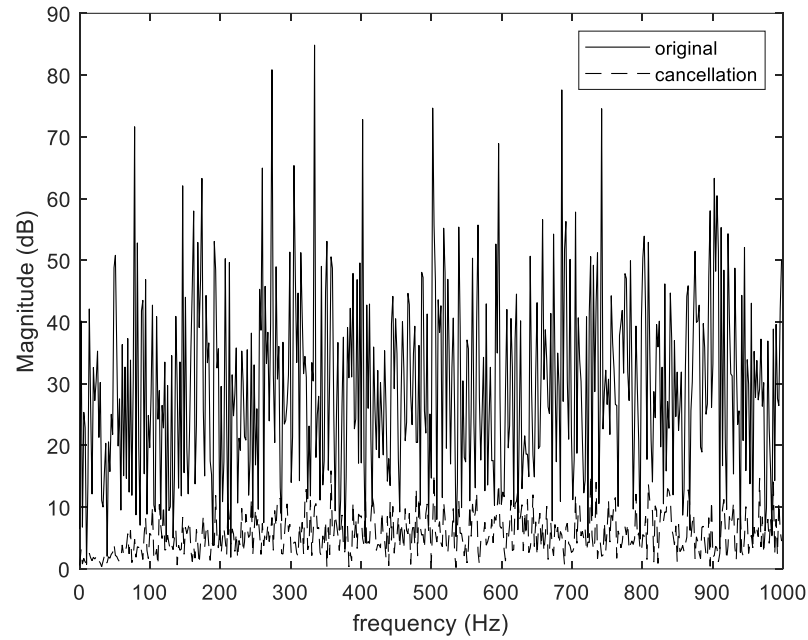

(a). without identification

(b). with identification

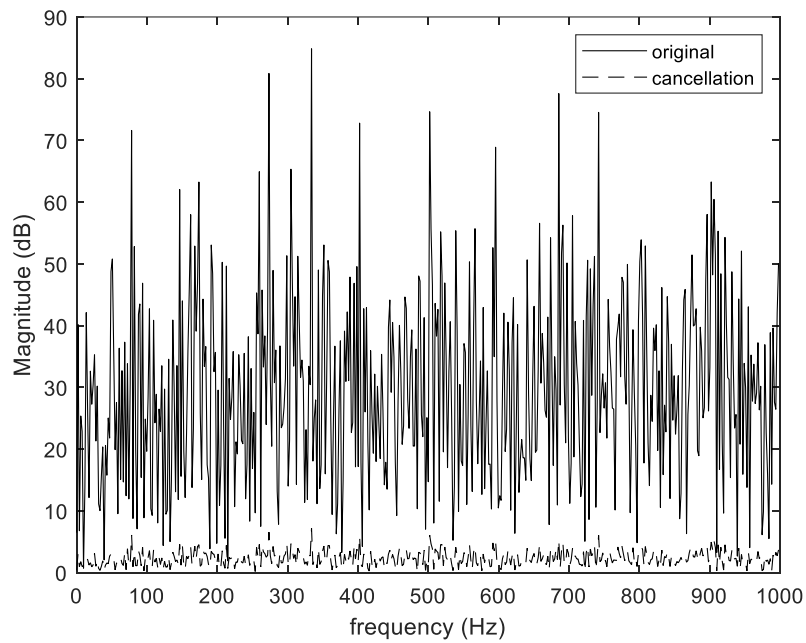**Figure 4.6.3.2.** Simulation results

72

Table 4.6.3.2. Comparison results of simulation time (in seconds) and average amount of cancellation (in dB)

Name	Simulation time (seconds)	Average amount of cancellation (dB)
Without identification	219.5	23.94
With identification	189.5	27.19

For the narrowband noise, results from Figure 4.6.3.1 and Table 4.6.3.1 reflect that there is a significant reduction of simulation time (measured in seconds) when the coefficients of the FIR filter are identified first but the difference in the presence of the residual noise signal magnitude (measured in dB) can be neglected. For the broadband noise, results from Figure 4.6.3.2 and Table 4.6.3.2 indicate that both simulation time and cancellation performance in the presence of average amount of cancellation (measured in dB) have been improved a lot when the coefficients of the FIR filter have been identified first.

In summary, we can reduce the simulation time or improve the cancellation performance when the coefficients of the FIR filter have been identified first. Therefore, in the following case studies, all adaptive filters are identified first, and we will no longer repeat this procedure.

4.6.4. The employment of the ANFIS technique

This case aims to demonstrate the cancellation capability of the proposed ANC system when employing the ANFIS technique as the parameter adjustment mechanism. Besides, we aim to explore the effects of different geometrical constraints on the cancellation performance in the presence of average amount of cancellation (measured in dB) for the broadband noise. The order of the adaptive FIR filter is 9.

Remark 11: The reason for choosing the broadband noise as the object to investigate the effects of different geometrical constraints on the cancellation performance is that the broadband noise is complex and the difference is significant.

Firstly, we select three different kinds of narrowband noise as the primary acoustic wave and Figure 4.6.4.1 qualitatively presents the cancellation performance in the presence of the residual noise signal magnitude (measured in dB).
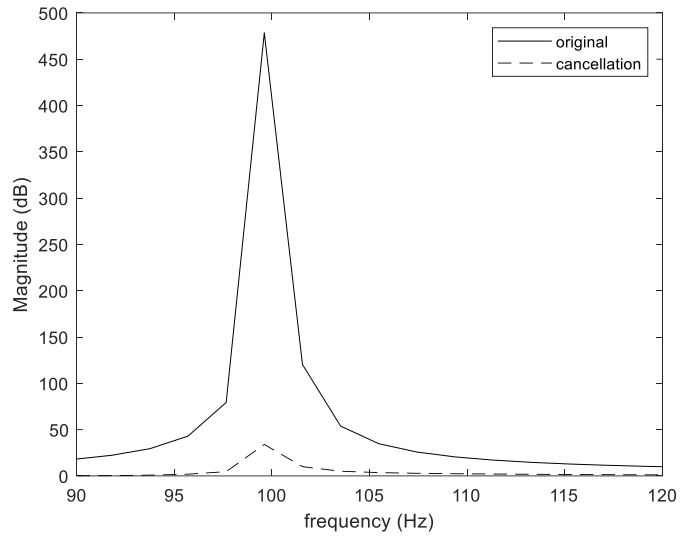
(a) a sine 100 *Hz* signal
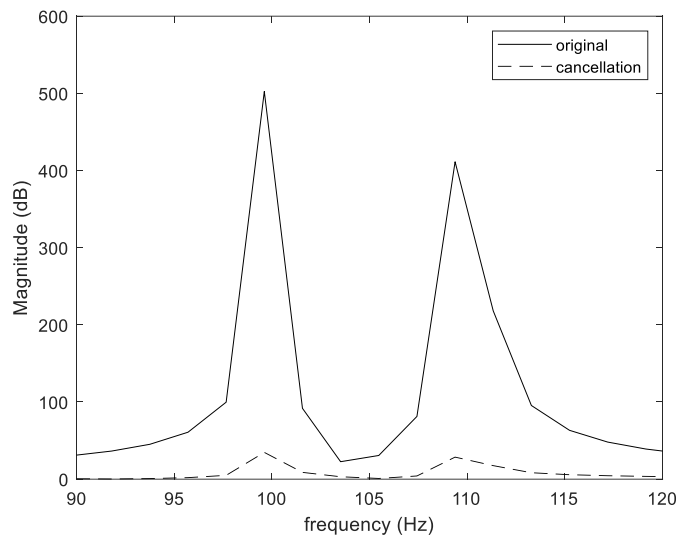
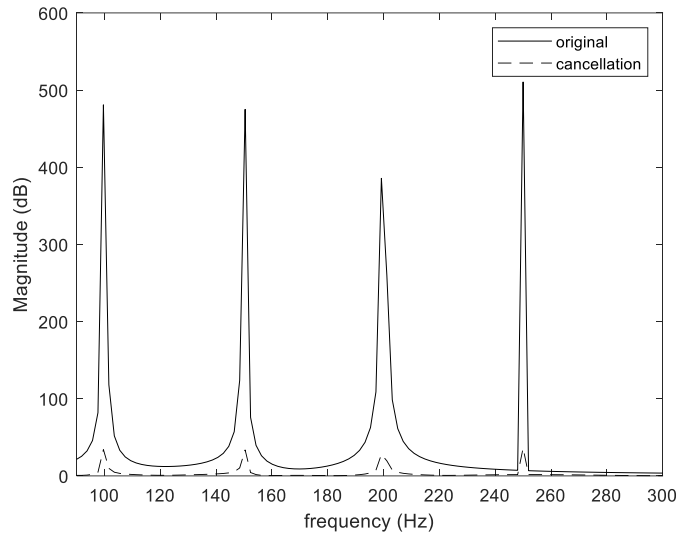(b) a combined signal (a sine 100 *Hz* signal + a sine 110 *Hz* signal)

(c) a combine signal consisted with four frequency content, 100 *Hz*, 150 *Hz*, 200 *Hz*, and 250 *Hz*.

Figure 4.6.4.1. Cancellation performance for narrowband noise

Secondly, we use the Gaussian white noise with zero mean and unit variance, the widely used broadband noise, as the primary acoustic wave.

Figure 4.6.4.2 qualitatively presents the cancellation performance in the presence of the average amount of cancellation (measured in dB).
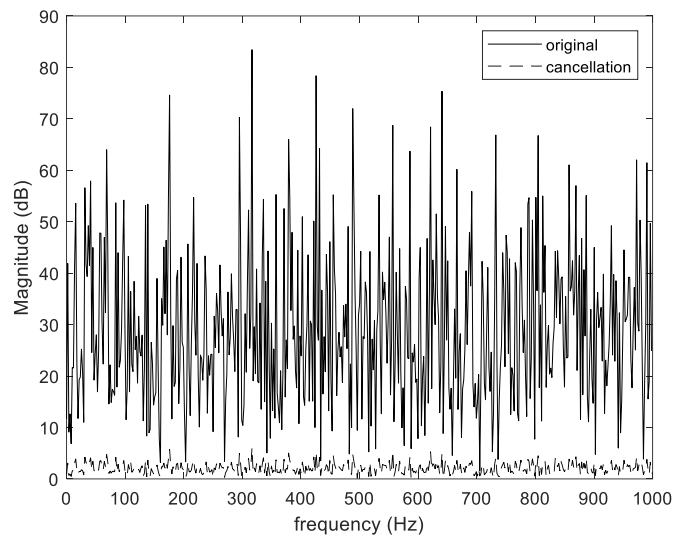
Figure 4.6.4.2. Cancellation performance for broadband noise

Simulation results from Figure 4.6.4.1 and Figure 4.6.4.2 demonstrate the cancellation capability of the proposed ANC system for the narrowband noise and the broadband noise when employing the ANFIS technique as the parameter adjustment mechanism.

75

Now, we aim at exploring the effects of different geometrical configurations on the cancellation performance and the related results are presented in Figure 4.6.4.3 and Table 4.6.4.1 separately.
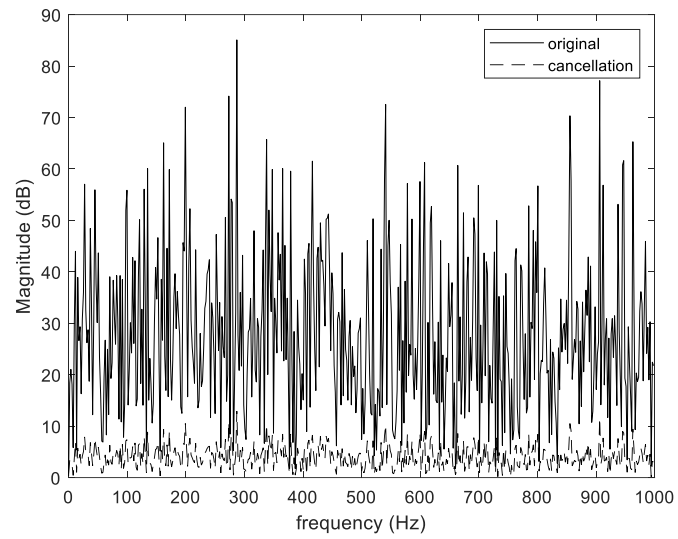
(a) $2 > a > 1 > b > \frac{1}{2}$
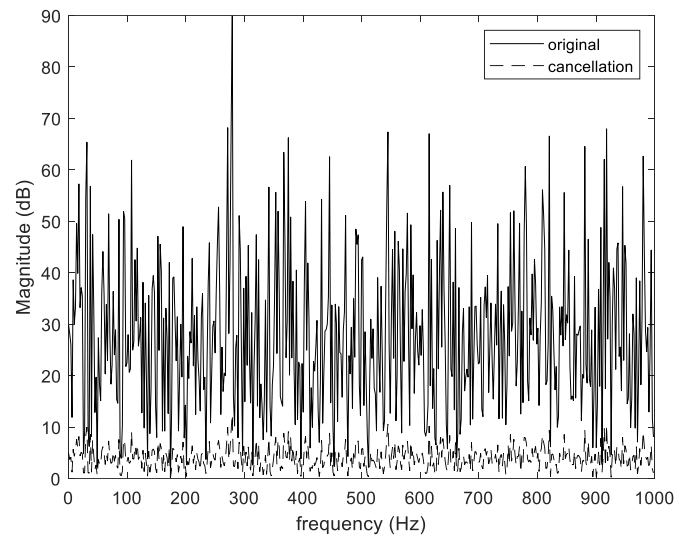
(b) $2 > a > b > 1$
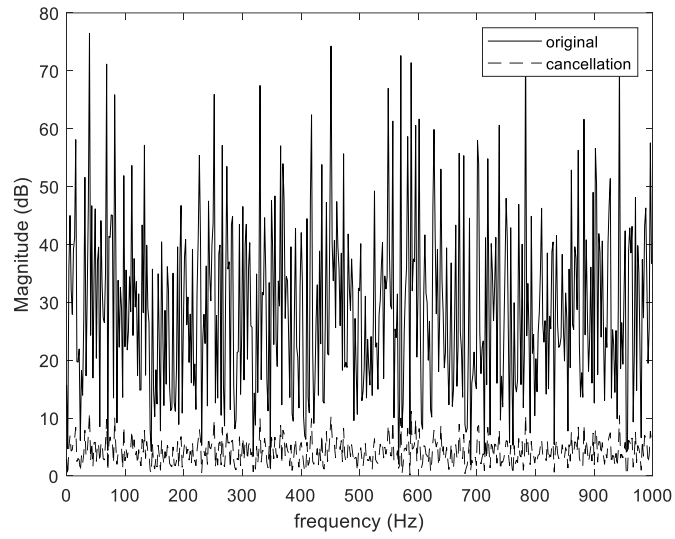
(c) $2 > a = b > 1$
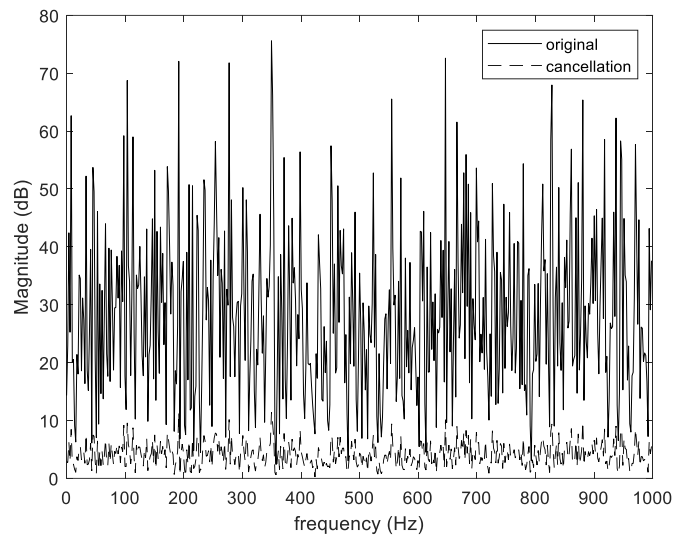
(d) $2 > b > a > 1$

Figure 4.6.4.3. Cancellation performance

Table 4.6.4.1. Comparison results

Configuration	Average amount of cancellation (dB)	Amount of running time (seconds)
$2 > a > 1 > b > \dfrac{1}{2}$	23.66	323.73
$2 > a > b > 1$	23.69	275.55
$2 > a = b > 1$	24.65	268.64
$2 > b > a > 1$	24.19	290.26

77

Simulation results from Figure 4.6.4.3 and Table 4.6.4.1 reflect that the effects of different geometrical configurations on the cancellation performance in the presence of average amount of cancellation (measured in dB) and the running time (measured in seconds) are existing. With the increasing of b, the cancellation performance has a slightly improved, and the optimal geometrical configuration is $2 > a = b > 1$. Meanwhile, the amount of running time is decreasing significantly especially when b changing from $1 > b$ to $b > 1$ and the best running time is when $2 > a = b > 1$.

From a physical perspective, the value of b determines the length of the acoustic feedback path[37]. As mentioned above, the acoustic feedback signal is a kind of disturbance during the process of noise cancellation. Therefore, within the reasonable physical constraints range, a shorter acoustic feedback path will contribute to improving the cancellation performance.

4.6.5. The employment of the proportional-derivative (PD)-like fuzzy logic control (FLC) technique

In this case study, we keep the FIR filter as the digital filter and its order is 9. The PD-like FLC technique is employed as the parameter adjustment mechanism and the main aim of this case study is to explore the effects of different geometrical configurations on the cancellation performance. The linguistic values of *e, Δe,* and *Δw* can be found in Table 4.5.1, Table 4.5.2, and Table 4.5.3.

Based on Eq. (4.5.30) and Eq. (4.5.32), we find that the selection of k_p and k_d might affect the cancellation performance, therefore, we firstly explore the effects of k_p and k_d on the degree of cancellation.

The Gaussian white noise with the zero mean and unit variance is used as the primary acoustic wave. Figure 4.6.5.1 qualitatively presents the cancellation performance in the presence of the average amount of cancellation (measured in dB) under four different pairs of k_p and k_d.

---

[37] In the ANC system, the acoustic feedback path denotes h_2.
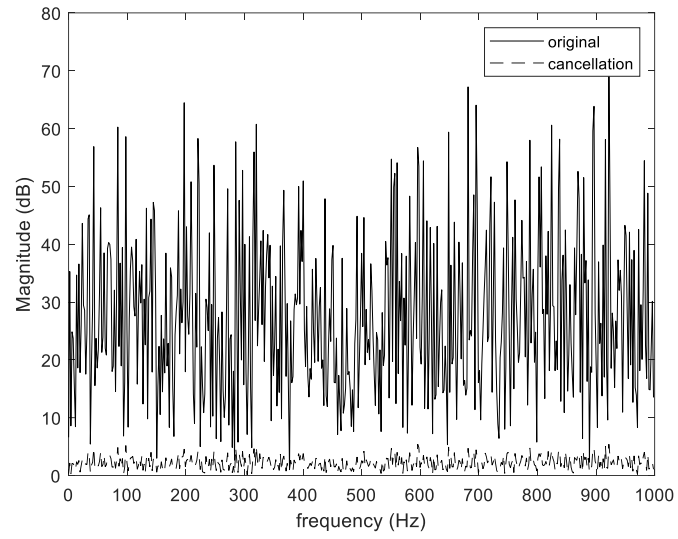
(a) $k_p = k_d = 1$
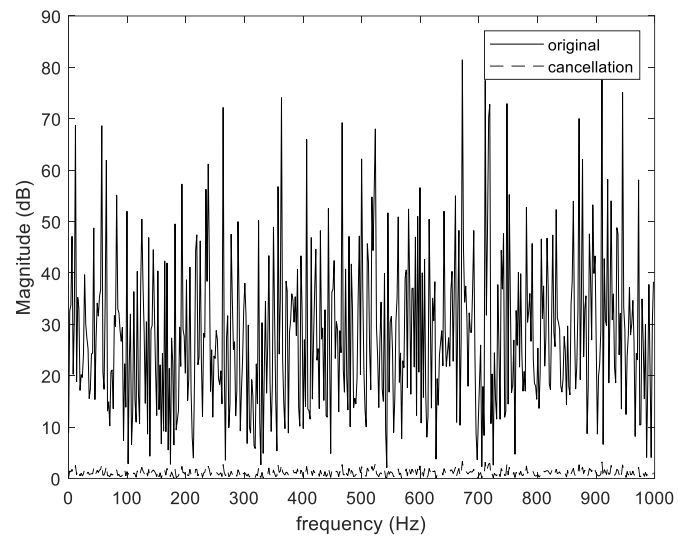
(b) $k_p = 0.5, k_d = 1$
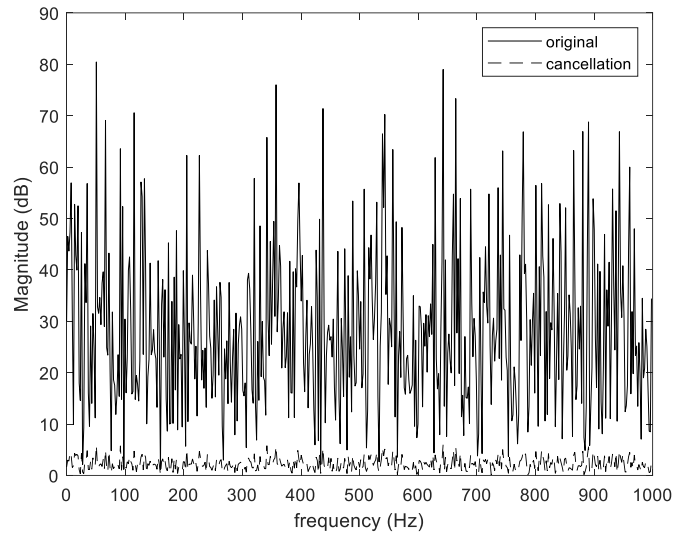
(c) $k_p = 1, k_d = 0.5$
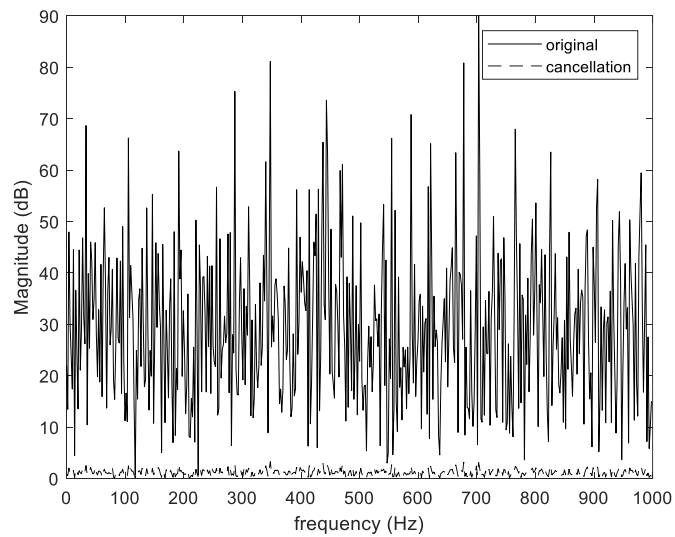
(d) $k_p = 0.5, k_d = 0.5$

Figure 4.6.5.1. Cancellation performance

Remark 12: According to statements provided in the Tokhi and Azad's book, the selections of k_p and k_d are based on the unit step response of the PD controller. In practice, we need to make sure the performance of the PD-type FLC is very promising in respect of rise time, maximum overshoot, settling time, and the steady-state error. In this case study, we randomly choose four pairs of parameters to briefly illustrate the effects of each parameter on the cancellation performance, which provides general instructions on future physical experiments.

Table 4.6.5.1 presents the comparison results.

Table 4.6.5.1. Comparison results

k_p	k_d	Average amount of cancellation (dB)	Amount of running time (seconds)
1	1	28.04	216.67
0.5	1	26.9	223.11
1	0.5	26.04	256.57
0.5	0.5	27.76	299.94

According to the comparison results from Table 4.6.5.1, it appears that a higher average amount of cancellation (measured in dB) and a lower amount of running time (measured in seconds) can be achieved when $k_p = 1$ and $k_d = 1$. In the PID control theory, increasing the proportional gain k_p can reduce the steady-state error and increasing the derivative gain k_d will cause the control system to react more strongly to changes in the error term, which increases the speed of the overall control system response.

Secondly, we aim to explore the effect of different geometrical configurations when $k_p = 1$ and $k_d = 1$. We still choose the Gaussian white noise with zero mean and unit variance as the primary acoustic wave. To analyse conveniently, we prefer to make the value of the physical distance is times of constant 1.7 or 3.4.

Remark 13: The physical distance denotes h_1, h_2, h_3, and h_4.

Figure 4.6.5.2 qualitatively presents cancellation performance in the presence of the average amount of cancellation (measured in dB).
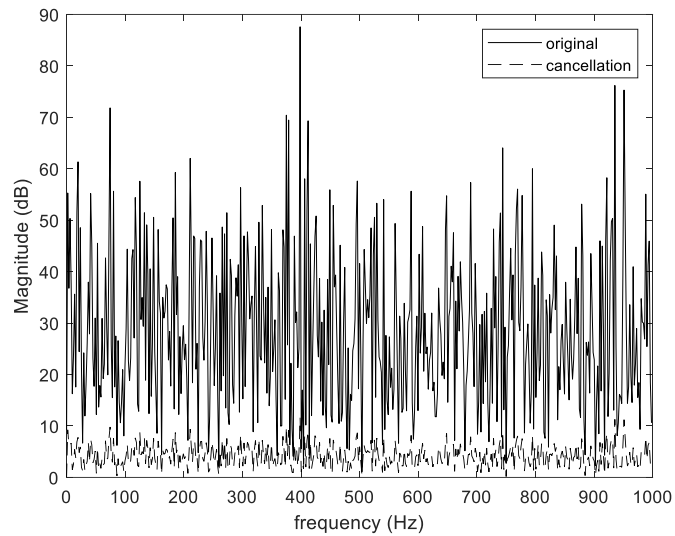
(a) $2 > a > 1 > b > \frac{1}{2}$
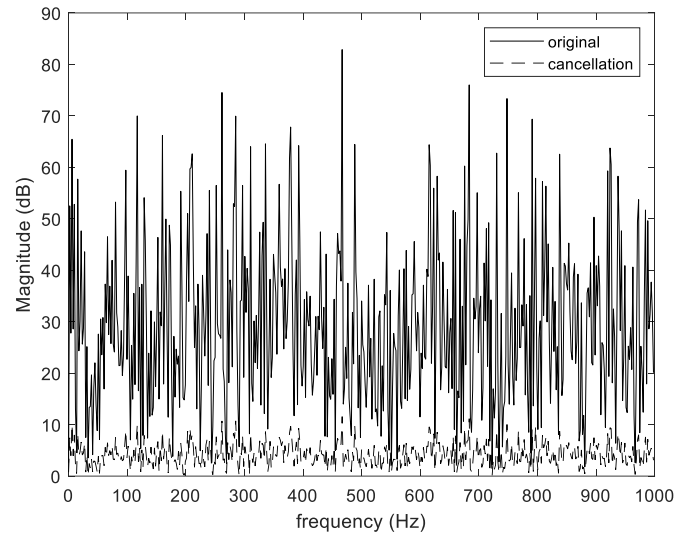
(b) $2 > a > b > 1$
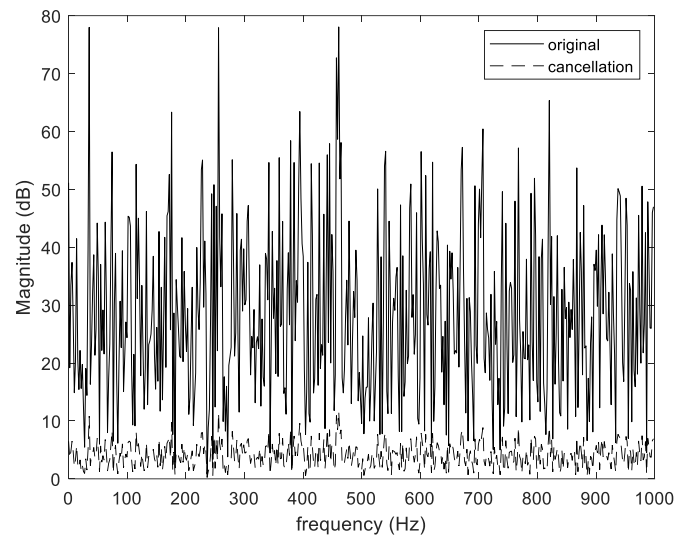
(c) $2 > a = b > 1$
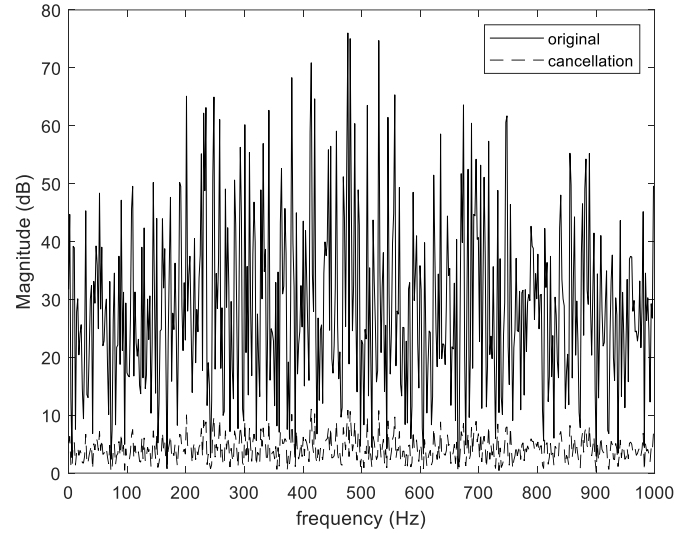
(d) $2 > b > a > 1$

Figure 4.6.5.2. Cancellation performance

Table 4.6.5.2 provides the comparison results under different geometrical configurations.

Table 4.6.5.2. Comparison results

Configuration	Average amount of cancellation (dB)	Amount of running time (seconds)
$2 > a > 1 > b > \dfrac{1}{2}$	24.2	236.51
$2 > a > b > 1$	24.44	222.61
$2 > a = b > 1$	24.89	175.14
$2 > b > a > 1$	24.34	185.11

According to comparison results from Table 4.6.5.2, different geometrical configurations have a significant effect on the amount of running time but the difference in the average amount of cancellation can be neglected. The optimal geometrical configuration is when $2 > a = b > 1$ and this is consistence with the conclusion obtained from section 4.6.4.

4.6.6. The employment of the SOV filter and the inertial PSO algorithm

This case uses the second-order truncated Volterra (SOV) series as the adaptive filter and the inertial PSO algorithm as the parameter adjustment mechanism. The memory length is 9 and the order of the SOV is 54. There are two aims of this case study. The first one is to validate the cancellation capability and explore the effect of different geometrical configurations on the cancellation performance, and the second one is to compare the

83

cancellation performance of the FIR filter-based ANC system and the SOV filter-based ANC system, which provides instructions on the filter selection in Chapter 5.

Firstly, we use a 200 *Hz* sine wave, the representative of the narrowband noise, as the primary acoustic wave to identify the cancellation capability and explore the effect of different distance ratios on the degree of cancellation.

Table 4.6.6.1 presents the number and corresponding physical constraints.

Table 4.6.6.1. Number and corresponding distance ratio conditions

1	$2 > a > 1 > b > \dfrac{1}{2}$
2	$2 > a > b > 1$
3	$2 > a = b > 1$
4	$2 > b > a > 1$

Figure 4.6.6.1 qualitatively shows the cancellation performance in the presence of the residual noise signal magnitude (measured in dB).
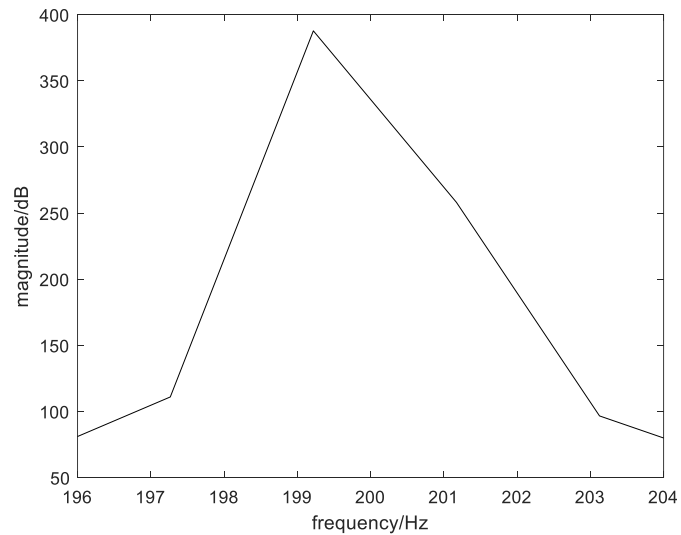
(a)
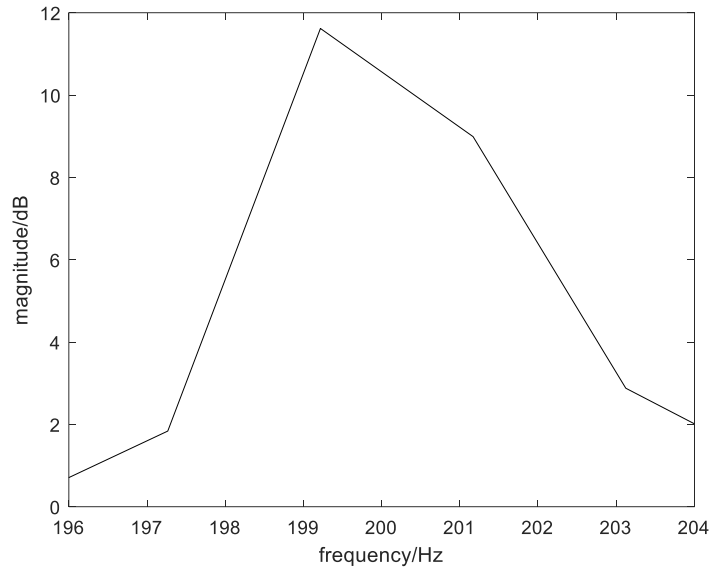
(b)
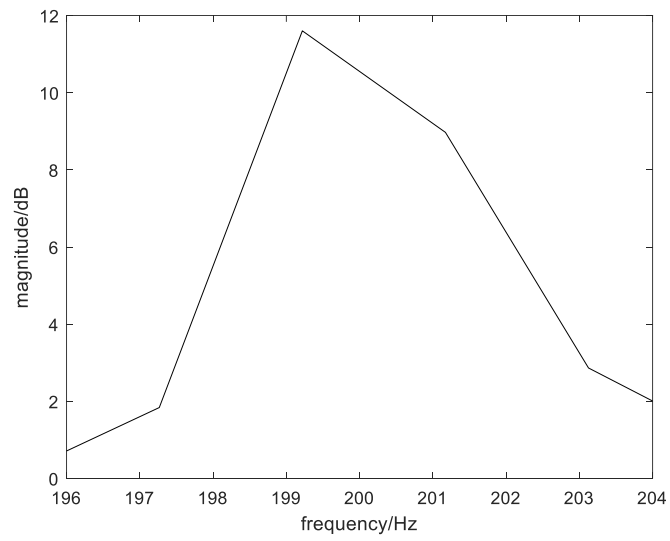
(c)

(d)

(e)

Figure 4.6.6.1. Cancellation performance of narrowband noise (a) original noise; (b) first distance ratio; (c) second distance ratio; (d) third distance ratio; (e) fourth distance ratio)

The simulation results in Figure 4.6.6.1 demonstrate the cancellation capability of the proposed ANC system for narrowband noise in the free-field acoustical environment. Figures 4.6.6.1b and 4.6.6.1c show that the residual noise signal magnitude is approximately 11.6 dB and 11.7 dB under the first and the second distance ratio respectively. Figures 4.6.6.1d and 4.6.6.1e show that the residual noise signal magnitude is 24.6 dB and 23.47 dB under the third and the fourth distance ratio respectively. It is found that the residual noise signal magnitude is

increasing with the increment of b, meaning the cancellation performance is degraded. In summary, the cancellation performance of the system with the narrowband noise shows that the effect of different distance ratios on the cancellation performance is significant and the cancellation performance of the narrowband noise is better when the value of b is smaller than the value of a.

Secondly, we use a Gaussian white noise with zero mean and unit variance, the representative of the broadband noise, as the primary acoustic wave and the geometrical constraints are same as presented in Table 4.6.6.1. The corresponding cancellation performance in the presence of the average amount of cancellation (measured in dB) is shown in Figure 4.6.6.2 and Table 4.6.6.2.

(a)

(b)

(c)

(d)

88
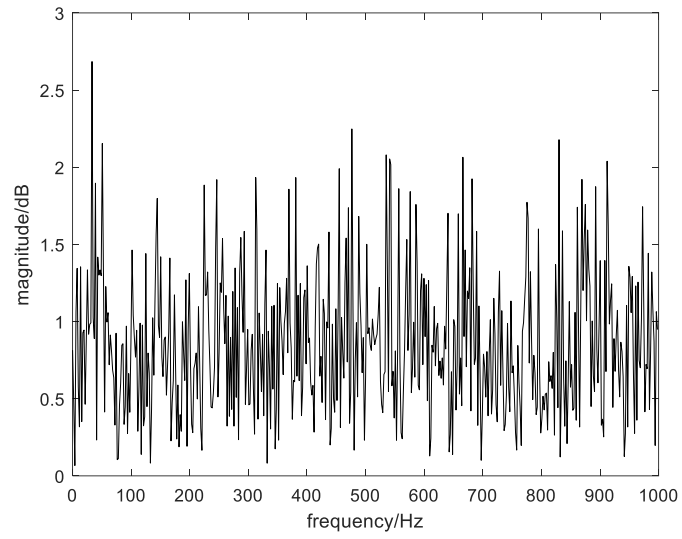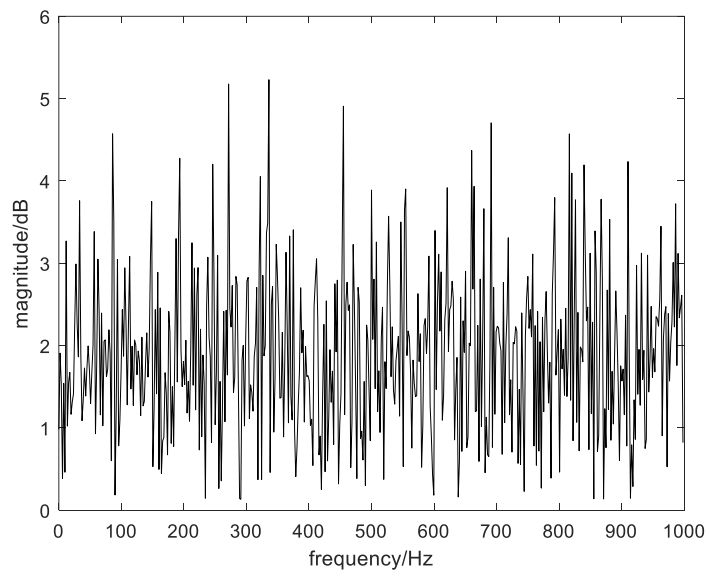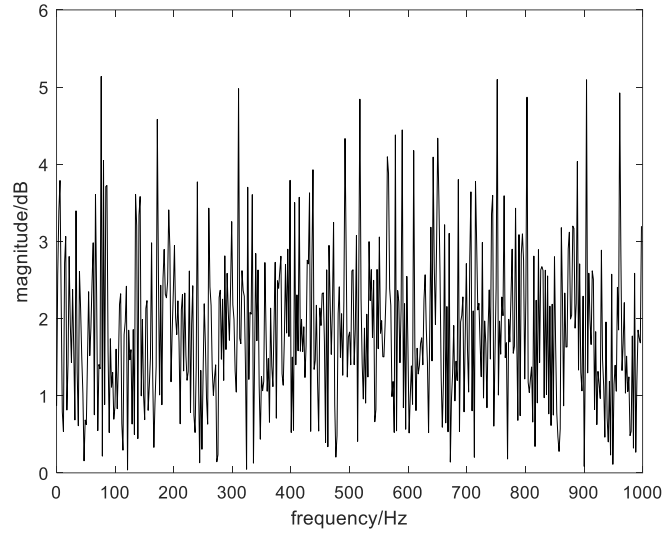
(e)

Figure 4.6.6.2. Cancellation performance of broadband noise (a) original noise; (b) first distance ratio; (c) second distance ratio; (d) third distance ratio; (e) fourth distance ratio)

Table 4.6.6.2. Average amount of cancellation (in dB) under different geometrical constraints

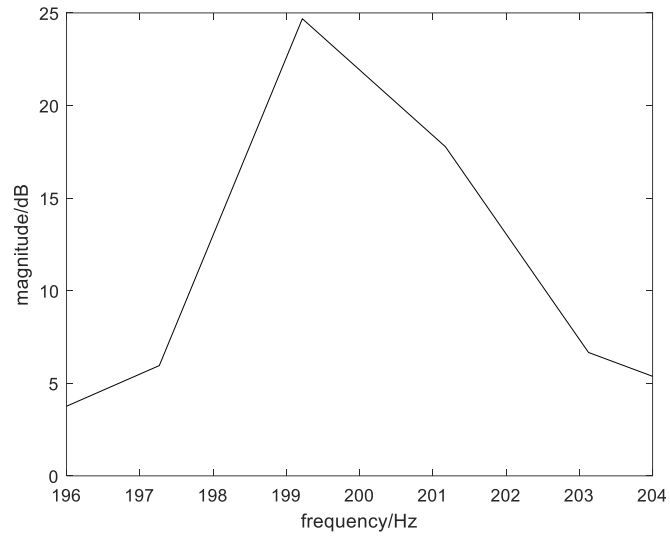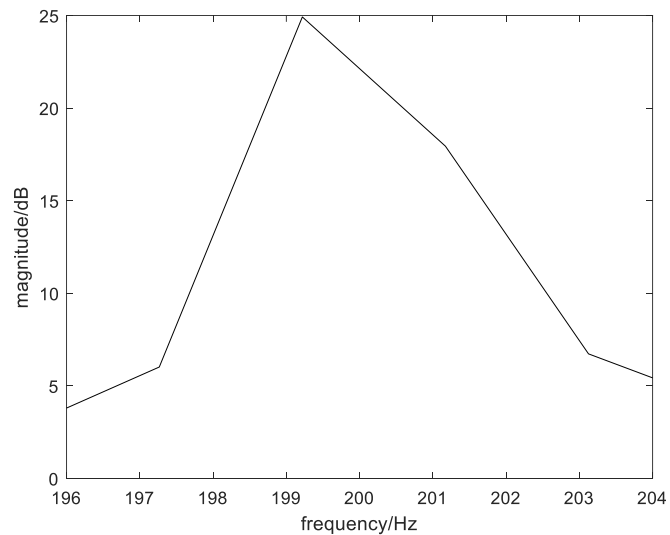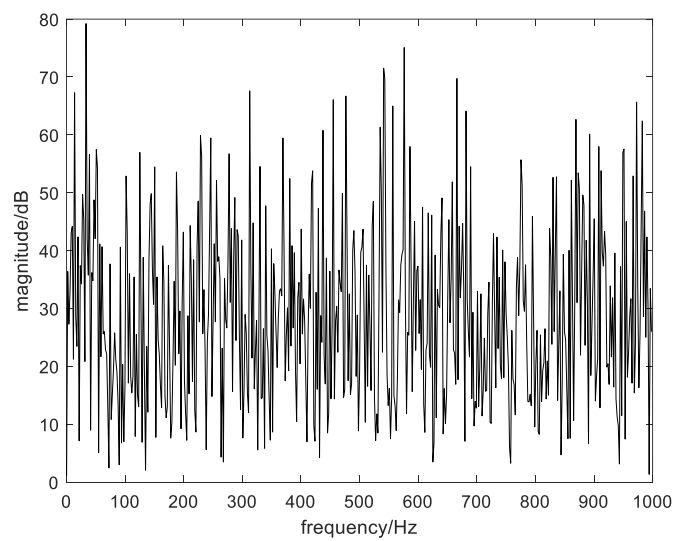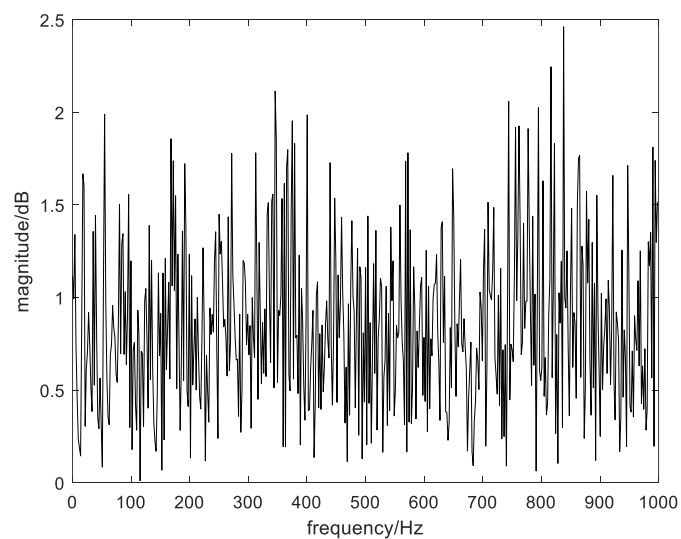| $2 > a > 1 > b > \dfrac{1}{2}$	$2 > a > b > 1$	$2 > a = b > 1$	$2 > b > a > 1$
0.8 dB	0.79 dB	0.8 dB	0.81 dB

The results in Figure 4.6.6.2 demonstrate the cancellation capability of the proposed ANC system for broadband noise. It is found that the maximum magnitude in Figures 4.6.6.2d and Figure 4.6.6.2e is more than twice of the maximum magnitude in Figures 4.6.6.2b and Figure 4.6.6.2c. Combine Figure 4.6.6.2 and Table 4.6.6.2, we can find that the difference in the average amount of cancellation is not big in comparison with the difference in the maximum magnitude.

Thirdly, we aim to compare the cancellation performance of the FIR filter-based ANC system and the SOV filter-based ANC system for the narrowband noise and the broadband noise.

Table 4.6.6.3 presents a summary of comparison of the residual noise signal magnitude of FIR filter-based and Volterra filter-based ANC systems under different distance ratios. The memory length of the FIR filter is 9, same as of the Volterra filter.

89

Table 4.6.6.3. The residual noise signal magnitude of FIR filter and Volterra filter (for narrowband noise)

Name	$2 > a > 1 > b > \dfrac{1}{2}$	$2 > a > b > 1$	$2 > a = b > 1$	$2 > b > a > 1$
FIR filter	11.6 dB	11.7 dB	24.8 dB	25 dB
Volterra filter	11.6 dB	11.56 dB	24.6 dB	23.47 dB
Difference[38]	+0 dB	+0.14 dB	+0.2 dB	+0.13 dB

Remark 14: Consider the difference between two filters is not significant, therefore, we do not present figures of cancellation performance of the FIR filter-based ANC system when employ the PSO algorithm.

Table 4.6.6.4 presents the relevant comparison of cancellation performance for broadband noise in terms of average amount of cancellation (measured in dB).

Table 4.6.6.4. Average amount of cancellation in dB of FIR filter and Volterra filter (for broadband noise)

Name	$2 > a > 1 > b > \dfrac{1}{2}$	$2 > a > b > 1$	$2 > a = b > 1$	$2 > b > a > 1$
FIR filter	0.85 dB	0.86 dB	1.89 dB	1.85 dB
Volterra filter	0.8 dB	0.79 dB	0.8 dB	0.81 dB
Difference	+0.05 dB	+0.07 dB	+1.09 dB	+1.04 dB

From the comparison result, we can find there is no significant difference between the FIR filter-based ANC system and the SOV filter-based ANC system regardless of the type of the primary acoustic wave.

Table 4.6.6.5 presents a comparison of the computational complexity.

Table 4.6.6.5. Comparison of computational complexity

Name	Memory length	Multiplication	Addition
FIR filter	N	N	N
Volterra filter	N	N	N(N+3)/2

As noted, with the value of N = 9 and the addition of Volterra filter is six times of the addition of FIR filter. Therefore, the computation load of the FIR filter is only 16.7% of the Volterra filter. Therefore, combine

---

[38] FIR-Volterra

results from Table 4.6.6.3, Table 4.6.6.4, and Table 4.6.6.5, we can find that the FIR filter-based ANC system is appropriate for noise cancellation and this gives instructions on the filter selection in Chapter 5.

4.7. Summary

This chapter contains 6 section. Section 4.1 proposes a geometrical configuration-based feedforward adaptive SISO ANC system for point source cancellation in the free field acoustic environment. The field cancellation factor is introduced to give an analytical relationship between the geometrical configuration and the degree of cancellation (the cancellation performance). Section 4.2 presents the geometrical constraints in the form of scalar quantities and section 4.3 presents the geometrical constraints in the form of vector quantities and the corresponding locus of system components in the two-dimensional Euclidean space are provided. Section 4.4 introduces the identification method for the FIR filter and section 4.5 introduces the nonlinear filter and several nonlinear parameter adjustment mechanisms. Section 4.6 contains several case studies, illustrates the principle of ANC systems, explore the effects of the effects of Δh_{34} and $\Delta\theta(\Omega)$ on K, demonstrates the cancellation capability of the proposed geometrical configuration-based adaptive feedforward ANC system, and explores the effects of different geometrical configurations on the cancellation performance. simulation results demonstrate the cancellation capability of the proposed ANC system and reflect that the optimal geometrical configuration is when $2 > a = b > 1$, which implies that within the reasonable physical constraints range, it is better to put the detector closer to the secondary source in comparison with the primary source. Besides, we can also find that it will be appropriate to choose the FIR filter as the digital filter in the proposed ANC system when consider both cancellation performance and computational complexity, which provides instructions on the filter selection in Chapter 5.

Chapter 5. The application of the proposed ANC system in noise cancellation of the turbulent flow around a circular cylinder : A two-dimensional case study

5.1. Introduction

The noise prediction by the turbulent flow over the bluff body is a challenging problem due to the complex physical phenomena (Cox et al., 1998). Three factors are accounting for the complex physical phenomena, the flow separation due to the adverse pressure gradient, the boundary layer becomes turbulent[39], and the vortex shedding due to the interaction between the upper shear layer and the bottom shear layer, which is also called as the von-Karman vortex street (Orselli et al., 2009). In the research field, researchers prefer to focus on a classical problem that noise generation of turbulent flow over a circular cylinder, a simple model of bluff bodies, and the reason is that this problem has a wide range of applications in real world and the aircraft landing gear noise is one of the popular representatives (Cox et al., 1998; Orselli et al., 2009; Liu et al., 2016; Cai et al., 2018; Liu et al., 2019).

To predict far-field (aeroacoustics) noise, researchers prefer to adopt the CAA technique and it has two forms, the direct approach, and the hybrid approach (Cai et al., 2018). The direct approach computes the sound together with its fluid dynamic source field by solving the compressible flow equations and the disadvantage is its higher computational cost (Ganta et al., 2019). The hybrid approach is based on a fundamental assumption that the unsteady flow generates sound and modifies its propagation, but the sound waves do not affect the flow in any significant way and it computes the sound in a post-processing step based on an aeroacoustics theory, which means the computation of flow is decoupled from the computation of sound. The far-field sound is obtained by integral or numerical solutions of acoustic analogy equations using computed source field data. Due to the fundamental assumption, the hybrid approach lies in flows at low fluctuating Mach numbers. In this case study, we mainly introduce the hybrid approach while the first stage is calculating the unsteady/transient flow and the second stage is the far-field noise calculation.

In the first stage, it is well known that the boundary layer and the wake region of the circular cylinder are two main factors affecting the flow regime and both factors are strongly depending on the Reynolds number (Re), defined as:

$$Re = \frac{\rho c D}{\mu_s} \tag{5.1.1}$$

---

[39] A kind of transition period.

where ρ denotes the density of the sound, c represents the free-stream sound velocity, D is the diameter of the circular cylinder and μ_s is the dynamic viscosity. When the value of Re between 0 and 180, the flow is two-dimensional and the laminar vortices are gradually shedding from the upper and the bottom of the circular cylinder and traveling in the wake region of the circular cylinder with the increasing of Re. When the Re increasing over 180, the flow field is three-dimensional as the vortex shedding appearing in the spanwise direction and the field is roughly divided into four regimes, subcritical, critical, supercritical, and transcritical based on the value of Re. The distinct differences among these four types of flow are the status of the boundary layer, where the boundary layer is gradually becoming turbulent with the increment of the Reynolds number. Currently, most researchers focus on the flow condition that $Re = 9 \times 10^4$ and the Mach number (Ma) is 0.2. The reason is that the flow is very sensitive, and the boundary layer is gradually becoming turbulent. In 1978, Revell et al. (1978) executed an experiment to explore the quantitative relationship between the drag coefficient and the far-field noise of the circular cylinder. The range of Re is $4.5 \times 10^4 < Re < 4.5 \times 10^5$ and the range of Ma is $0.1 < Ma < 0.5$. Their experimental results provided a strong reference for further researches. In 1996, Brentner et al. (1996) used two unsteady Reynolds-Averaged Navier-Stokes (RANS) solvers, CFL3D, to compute the unsteady flow for the circular cylinder in the two-dimensional computational space when the Ma is 0.2 and the Reynolds number based on the diameter of the circular cylinder is 9×10^4. They used the shear stress transport (SST) turbulence model in CFL3D, the k-ε turbulence model in CFL3D and simulation results reveal that the mean drag coefficient is 0.802 and the value of Strouhal number is 0.227. In 1997, Cox et al. (1997) used all existing computational methods to predict the unsteady flow field and associated flow-induced noise of the circular cylinder to validate their capability. In 2009, Orselli et al. (2009) used the ANSYS FLUENT CFD code to do a similar research topic like Cox et al. under the same value of Re. A summary of similar researches can be found in several review papers (Cai et al., 2018; Liu et al., 2019). The second stage is to predict the far-field noise. The Ffowcs Williams and Hawkings (FW-H) equation, the most general form of the Lighthill acoustic analogy, is the widely used governing equation to post-process the computed source field data in recent several years and the biggest advantage is that it is appropriate for bodies in arbitrary motion.

Recent control strategies for aeroacoustics noise can be categorized as two domains, passive flow control (e.g. splitter plates, acoustic liners, slat cove cover, and fairings), and active flow control (e.g. dielectric barrier discharge (DBD) plasma actuators, air blowing, and suction). For passive flow control, the amount of cancellation in the presence of overall sound pressure level (OSPL) concentrates at 2 dB. For active flow control, Thomas et al. (2008) applied the DBD plasma actuator in the noise reduction of a single circular cylinder and results reflected

that sound pressure levels (SPLs) associated with shedding were reduced by 13.3 dB in near field. In 2009, Kozlov and Thomas also applied the DBD in the same noise cancellation problem with different flow conditions. Experimental results reveal that the amount of noise reduction is 12.6 dB and 14 dB in the streamwise direction and the spanwise direction respectively. Related summaries can be found in Yong's review paper and in summary, the active flow control has a better cancellation performance in comparison with the passive flow control.

5.2. Problem definition

Figure 5.2.1 presents a schematic diagram of the turbulent flow around a circular cylinder in the two-dimensional computational domain (Cox et al., 1997; Orselli et al., 2009).
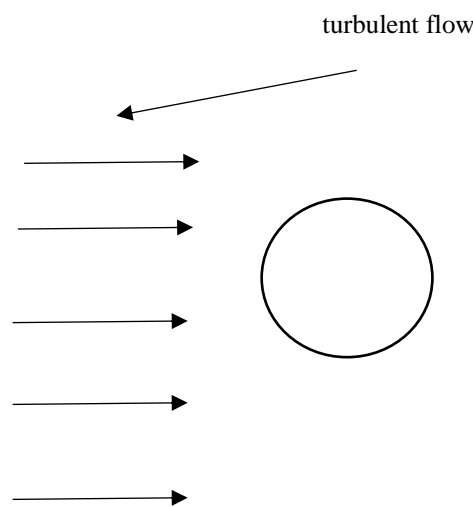
turbulent flow

Figure 5.2.1. Turbulent flow over a circular cylinder in the two-dimensional computational domain

The diameter (*D*) of the circular cylinder is 0.019 meters, the Reynolds number (based on the cylinder diameter) is 90,000, the Ma is 0.2, and the free-stream sound velocity is $340 \, m/_s$. All these parameters are the same as previous experiments executed by Revell et al (1978) and simulation experiments by Cox et al (1998) and Orselli et al (2009), which is convenient for further validation.

Our objective is to cancel the low-frequency range of far-field (aeroacoustics) noise and numerically explore the appropriate geometrical configuration, which provides instructions on the future practical experiments.

5.3. Method

Flow field method

Firstly, we use the ICEM software to obtain a good quality mesh. The computational domain is a rectangular with *21D* in the *x*-direction and *11D* in the *y*-direction. The inlet and outlet boundaries exist at a distance of *8.5D* and *20.5D* to the cylinder axis in the *x*-direction respectively. The up and bottom boundaries are

located at an equidistance to the cylinder axis in the y-direction. The cylinder surface is discretized with 240 volume cells and the non-dimensional wall distance y^+ is 1, equal to the 1st layer height approximately 4.1×10^{-6} meters to guarantee the resolution of the near-wall flow. A 1.05 and 1.1 expansions are used in the radial height near and far away from the cylinder respectively (Orselli et al., 2009).

Table 5.3.1 presents related parameters for the Hexa mesh.

Table 5.3.1. Parameters (Orselli et al., 2009)

Name of parameter	Value
Diameter of the cylinder	0.019m
Length in x-direction	0.551m
Length in y-direction	0.399m
Mach number	0.2
Reynolds number	90,000
y^+	1
Around the surface	240

Step 1: Generate points and curves

Use to generate points and to make curve.

Step 2: Parts generation and initial blocking

Right click to create a new part and select the corresponding entity and assign the corresponding name. In this mesh, the left side, the right side, the top and bottom sides, and the surface of the circular cylinder are assigned as 'Inlet', 'Outlet', 'Symmetry', and 'Wall'. Then we need to initialize block and the path is 'Blocking'>'Create Block'>'Initialize Blocks'.

Step 3: Associate entities to the geometry

The path that associates entities to the geometry is: 'Blocking'>'Associate' >'Associate Edge to Curve' . Here, it is useful to check whether any leaking points through the colour of edges. The yellow means that the curve has attached to a single surface and the green reveals that the curves has not attached to a single surface.

Step 4: Blocking (O-grid)

The path is 'Blocking'> and, in the 'Split Method' drop-down list, select 'Prescribed point'.

Step 5: Generate the mesh

A non-dimensional wall distance for a wall-bounded flow can be defined in the following way:

$$y^+ = \frac{u_\tau \triangle y}{\nu} = \frac{\sqrt{\frac{\tau_{wall}}{\rho}} \triangle y}{\nu} = \frac{\sqrt{\frac{\frac{1}{2} C_f \rho u^2}{\rho}} \triangle y}{\nu} \tag{5.3.1}$$

Where

u_τ : The friction velocity, $u_\tau = \sqrt{\frac{\tau_{wall}}{\rho}}$

ρ : The fluid density at the wall

τ_{wall}: The wall shear stress, $\tau_{wall} = \mu \left(\frac{\partial u}{\partial y}\right)_{y=0}$, $Pa = \frac{kg}{ms^2}$

u: The flow velocity parallel to the wall

$\triangle y$: The distance to the nearest wall

ν : The local kinematic viscosity of the fluid

Secondly, we choose the CFD technique, which is executing via the FLUENT CFD finite-volume code, to do the unsteady flow field calculation. The RANS two-layer $k - \omega$ shear stress transport (SST) of Menter (1992) is selected as the turbulence model and the reason is that the model gives good results for flow characterized by zero pressure gradient and adverse pressure gradient boundary layers and this makes it more appropriate for the problem of the flow over the cylinder (Cox et al., 1998; Orselli et al., 2009). Besides, it is the most widely used turbulence model and sufficient validate data are available for us to validate our simulation results.

The SIMPLE scheme is used for the pressure-velocity coupling, the second order implicit scheme is employed for transient formulation, and the second order upwind scheme is employed for pressure and momentum The time step size Δt is 4.75×10^{-6}, equals to the dimensionless time step Δt* is 0.0173, smaller than 0.02, which is sufficient to obtain a reliable transient flow field (Kazeminezhad et al., 2010). Meanwhile, for each time step, 20 inner iterations are employed for convergence of the equations.

Aeroacoustics field method

In the acoustic analogy approach, the obtained near-field flow is used as a sound source input into the wave equations to predict the mid-to-far-field noise. In this case study, we use the FW-H equation and its integral solution to predict the far-field noise. To understand the FW-H equation, firstly, we need briefly review the Lighthill's acoustic analogy.

The Lighthill's acoustic analogy can be used for the free flow and it is obtained by rearranging the compressible Navier-Stokes equation (Cai et al., 2018), it follows that:

$$\frac{\partial^2 \rho}{\partial t^2} - c_\infty^2 \nabla^2 \rho = \frac{\partial^2 T_{ij}}{\partial x_i \partial x_j} \tag{5.3.2}$$

Where:

c_∞: the far-field sound velocity

ρ: the density of fluid

The Lighthill stress sensor T_{ij} is defined as:

$$T_{ij} = \rho u_i u_j + P_{ij} - c_\infty^2 (\rho - \rho_0)\delta_{ij} \tag{5.3.3}$$

Where u_i and u_j are velocity component, δ_{ij} is the Kronecker delta and P_{ij} is the compressive stress sensor, which is expressed as:

$$P_{ij} = p_{steady}\delta_{ij} - \mu[\frac{\partial u_i}{\partial x_j} + \frac{\partial u_j}{\partial x_i} - \frac{2}{3}\frac{\partial u_k}{\partial x_k}\delta_{ij}] \tag{5.3.4}$$

Where p_{steady} is the statistic pressure of the fluid and $\mu[\frac{\partial u_i}{\partial x_j} + \frac{\partial u_j}{\partial x_i} - \frac{2}{3}\frac{\partial u_k}{\partial x_k}\delta_{ij}]$ is called the viscous stress tensor.

The FW-H equation (analogy) can be treated as an extension of the Lighthill's acoustic analogy as it considers the effect of the moving boundaries, it follows that:

$$\frac{1}{c_\infty^2}\frac{\partial^2 p'}{\partial t^2} - \nabla^2 p' = \frac{\partial}{\partial t}\{[\rho_\infty v_n + \rho(u_n - v_n)]\delta(f)\} - \frac{\partial}{\partial x_i}\{[P_{ij}n_j + \rho u_i(u_n - v_n)]\delta(f)\}$$

$$+ \frac{\partial^2}{\partial x_i \partial x_j}\{T_{ij}H(f)\} \tag{5.3.5}$$

Where:

$f = 0$: the source (emission) surface

$f > 0$: exterior region

u_i : fluid velocity in x_i direction

v_i : surface velocity in x_i direction

u_n : fluid velocity normal to the surface $f = 0$

v_n : surface velocity normal to the surface $f > 0$

p' : sound pressure in the far-field area

$H(f)$: Heaviside function

$\delta(f)$: Dirac delta function

n_j : the unit normal vector pointing toward $f > 0$

The right side of Eq. (5.3.5) is consists of three acoustic source terms and they represent monopole source, dipole source, and quadrupole source, respectively. The monopole source refers to the noise generated by the displacement of the fluid by the moving surfaces. The dipole source accounts for the noise generated by the fluctuating forces on the body surfaces. The quadrupole source is a volume distribution and it accounts for the noise generated by the off-body fluctuating stresses of the fluid. The monopole source and the dipole source can be solved when substitute the free-space Green function, $\delta(g)/4\pi r$ [40] in Eq. (5.3.5) and the quadrupole source is obtained from the volume integrals.

In ANSYS FLUENT software, the volume integrals are dropped and the procedures of implementing the FW-H model in ANSYS are presented as follows.

Step 1: Obtained flow field data.

Consider the transient condition, therefore, we need to make sure that it comes to a statistically steady-state condition, which is normally evaluated through the time history of the lift coefficient or the drag coefficient. The steady-state condition implies that all the major flow variables have been fully developed as their statistics are not changing with time.

Step 2: Enable the FW-H model.

Step 3: Specify the source surface.

Remark 1: The 'Write Frequency' determines the maximum frequency of the aeroacoustics noise and this value is critical as the later sampling frequency depends on this.

Step 4: Specify the receivers.

The receiver[41] is employed at a distance of *128D* away from the cylinder axis and an angle of 90 degrees from the cylinder stagnation point.

Step 5&6: Run the simulation again, compute the sound pressure signals and save.

Here, the vortex shedding in the spanwise has a significant effect on the noise pressure level. To evaluate this, the acoustic correlation length (Cox et al., 1998) or fluid spanwise correlation length (Norberg, 2002) is proposed. According to Cox et al (1998), the value of the acoustic correlation length varies with the value of Reynolds number and is approximately *2-4D* for the critical Reynolds number. In 2002, Norberg gave a value of

---

[40] $g = t - \tau - r/c$, t means the observer time, τ denotes the source time and r is the distance to the observer.

[41] We use only one receiver in the first case study because of simplicity.

3.16D from the experiments (Norberg, 2002). In 2009, Orselli et al. pointed that in order to use the two-dimensional CFD results as an input data for the acoustic computations, the acoustic correlation length should be at least *5D*. In this case study, we choose *5D* as the acoustic correlation length.
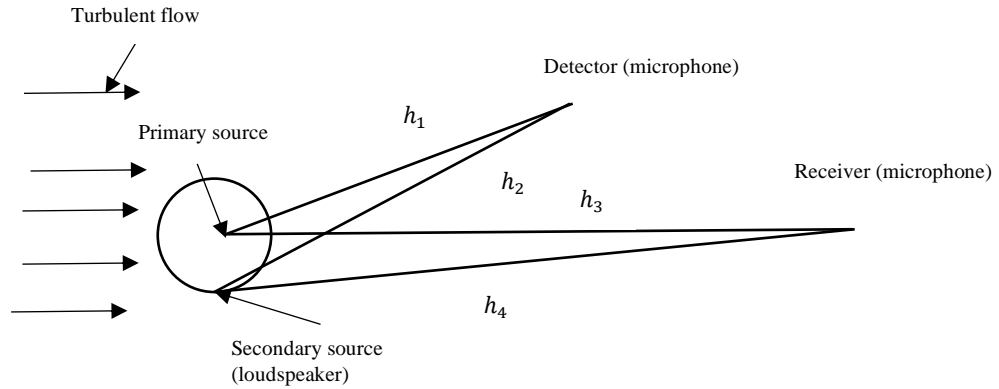
Noise Cancellation method

Now, we apply the proposed ANC system in cancelling the low-frequency range of the obtained far-field (aeroacoustics) noise. According to the discussions from section 4.6.6, we use the FIR filter as the digital filter. Besides, we choose the conventional type-I ANFIS technique as the parameter adjustment mechanism.

Locus of system components in the two-dimensional computational space

Firstly, we need to clarify the concept of the dispersive and the non-dispersive propagation medium. When the sound wave traveling through the non-dispersive medium, the sound speed only depends on the property of the medium, therefore, its value is a constant and independent on the frequency of the sound. In contrast, a dispersive medium is a medium that the sound velocity is affected by the frequency component of the sound, which means sound waves at different frequency travels at a different speed. In practice, the air is a non-dispersive propagation medium and the building and other structures are dispersive mediums.

Secondly, we need to consider the effect of the near-field and the far-field. The sound pressure in near-filed is complicated and it is difficult to predict, and the inverse square law can only be applied in the far-field region of the real source. Therefore, to analyse it convenient, we use the average sound pressure in the following section.

Figure 5.3.1 presents a schematic diagram of the application of the proposed ANC system in noise cancellation of the turbulent flow around a circular cylinder in the two-dimensional computational domain.

Figure 5.3.1. A schematic diagram of the application of the proposed ANC system in the flow-induced noise cancellation (two-dimensional computational domain)[42]

Now we can obtain the locus of system components in the two-dimensional computational space through repeating procedures in section 4.3.

Remark 2: In this case study, consider the practical constraint that the secondary source must be located on the circular cylinder or within the circular cylinder, therefore, the range of both u and v is $\left[-\frac{D}{2}, \frac{D}{2}\right]$.

The conventional type-I ANFIS technique

Soft computing technique, a consortium of methodologies that works synergetically, is good at handing real life ambiguous situations. It aims to exploit the tolerance for imprecision, uncertainty, approximate reasoning, and partial truth to achieve tractability, robustness, and low-cost solutions, which is different from the traditional hard computing technique. The guiding principle of the soft computing technique is to devise methods of computation that lead to an acceptable solution at a low cost by seeking for an approximate solution to an imprecisely/precisely formulated problem. Artificial neural networks (ANNs) and FLC systems are two types of commonly used soft computing techniques. A brief introduction of the FLC systems is provided in Chapter 4 and we know that the fuzzy logic technique is good at improving the reasoning and inference in a learning machine and we can use it when sufficient expert knowledge about the process is available (Mitra et al., 2000; Shihabudheen and Pillai, 2018). The concept of ANNs was inspired by biological neural networks (BNN's) and it attempts to solve complex problems efficiently through using principles from nervous systems (Tang et al., 2020). The biggest advantage of the ANNs technique is the learning capability and it is appropriate when sufficient process data are available or measurable. In summary, both ANNs technique and fuzzy logic technique build

---

[42] The adaptive FIR controller is placed on the circular cylinder.

nonlinear systems based on bounded continuous variables while the difference is that ANNs are treated numerically and the FLC systems are treated in a symbolic qualitative manner (Mitra et al., 2000).

Recently, the neuro-fuzzy integration technique, which combines the advantages of both ANNs technique and fuzzy logic technique, has become a new research hotspot (Ren et al., 2020) and the ANFIS technique is the best representative.

In this case study, we adopt the conventional type-I ANFIS technique as the parameter adjustment mechanism to tune the coefficients of the FIR filter. Detailed descriptions of corresponding procedures can be found in section 4.5.

5.4. Results and analysis

Aerodynamic results

As stated in section 5.3, the near-field unsteady flow results are used as an input data to the FW-H equation to predict the far-field noise, therefore, the accuracy of the CFD results directly determine the accuracy of the noise prediction results. To evaluate the accuracy of the numerical simulations, we normally quantitatively and qualitatively compare it with the available experimental results.

From the quantitative perspective, we select the mean drag[43] (mean flow quantity) and the Strouhal number ($St = \frac{f_s D}{U}$, $where\ f_s\ is\ the\ shedding\ frequency$) (fluctuating quantity) as benchmark parameters for evaluating the quality of the CFD results in comparison with its corresponding available experimental data. Table 5.4.1 shows the obtained results of the two-dimensional unsteady RANS $k - \omega\ SST$ model.

Table 5.4.1. Results of the two-dimensional unsteady RANS $k - \omega\ SST$ model

Name of the parameter	This case study	Orselli et al (2009)	Norberg et al (2002)
Mean drag coefficient	1.023	1.09	1.0-1.4
Strohaul[1] number	0.25	0.247	0.18-0.191

[1] Theoretically value at this Reynolds number is 0.2.

---

[43] The equations of calculating lift and drag coefficient are: $C_l = \frac{2F_l}{\rho u^2 S}$ and $C_d = \frac{2F_d}{\rho u^2 S}$, where S denotes the reference area. To obtain the mean C_l and C_d, in the Fluent software, check the value of area and length in the 'Reference values' part.

Besides, the time history of the aerodynamic forces (lift and drag) acting on the cylinder obtained by the unsteady RANS $k - \omega\ SST$ model is presented in Figure 5.4.1.
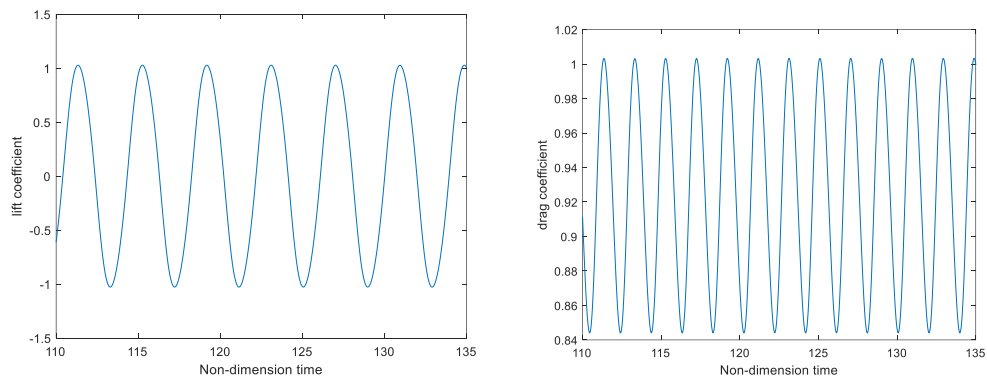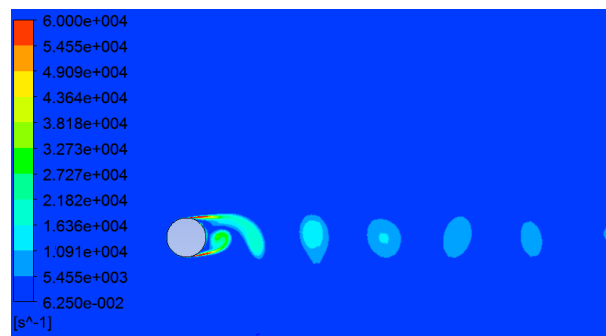

Figure 5.4.1. Time history of lift and drag coefficients (left: lift coefficient; right: drag coefficient)

Figure 5.4.2 presents a qualitative view of the numerical results obtained by the two-dimensional $k - \omega$ SST model where the vorticity magnitude contours at an instant of time.
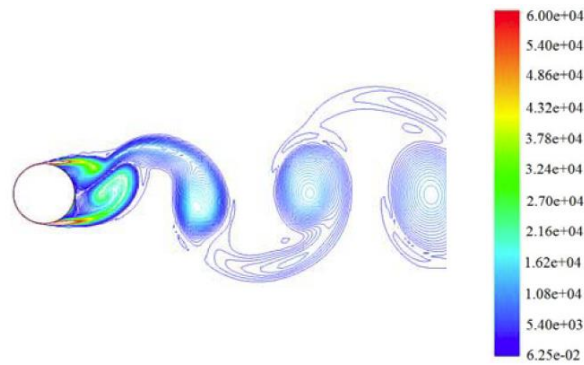

(a)

(b)

Figure 5.4.2. Flow field results ((a). Orselli et al. (2009); (b). This case study)

Aeroacoustics results

102

In this case study, because of low Mach number, the contribution of quadrupole sources is not very significant, thus most of the sound is generated on wall surfaces (dipole and monopole sources). Therefore, the acoustic spectrum was here computed considering all noise sources being generated on the cylinder wall surface. Figure 5.4.3 presents the aeroacoustics spectrum [44] under the condition that the acoustic correlation length is *5D*.
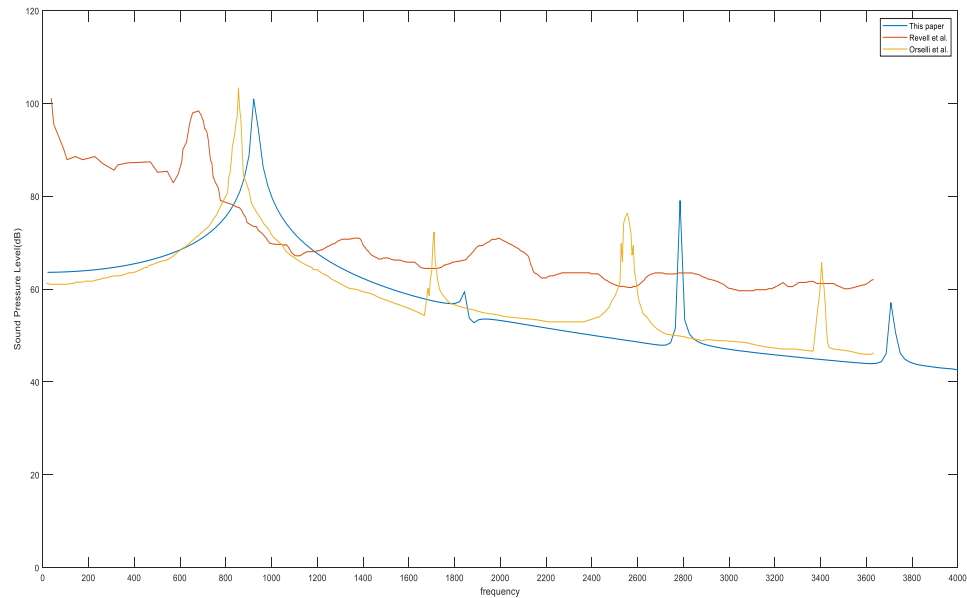
**Figure 5.4.3.** Aeroacoustics spectrum

Cancellation performance

The maximum frequency of the flow-induced noise[45] is approximately 10,244 *Hz*, therefore, in this simulated experiment, we use 25,000 *Hz* as the sampling frequency based on the Nyquist–Shannon sampling theorem.

The mathematical models of the microphone and the loudspeaker are the same as descriptions in section 4.7 and the order of the FIR filter is 21. Based on descriptions in section 5.3, the coordinate of the receiver point is (2.432,0) and the maximum distance between the primary source and the secondary source is 9.5e-3 meters.

Figure 5.4.4 presents the cancellation performance in the presence of the residual noise signal magnitude (measured in dB) under different geometrical configurations.

---

[44] The data obtained from the ANSYS FLUENT is saved in the format of ASD. Use MATLAB 'import' function to directly import. Here the data is stored on the workspace in the form of matrix. There are several different ways of importing data to the Simulink platform and in this case we adopt through 'From Workspace' block. The function of the 'From Workspace' block is to read signal data from a workspace and outputs the data as a signal.
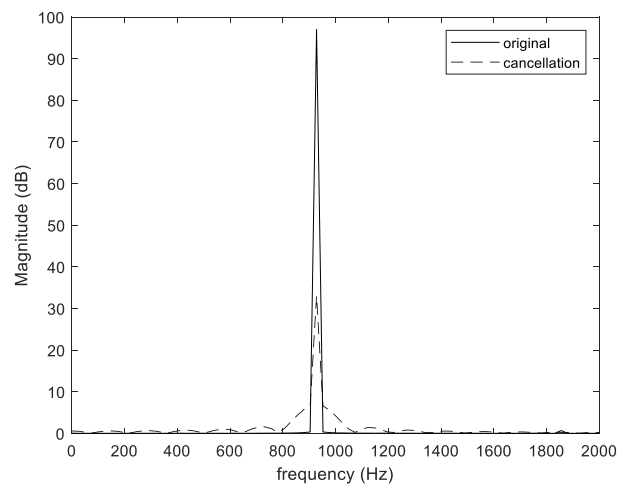
[45] For a given time step Δt, the highest frequency that the acoustic analysis can produce is $f = 1/(2\Delta t)$.
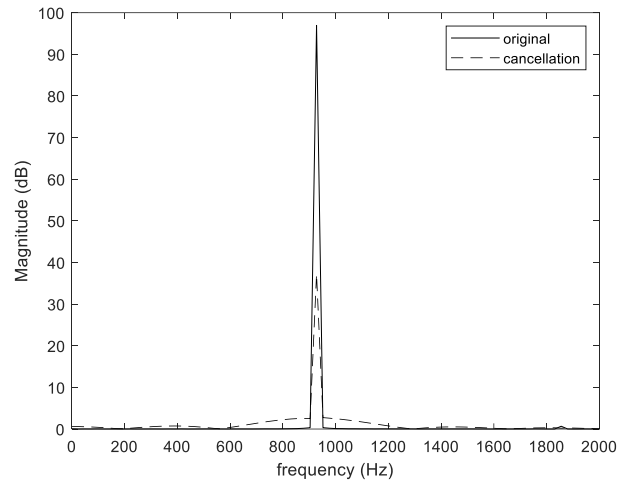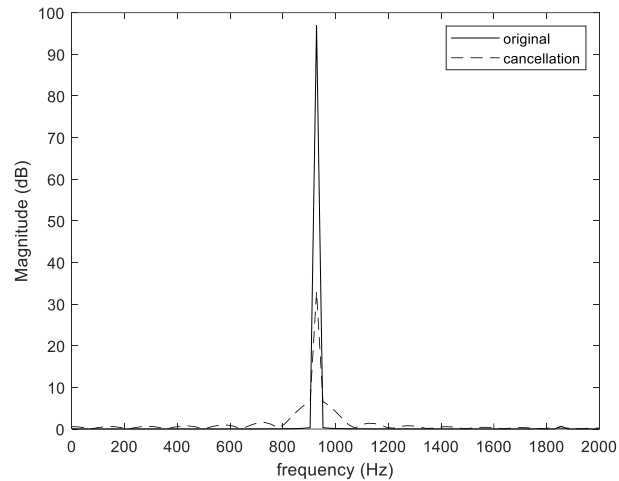
(a)
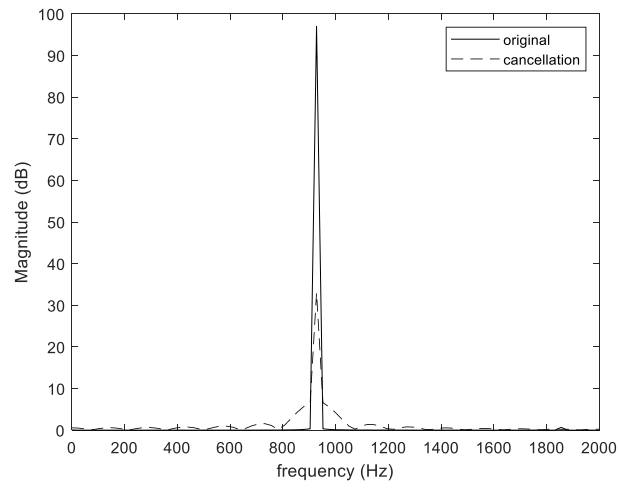
(b)

(c)

(d)

Figure 5.4.4. Cancellation results in presence of the magnitude of the residual noise signal ((a) $a > 1 > b$ 37.22 dB; (b) $a > b > 1$ 33.01 dB; (c) $a = b > 1$ 33.02 dB; (d) $b > a > 1$ 33.02 dB)

Analysis

As for the aerodynamic results, Figure 5.4.1 reflects that the two-dimensional unsteady RANS model predicts an almost perfectly periodic flow which indicates the presence of a fully spanwise correlated main vortex shedding. Comparison results from Table 5.4.1 reveal that all two-dimensional simulations predict a slightly higher shedding frequency when compared to the experimental data, which is an expected CFD result of the two-dimensional case study. Comparison results from Figure 5.4.2 demonstrate that the flow is almost characterized by a great alternating vortex shedding because of the similar shape and dissipation at this Reynolds number.

As for the aeroacoustics results, Figure 5.4.3 presents the acoustic spectrum obtained for the acoustic representative span length in *5D.* (the blue line: this case study; the orange line: a similar simulation case study (Orselli et al., 2009); the red line: the experimental data). The *x*-axis represents the frequency and the *y*-axis denotes the sound pressure level (SPL) in decibel (dB). In comparison with the similar previous work, the accuracy of the obtained acoustic spectrum in this case study can be validated with reasonable error because of the mesh resolution and the computer capacity. It is observed that the two-dimensional approach can only predict discrete values of sound pressure level (SPL) associated with the fundamental frequency (Strouhal number) and its harmonics.

For the noise cancellation performance, cancellation results from Figure 5.4.4 reflect that a significant reduction is achieved around 900 *Hz*, which demonstrates the cancellation capability of the proposed ANC system for the low-frequency range of far-field (aeroacoustics) noise. Besides, cancellation results imply that within the

reasonable physical constraints range, the cancellation performance will better if the detector is closer to the secondary source when compared to the primary source. From the physical phenomenon perspective, the secondary source generates both upstream and downstream radiations, and the detector (microphone) detects the upstream radiation of the secondary acoustic wave, which is called the acoustic feedback. Normally, the electrical signal with a specified frequency is traveling faster when compared to an acoustic wave at the same frequency and the electrical delay, caused by the electrical signal, is the reason accounting for the phase difference between two waves. Therefore, a relatively shorter acoustic feedback path contributes to making the primary acoustic wave and the secondary acoustic wave arriving the detector at a similar time, which minimizes the negative effects of the acoustic feedback wave signal. From the mathematical perspective, under this condition, the decrease of the acoustic feedback path h_2 results in a bigger field cancellation factor K, which implies a better cancellation performance. This conclusion provides instructions for future practical experiments about how to locate the secondary source inside the flow field to satisfy different cancellation requirements.

5.5. Summary

This chapter presents a two-dimensional case study about the application of a geometrical configuration-based feedforward ANC system in cancelling the low-frequency range of far-field aeroacoustics noise. Simulation and comparison results validate the accuracy of the obtained acoustic spectrum in this case study with reasonable error because of the mesh resolution and the computer capacity. Cancellation results demonstrate the cancellation capability of the proposed ANC system for the low-frequency range of far-field (aeroacoustics) noise and the cancellation performance will be better when the detected sensor is placed closer to the secondary source in comparison with the primary source. This conclusion provides useful general instructions on future practical experiments, but detailed physical distance value must be dependent on individual cases. Future works can be implemented from three aspects, the first aspect is to expand the two-dimensional calculation to the three-dimensional calculation, aims at increasing the accuracy of the acoustic results , the second aspect is to design the feedforward ANC system for dipole source or multiple-source cancellation, which guarantees the cancellation of the full frequency range of aeroacoustics noise, and the third aspect is to execute the physical experiments to validate the numerical and simulation conclusions or provide some supplements.

Chapter 6. Conclusions

This thesis presents a study about the application of a proposed geometrical configuration-based adaptive feedforward ANC system for the low-frequency range of flow-induced (aeroacoustics) noise cancellation and the investigation on the effects of different geometrical configurations on the noise cancellation performance.

The geometrical configuration-based adaptive feedforward ANC system is proposed based on the Leitch and Tokhi's works. The acoustical physical paths are constructed from the perspective of noise pressure level, the adaptive FIR filter acts as the digital filter for processing the input reference signal and the output signal is used for driving the loudspeaker to generate the secondary acoustic wave. The soft computing technique (e.g. ANFIS and PD-like FLC) and the evolutionary-computing-based technique (e.g. PSO algorithm) are employed as the parameter adjustment mechanism to cope with the nonlinearity problem, which is caused by microphones and loudspeakers. The physical constraints are provided in both scalar quantities and vector quantities. Scalar quantities aim at reflecting the change of the magnitude and vector quantities aim at reflecting both direction and magnitude variation in two, three, or multiple-dimensional space, which depends on the practical problem. In comparison with scalar quantities, vector quantities are more appropriate to reveal the locus of system components under different geometrical configurations. Simulation results firstly reflect that better cancellation performance or a reduced amount of simulation time can be achieved when the adaptive filter is identified before the beginning of the adaptive control. Secondly, the simulation results demonstrate the cancellation capability of the proposed ANC system for both narrowband noise and broadband noise. Meanwhile, it reveals that the cancellation performance will be better when the detector is closer to the secondary source when compared to the primary source. The secondary loudspeaker radiates the acoustic wave into the propagation medium, the microphone (detected sensor) detects the upstream acoustic wave, and this is called acoustic feedback, which can be treated as a kind of disturbance during the process of noise cancellation. Therefore, within the reasonable physical constraints range, a proper length of the acoustic feedback path will contribute to improving the cancellation performance.

A two-dimensional case study about the application of a geometrical configuration-based feedforward adaptive ANC system in cancelling the low-frequency range of far-field (aeroacoustics) noise is completed. The physical background of this case study is the vicious flow over the bluff body, the simplest and classical model of the landing gear noise. Both unsteady flow results and aeroacoustics results demonstrate the accuracy of the aeroacoustics data within a reasonable error. Cancellation results demonstrate the cancellation capability of the proposed ANC system for the low-frequency part of the far-field (aeroacoustics) noise cancellation and the

cancellation performance is better when the detector is closer to the secondary source when compared to the primary source.

Future works can be done from two parts, which are specified as follows:

1. This thesis mainly focuses on the ANC technique, which attenuates the noise pressure level during the propagation path. However, the PNC technique has its own advantages for noise cancellation. Therefore, in the future, we would like to apply the hybrid noise control technique in the aeroacoustics noise cancellation. The PNC technique can be used at the noise source or at the receiver position, which enhances the cancellation performance or improves the sound quality.

2. This thesis presents theoretical deduction and several simulated experiments. However, we still need to validate these outcomes in practice. Besides, the flow-induced noise is an important and heated field in daily life (e.g. air condition and vehicle). Therefore, we would like to do some physical experiments to validate and improve the obtained results, which can be applied to practical problems in real life.

References

Flow-induced noise

Revell, J.D. (1974) On the calculation of aerodynamic noise generated by large aircraft at landing approach. *The Journal of the Acoustical Society of America.* 55 (S1), pp. S73.

Revell, J.D., Prydz, R.A. and Hays, A.P. (1978) Experimental Study of Aerodynamic Noise vs Drag Relationships for Circular Cylinders. *AIAA Journal.* 16 (9), pp. 889-897.

NASA Langley Research Center (1991) *Aeroacoustics of Flight Vehicles: Theory and Practice. Volume 1: Noise Sources.* Washington, United States. Hampton: NASA Langley Research Center.

Cox, J.S., Brentner, K.S. and Rumsey, C.L. (1998) Computation of Vortex Shedding and Radiated Sound for a Circular Cylinder: Subcritical to Transcritical Reynolds Numbers. *Theoretical and Computational Fluid Dynamics.* 12, pp. 233-253.

Dobrzynski, W., Nagakura, K., Gehlhar, B. and Buschbaum, A. (1998) Airframe Noise Studies on Wings with Deployed High-Lift Devices. *4th AIAA/CEAS Aeroacoustics Conference.* Toulouse, France, 02-04 June. AIAA-1998-2337.

Dobrzynski, W., Gehlhar, B. and Buchholz, H. (2001) Model- and full scale high-lift wing wind tunnel experiments dedicated to airframe noise reduction. *Aerosp Sci Technol.* 5 (1), pp. 27-33.

Smith, M.G. and Chow, L.C. (2002) Validation of a Prediction Model for Aerodynamic Noise from Aircraft Landing Gears. *8th AIAA/CEAS aeroacoustic Conference.* Breckenridge, Colorado, 17-19 June. AIAA-2002-2581.

Norberg, C. (2002) Fluctuating Lift on a Circular Cylinder: Review and New Measurements. *J. Fluids and Structures.* 17 (1), pp. 57-96.

Dobrzynski, W., Chow, L.C., Guion P. and Shiells, D. (2002) Research into landing gear airframe noise reduction. *8th AIAA/CEAS aeroacoustic Conference.* Breckenridge, Colorado, 17-19 June. AIAA-2002-2409.

Chow, L.C., Mau, K. and Remy, H. (2002) Landing Gears and High Lift Devices Airframe Noise Research. *8th AIAA/CEAS aeroacoustic Conference.* Breckenridge, Colorado, 17-19 June. AIAA-2002-2408.

Jenkins, L.N., Khorrami, M.R. and Choudhari, M.M. (2004). Characterization of Unsteady Flow Structures Near Leading-Edge Slat: Part I. PIV Measurements. *10th AIAA/CEAS aeroacoustic Conference.* Manchester, GREAT BRITAIN, 10-12 May 2004. AIAA-2004-2801.

Khorrami, M.R., Choudhari, M.M. and Jenkins, L.N. (2004) Characterization of Unsteady Flow Structures Near Leading-Edge Slat: Part II. 2D Computations. *10th AIAA/CEAS aeroacoustic Conference*. Manchester, GREAT BRITAIN, 10-12 May 2004. AIAA-2004-2801.

Guo, Y., Stoker, R.W. and Yamamoto, K.J. (2006) Experimental Study on Aircraft Landing Gear Noise. *J. of Aircraft.* 43 (2), pp. 306-317.

Farassat, F. and Casper, J. (2006) Towards an airframe noise prediction methodology: survey of current approaches. *44th Aerospace Sciences Meeting and Exhibit.* Reno, Nevada, 9–12 January 2006. AIAA-2006-0210.

Huang, X., Chan, S. and Zhang, X. (2007) Atmospheric plasma actuators for aeroacoutic applications. *IEEE Trans Plasma Sci.* 35 (3), pp. 693-695.

Chan, S., Zhang, X. and Gabriel, S. (2007) The attenuation of cavity tones using plasma actuators. *AIAA J.* 45 (7), pp. 1525-1538.

Moreau, E. (2007) Airflow control by non-thermal plasma actuators. *J Phys D Appl Phys.* 40 (3), pp. 605-636.

Casalinoa, D., Diozzib, F., Sanninob, R. and Paonessa, A. (2008) Aircraft noise reduction technologies: A bibliographic review. *Aerospace Science and Technology.* 12 (1), pp. 1-17.

Thomas, F.O., Kozlov, A. and Corke, K.C. (2008) Plasma actuators for cylinder flow control and noise reduction. *AIAA J.* 46 (8), pp. 1921–1931.

Huang, X., Chan, S., Zhang, X. and Gabriel, S. (2008) Variable structure model for flow-induced tonal noise control with plasma actuators. *AIAA J.* 46 (1), pp. 241-250.

Kozlov, A.V. and Thomas, F.O. (2009) Active noise control of bluff-body flows using dielectric barrier discharge plasma actuators. *15th AISS/CEAS aeroacoustic Conference.* Miami, Florida, 11-13 May 2009. AIAA-2009-3245.

Boorsma, K., Zhang, X. and Molin, N. (2009) Bluff body noise control using perforated fairings. *AIAA J.* 47 (1), pp. 33-43.

Ma, Z. and Zhang, X., (2009) Numerical Investigation of Broadband Slat Noise Attenuation with Acoustic Liner Treatment. *AIAA J.* 47 (12), pp. 2812-2820.

Orselli, R., Meneghini, J. and Saltara, F. (2009) Two and Three-Dimensional Simulation of Sound Generated by Flow Around a Circular Cylinder. *15th AIAA/CEAS aeroacoustic Conference (30th AIAA aeroacoustic Conference).* Miami, Florida, USA, 11-13 May 2009.

Li, Y., Zhang, X. and Huang X. (2010) The use of plasma actuators for bluff body broadband noise control. *Exp Fluids.* 49 (2), pp. 367–377.

Huang, X., Zhang, X. and Li, Y. (2010) Broadband flow-induced sound control using plasma actuators. *J Sound Vibration.* 329 (13), pp. 2477–2489.

Angland, D., Zhang, X. and Goodyer, M. (2010) The use of blowing flow control to reduce bluff body interaction noise. *AIAA J.* 50 (8), pp. 1670-1684.

Kazeminezhad, M.H., Yeganeh-Bakhtiary, A. and Etemad-Shahid, A. (2010) Numerical investigation of boundary layer effects on vortex shedding frequency and forces acting upon marine pipeline. *Applied Ocean Research.* 32, pp. 460-470.

Dobrzynski, W. (2010) Almost 40 years of airframe noise research: what did we achieve? *Journal of Aircraft.* 47 (2), pp. 353–367.

Li, Y., Smith, M. and Zhang, X. (2012) Measurement and control of aircraft landing gear broadband noise. *Aerospace Science and Technology*. 23 (1), pp. 213-223.

Li, Y., Wang, X. and Zhang, D. (2013) Control strategies for airframe noise reduction. *Chinese Journal of Aeronautics.* 26 (2), pp. 249-260.

Pascioni, K.A., Cattafesta, L.N. and Choudhari, M.M. (2014) An Experimental Investigation of the 30P30N Multi-Element High-Lift Airfoil. *20th AIAA/CEAS aeroacoustic Conference (35th AIAA aeroacoustic Conference).* Atlanta, Georgia, 16-20 June 2014.

Choudhari, M. and Lockard, D.P. (2015) Assessment of Slat Noise Predictions for 30P30N High-Lift Configuration from BANC-III Workshop. *21st AIAA/CEAS aeroacoustic Conference*. Dallas, July 2015.

Soulat, L., Fosso, P, A. and Moreau, S. (2016) A high-order sensitivity method for multi-element high-lift device optimization. *Computers & Fluids.* 124, pp. 105-116.

Li, L., Liu, P., Guo, H., Hou, Y., Geng, X. and Wang, J. (2016) Aeroacoustic measurement of 30P30N high-lift configuration in the test section with Kevlar cloth and perforated plate. *Aerospace Science and Technology.* 90, pp. 590–599.

Jun, T. and Gang, S. (2016) An artificial neural network approach for aerodynamic performance retention in airframe noise reduction design of a 3D swept wing model. *Chinese Journal of Aeronautics.* 29 (5), pp. 1213-1225.

Ashton, N., West, A. and Mendonca, F. (2016) Flow Dynamics Past a 30P30N Three-Element Airfoil Using Improved Delayed Detached-Eddy Simulation. *AIAA J.* 54 (11), pp. 3657-3666.

Gao, J.H., Li, X.D. and Lin, D.K. (2017) Numerical Simulation of the Noise from the 30P30N Highlift Airfoil with Spectral Difference Method. *23rd AIAA/CEAS aeroacoustic Conference*. Denver, Colorado, 5-9 June 2017.

Cai, J.C., Pan, J., Kryzhanovskyi, A. and E, S.J. (2018) A numerical study of transient flow around a cylinder and aerodynamic sound radiation. *Thermophysics and Aeromechanics*. 25, pp. 331–346.

Bertsch, L., Snellen, M., Enghardt, L. and Hillenherms, C. (2019) Aircraft noise generation and assessment: executive summary. *CEAS Aeronautical Journal*. 10, pp. 3–9.

Molin, N. (2019) Airframe noise modeling and prediction. *CEAS Aeronautical Journal*. 10, pp. 11–29.

Khorrami, M. and Fares, E. (2019) Toward noise certification during design: airframe noise simulations for full-scale, complete aircraft. *CEAS Aeronautical Journal*. 10, pp. 31-67.

Pott-Pollenske, M. (2019) Limits and challenges of aircraft retrofitting for noise reduction. *CEAS Aeronautical Journal*. 10, pp. 69-76.

Yamamoto, K., Hayama, K., Kumada, T. and Hayashi, K. (2019) A flight demonstration for airframe noise reduction technology. *CEAS Aeronautical Journal*. 10, pp. 77-92.

Liu, X.W., Thompson, D.J. and Hu, Z.W. (2019) Numerical investigation of aerodynamic noise generated by circular cylinders in cross-flow at Reynolds numbers in the upper subcritical and critical regimes. *International Journal of Aeroacoustics*. 18 (4-5), pp. 470-495.

System identification

Ljung, L. (1987) *SYSTEM IDENTIFICATION: Theory for the User*. London: Prentice-Hall International (UK) limited.

Adaptive control and signal processing

John, G.P. and Dimitris, G.M. (2013) *Digital Signal Processing*. 4th ed. Essex: Pearson New International Edition.

Kuo, S.M. and Lee, B.H. (2006) *Real-Time Digital Signal Processing: Implementations and Applications*. 2nd ed. West Sussex: Wiley.

Active noise control

Lueg, P. Process of Silencing Sound Oscillations, US Patent 2043416, June 9, 1936.

Janocha, H. and Liu, B. (1998) Simulation approach and causality evaluation for an active noise control system. *IEE Proc., Control Theory Appl.* 145 (4), pp. 423–426.

Leitch, R.R. and Tokhi, M.O. (1987) Active noise control systems. *IEE Proceedings A - Physical Science, Measurement and Instrumentation, Management and Education – Reviews.* 134 (6), pp. 525-546.

Kuo, S.M. and Morgn, D.R. (1999) Active noise control: a tutorial review. *Proceedings of the IEEE.* 87 (6), pp. 943-973.

Kuo, S.M., Wu, H.T., Chen, F.K. and Gunnala, M.R. (2004) Saturation effects in active noise control systems. *IEEE Trans. Circuits Syst. I.* 51 (6), pp. 1163–1171.

Raja Ahmad, R.K. and Tokhi, M.O. (2010) Analysis of Geometry Related Constraints of Minimum Effort Active Noise Control System. *JOURNAL OF LOW FREQUENCY NOISE, VIBRATION AND ACTIVE CONTROL.* 29 (2), pp. 111-128.

Peters, R J., Smith, B J. and Hollins, N. *Acoustics and Noise Control.* 3rd ed. UK: Pearson Education Limited.

Sahib, M.A. and Kamil, R. (2011) Comparison of Performance and Computational Complexity of Nonlinear Active Noise Control Algorithms. *ISRN Mechanical Engineering.* 2011, pp. 1-9.

Kajikawa, Y., Gan, W.S. and Kuo, S.M. (2012) Recent advances on active noise control: open issues and innovative applications. *APSIPA Transactions on Signal and Information Processing.* 1 (3), pp. 1-21.

George, N.V. and Panda, G. (2013) Advances in active noise control: A survey, with emphasis on recent nonlinear techniques. *Signal Processing.* 93 (2), pp. 363-377.

Jiang, J.G. and Li, Y. (2018) Review of active noise control techniques with emphasis on sound quality enhancement. *Applied Acoustics.* 136, pp. 139-148.

Luo, L., Bai, Z.L., Zhu, W.Z. and Sun, J.W. (2018) Improved functional link artificial neural network filters for nonlinear active noise control. *Applied Acoustics.* 135, pp. 111-123.

Mondal, K., Das, S., Abu, A.B.H., Hamada, N., Toh, H.T., Das, S. and Faris, W.F. (2018) All-pass filtered x least mean square algorithm for narrowband active noise control. *Applied Acoustics*. 142 (15), pp. 1-10.

Lam, B., Elliott, S., Cheer, J. and Gan, W.S. (2018) Physical limits on the performance of active noise control through open windows. *Applied Acoustics*. 137, pp. 9-17.

Wrona, S., Diego, M.D. and Pawelczyk, M. (2018) Shaping zones of quiet in a large enclosure generated by an active noise control system. *Control Eng Pract.* 80, pp. 1–16.

Iwai, K., Hase, S. and Kajikawa, Y. (2018) Multichannel Feedforward Active Noise Control System with Optimal Reference Microphone Selector Based on Time Difference of Arrival. *Appl. Sci.* 8 (2291), pp. 1-17.

Nunez, I.J.C., Miranda, J.G.O. and Duarte, M.V. (2019) Active noise control in acoustic shutters. *Applied Acoustics.* 152, pp. 41-46.

Zhu, L.P., Yang, T.J., Pan, J., Zhu, M.G. and Li, X.H. (2019) Reweighted adaptive bilinear filters for an active noise control system with a nonlinear secondary path. *Applied Acoustics.* 155, pp. 123-129.

Mazur, K., Wrona, S. and Pawelczyk, M. (2019) Active noise control for a washing machine. *Applied Acoustics.* 146, pp. 89-95.

Le, D.C., Li, D.F. and Zhang, J.S. (2019) M-max partial update leaky bilinear filter-error least mean square algorithm for nonlinear active noise control. *Applied Acoustics.* 156, pp. 158-165.

He, Z.C., Ye, H.H. and Li, E. (2019) An efficient algorithm for nonlinear active noise control of impulsive noise. *Applied Acoustics.* 148, pp. 366-374.

Puri, A., Modal, S.V. and Gupta, K. (2019) Global active control of harmonic noise in a vibro-acoustic cavity using Modal FxLMS algorithm. *Applied Acoustics.* 150, pp. 147-161.

Niu, F., Qiu, X.J. and Zhang, D. (2020) Effects of active noise cancelling headphones on speech recognition. *Applied Acoustics.* 152, 107335.

Meng, H. and Chen, S.M. (2020) A modified adaptive weight-constrained FxLMS algorithm for feedforward active noise control systems. *Applied Acoustics.* 164, 107227.

Patel, V. and George, N.V. (2020) Multi-channel spline adaptive filters for non-linear active noise control. *Applied Acoustics.* 161, 107142.

Guo, J.F., Yang, F.R. and Yang, Y. (2020) Convergence analysis of the conventional filtered-x affine projection algorithm for active noise control. *Signal Processing.* 170, 107437.

Wang, Y.S., Guo, H., Li, Y.R., Liu, N.N. and Yang, C. (2020) Active control for vehicle interior noise based on DWT-FxLMS algorithm using a piezoelectric feedback system. *Applied Acoustics.* 167, 107409.

Soft engineering technique

Zadeh, L.A. (1965) Fuzzy Sets. *Information and Control.* 8, pp. 338-353.

Zadeh, L.A. (1994) Fuzzy Logic, Neural Networks, and Soft Computing. *Fuzzy Systems.* 37 (3), pp. 77-84.

Takagi, T. and Sugeno, M. (1985) Fuzzy Identification of Systems and Its Applications to Modeling and Control. *IEEE Transactions on Systems, Man, and Cybernetics.* 15 (1), pp. 116-132.

Jang, J-S.R. (1993) ANFIS: Adaptive-Network-Based Fuzzy Inference System. *IEEE TRANSACTIONS ON SYSTEMS, MAN, AND CYBERNETICS.* 23 (3), pp. 665-685.

Jang, J-S.R. and Sun, C.T. (1995) Neuro-Fuzzy Modeling and Control. *Proceedings of the IEEE.* 83 (3), pp. 378-406.

Mitra, S. and Hayashi, Y. (2000) Neuro-fuzzy rule generation: survey in soft computing framework. *IEEE Trans. Neural Networks.* 11 (3), pp. 748-768.

Kasabov, N.K. and Song, Q. (2002) DENFIS: dynamic evolving neural-fuzzy inference system and its application for time-series prediction. *IEEE Trans. Fuzzy Syst.* 10 (2), pp. 144-154.

Chen, M.Y. (2013) A hybrid ANFIS model for business failure prediction utilizing particle swarm optimization and subtractive clustering. *Inf. Sci.* 220, pp. 180-195.

Tokhi, M.O. and Azad, A.K.M. (2017) *Flexible Robot Manipulators - Modelling, Simulation and Control.* 2nd ed. London: Institution of Engineering and Technology.

Zhao J.B., Wang T., Zhang G., He Z. and Mario J. Ṕerez-Jiḿenez. (2014) Fault diagnosis of electric power systems based on fuzzy reasoning spiking neural p systems. *IEEE Trans. Power Syst.,* 30 (3), pp. 1182-1194.

Kurczyk, S. and Pawelczyk, M. (2014) Active Noise Control Using a Fuzzy Inference System Without Secondary Path Modelling. *Archives of Acoustics.* 39 (2), pp. 243-248.

Dave, V.S. and Dutta, K. (2014) Neural network based models for software effort estimation: a review. *Artificial Intelligence Review.* 42 (2), pp. 295-307.

Shihabudheen, K.V. and Pillai, G.N. (2017) Regularized extreme learning adaptive neuro-fuzzy algorithm for regression and classification. *Knowledge-Based Systems.* 127, pp. 100-113.

Shihabudheen, K.V. and Pillai, G.N. (2018) Recent advances in neuro-fuzzy system: A survey. *Knowledge-Based Systems.* 156, pp. 136-162.

Abbas, K.M. (2018) FNDSB: A fuzzy-neuro decision support system for back pain diagnosis. *Cogn. Syst. Res.* 52, pp. 691-700.

Abiodum, O.I., Jantan, A., Omolara, A.E., Dada, K.V., Mohamd, N.A. and Arshad, H. (2018) State-of-the-art in artificial neural network applications: A survey. *Heliyon.* 4, pp. 1-41.

Rajab, S. (2019) Handling interpretability issues in ANFIS using rule base simplification and constrained learning. *Fuzzy Sets and Systems.* 368 (1), pp. 36-58.

Baraka, A. and Panoutsos, G. (2019) Long-term learning for type-2 neural-fuzzy systems. *Fuzzy Sets and Systems.* 368 (1), pp. 59-81.

Ren, W.B., Wu, K.Z., Gu, Q.S. and Hu, Y.G. (2020) Intelligent decision making for service providers selection in maintenance service network: An adaptive fuzzy-neuro approach. *Knowledge-Based Systems.* 190, 105263.

Particle swarm optimization algorithm

Kennedy, J. and Eberhart, R.C. (1995) Particle swarm optimization, in: *Proceedings of the IEEE International Conference on Neural Networks*. 1, pp. 1942–1948.

Shi, Y. and Eberhart, R. (2002) A modified particle swarm optimizer. *1998 IEEE International Conference on Evolutionary Computation Proceedings. IEEE World Congress on Computational Intelligence (Cat. No.98TH8360.* Anchorage, AK, USA, USA, 4-9 May. pp. 69-73.

Russo, F. and Sicuranza, G.L. (2007) Accuracy and performance evaluation in the genetic optimization of nonlinear systems for active noise control. *IEEE Transactions on Instrumentation and Measurement.* 56 (4), pp. 1443-1450.

Karaboga, D. and Akay, B. (2009) A comparative study of Artificial Bee Colony algorithm. *Applied Mathematics and Computation*. 214 (1), pp. 108-132.

Rout, N.K., Das, D.P. and Panda, G. (2012) Particle swarm optimization based active noise control algorithm without secondary path identification. *IEEE Transactions on Instrumentation and Measurement*. 61 (2), pp. 554-563.

Zhang, Y.D., Wang, S.H. and Ji, G.L. (2015) A Comprehensive Survey on Particle Swarm Optimization Algorithm and Its Applications. *Mathematical Problems in Engineering*. 2015, pp. 1-38.

Wang, D.S., Tan, D.P. and Liu, L. (2018) Particle swarm optimization algorithm: an overview. *Soft Comput.* 22, pp. 387–408.

Appendix

A. Locus of system components in the three-dimensional Euclidean space

This section expands the locus of system components from two-dimensional to three-dimensional Euclidean space. Assume the primary source as the original point and coordinates of the secondary source, the detector and the receiver are (u, v, w), (x_1, y_1, z_1) and (x_2, y_2, z_2). Figure A.1 presents coordinates of system components in a three-dimensional Cartesian coordinate system based on the physical process of active noise control.
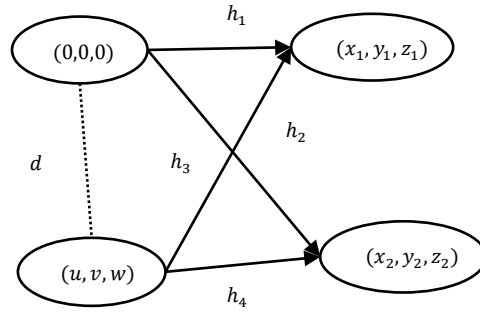
Figure A.1. System components in a three-dimensional Cartesian coordinate system

To analyse conveniently, we define four vector quantities as follows:

$$\begin{cases} \overrightarrow{h_1} = (x_1)\vec{m} + (y_1)\vec{n} + (z_1)\vec{k} \\ \overrightarrow{h_2} = (x_1 - u)\vec{m} + (y_1 - v)\vec{n} + (z_1 - w)\vec{k} \\ \overrightarrow{h_3} = (x_2)\vec{m} + (y_2)\vec{n} + (z_2)\vec{k} \\ \overrightarrow{h_4} = (x_2 - u)\vec{m} + (y_2 - v)\vec{n} + (z_2 - w)\vec{k} \end{cases} \tag{1}$$

where $\vec{m}$, $\vec{n}$ and $\vec{k}$ are standard vectors in the positive x, y and z axis respectively.

Assume the physical separation between two sources is d and d is known, one can obtain that:

$$\sqrt{u^2 + v^2 + w^2} = d \tag{2}$$

Where, the range of u, v and w is $(0, d)$.

Remark 1: The physical separation between two sources in the feedforward ANC system determines the phase delay and the value of d should be determined according to the practical problems.

Remark 2: All discussions presented in this part focus on the condition that both detector and receiver locate in the right side of the secondary source, which means coordinates of the detector and the receiver are positive.

The distance ratio is greater than one

Consider definition in section 4.3 and Eq. (1), one can obtain that:

$$\frac{\sqrt{x_2{}^2 + y_2{}^2 + (z_2)^2}}{\sqrt{(x_2 - u)^2 + (y_2 - v)^2 + (z_2 - w)^2}} = a \tag{3}$$

$$\frac{\sqrt{x_1{}^2 + y_1{}^2 + (z_1)^2}}{\sqrt{(x_1 - u)^2 + (y_1 - v)^2 + (z_1 - w)^2}} = b \tag{4}$$

The distance ratio is greater than one can be further classified as three subsections, $2 > a > b > 1$, $2 > a > b \,\&\, b = 1$ and $2b > a > 1 > b > \frac{1}{2}$.

$\boldsymbol{2 > a > b > 1}$: Apply the condition in Eq. (3) and Eq. (4), we can obtain that:

$$\left(x_2 - \frac{a^2 u}{a^2 - 1}\right)^2 + \left(y_2 - \frac{a^2 v}{a^2 - 1}\right)^2 + \left(z_2 - \frac{a^2 w}{a^2 - 1}\right)^2 = \frac{a^2}{(a^2 - 1)^2} d^2 \tag{5}$$

$$\left(x_1 - \frac{b^2 u}{b^2 - 1}\right)^2 + \left(y_2 - \frac{b^2 v}{b^2 - 1}\right)^2 + \left(z_1 - \frac{b^2 w}{b^2 - 1}\right)^2 = \frac{b^2}{(b^2 - 1)^2} d^2 \tag{6}$$

Eq. (5) and Eq. (6) are two sphere equations.

Assume symbol A and B are the central point of each sphere and coordinates of A and B are $(\frac{a^2 u}{a^2 - 1}, \frac{a^2 v}{a^2 - 1}, \frac{a^2 w}{a^2 - 1})$ and $(\frac{b^2 u}{b^2 - 1}, \frac{b^2 v}{b^2 - 1}, \frac{b^2 w}{b^2 - 1})$ respectively.

Now, to identify the relationship between these two loci of microphone, we define two vector quantities as:

$$\begin{cases} \overrightarrow{OA} = \left(\dfrac{a^2 u}{a^2 - 1}, \dfrac{a^2 v}{a^2 - 1}, \dfrac{a^2 w}{a^2 - 1}\right) \\[2mm] \overrightarrow{OB} = \left(\dfrac{b^2 u}{b^2 - 1}, \dfrac{b^2 v}{b^2 - 1}, \dfrac{b^2 w}{b^2 - 1}\right) \end{cases} \tag{7}$$

Repeat similar procedures provided in section 4.3.1, we can obtain the relationship between these two loci (see Figure A.2).
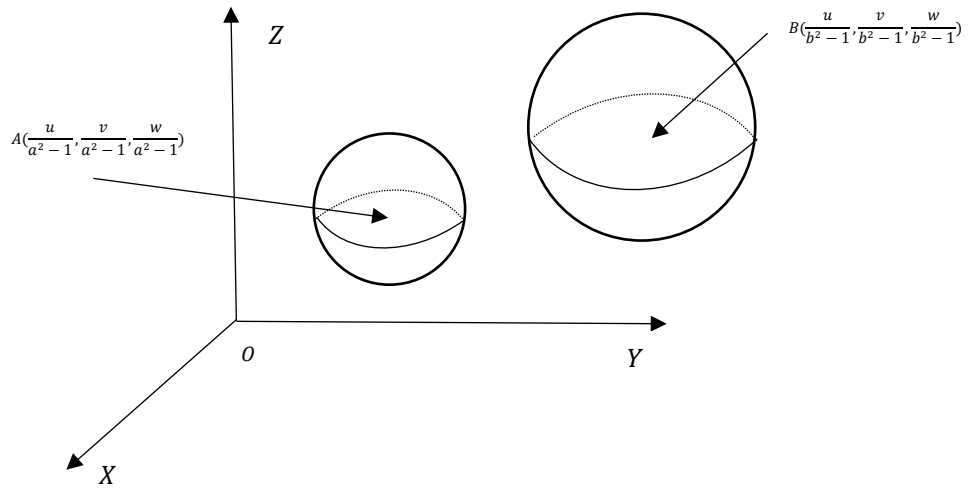
Figure A.2. Relationship between two loci ($2 > a > b > 1$)

$2 > a > b$ & $b = 1$: Substitute $b = 1$ in Eq. (4), we obtain that:

$$\frac{\sqrt{x_1{}^2 + y_1{}^2 + (z_1)^2}}{\sqrt{(x_1 - u)^2 + (y_1 - v)^2 + (z_1 - w)^2}} = 1 \tag{8}$$

Simplify Eq. (8), then we can obtain that:

$$\frac{2u}{d^2} x_1 + \frac{2v}{d^2} y_1 + \frac{2w}{d^2} z_1 = 1 \tag{9}$$

Eq. (9) describes a plane in three-dimensional space and coordinates of intersects points located within

the positive octant are $(\frac{d^2}{2u}, 0, 0)$, $(0, \frac{d^2}{2v}, 0)$ and $(0, 0, \frac{d^2}{2w})$ respectively (see Figure A.3).
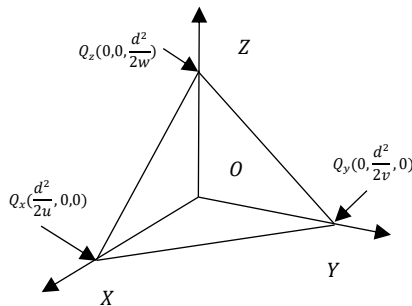
Figure A.3. Locus of the detector ($b = 1$)

Remark 4: Under this condition, the locus of the detector greatly depends on the coordinate of the secondary source.

Consider the range of u, v and w is $(0, d)$, then we can obtain that:

$$\begin{cases} \dfrac{d^2}{2u} > \dfrac{d}{2} \\ \dfrac{d^2}{2v} > \dfrac{d}{2} \\ \dfrac{d^2}{2w} > \dfrac{d}{2} \end{cases} \tag{10}$$

Assume that A' is the nearest point of the locus described in Eq. (10) with respect to O in the positive octant and the distance between A' and O is:

$$|\overrightarrow{OA'}| = \frac{ad}{a^2 - 1} - \frac{d}{a^2 - 1} = \frac{d}{a + 1} \tag{11}$$

Apply $1 < a < 2$ in Eq. (11), we can obtain that:

$$\frac{d}{3} < |\overrightarrow{OA'}| < \frac{d}{2} \tag{12}$$

Combine Eq. (10) and Eq. (12), we can find that the relationships between these two loci are uncertainty and greatly depends on the coordinate of the secondary source.

$2b > a > 1 > b > \frac{1}{2}$: Apply $b < 1$ in Eq. (4), the locus equation of the receiver is:

$$\left(x_1 + \frac{b^2 u}{1 - b^2} \right)^2 + \left(y_1 + \frac{b^2 v}{1 - b^2} \right)^2 + \left(z_1 + \frac{b^2 w}{1 - b^2} \right)^2 = \frac{b^2}{(1 - b^2)^2} d^2 \tag{13}$$

Eq. (13) is a sphere equation and we assume the centre point as B_1 and the coordinate is $(-\frac{b^2 u}{1 - b^2}, -\frac{b^2 v}{1 - b^2}, -\frac{b^2 w}{1 - b^2})$.

Consider $1 > b > \frac{1}{2}$, B_1 is located within the negative octant and Figure 4 presents the locus of the detector.
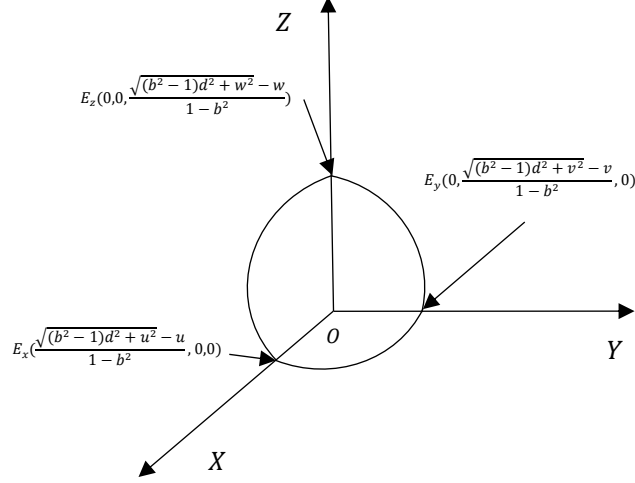
Figure A.4. The locus of the detector $(1 > b > \frac{1}{2})$

To analyse conveniently, we select another point $B_1{}'$, which is the farthest point on the sphere with respect to O in the positive octant and the distance between $B_1{}'$ and O is:

$$\left|\overrightarrow{OB_1{}'}\right| = \frac{bd}{1 - b^2} - \frac{d}{1 - b} = \frac{d}{b + 1} \tag{14}$$

Apply $a > b$ in Eq. (11) and Eq. (14), it can find that $\left|\overrightarrow{OA'}\right| < \left|\overrightarrow{OB_1{}'}\right|$ and these two loci have intersection parts and also greatly depends on the coordinate of the secondary source.

Remark 5: In summary, when the distance ratio of the detector is no bigger than 1, the relationship between two loci greatly depends on the location of the secondary source.

The distance ratio is one

In this case, we can obtain that $a = b > 1$ and both sensors satisfy the same locus equation, it is specified as:

$$\left(x - \frac{u}{c^2 - 1}\right)^2 + \left(y - \frac{v}{c^2 - 1}\right)^2 + \left(z - \frac{w}{c^2 - 1}\right)^2 = \frac{c^2}{(c^2 - 1)^2}d^2 \tag{15}$$

Where $c = a = b$ and we present the locus in Figure A.5.

121
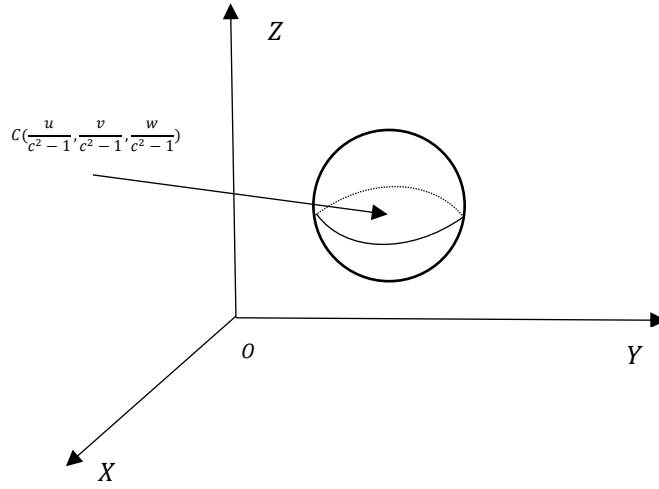
Figure A.5. Loci of two sensors ($a = b > 1$)

Remark 6: Although both sensors have the same locus equation on this scene, their positions cannot be overlapped as we only consider the feedforward ANC system in this paper.

The distance ratio is smaller than one

Under this condition, the relationship between two parameters is:

$$2 > b > a > 1 \tag{16}$$

Repeat similar procedures in section 4.3.3, we provide the relationship between two loci in Figure A.6.
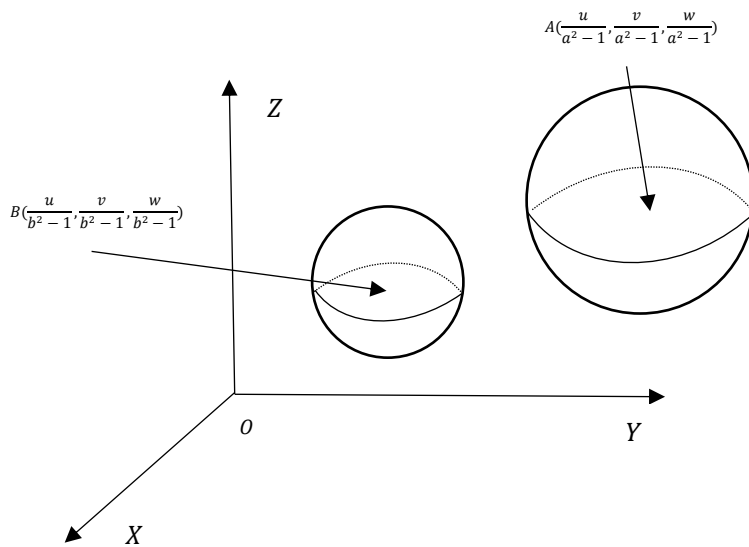
Figure A.6. Relationship between two loci ($2 > b > a > 1$)

B. A single input, multi-output (SIMO) ANC system description

In practice, sources of noise can broadly be classified as compact or distributed. A compact source of noise is theoretically modelled as a point source with contours of equal pressure levels forming spherical surfaces around the source and it is an important source of the landing gear noise (see Chapter 5). To cancel the compact source of noise, a single detector and a single receiver is generally sufficient to obtain the required signal information needed to generate the cancelling signal and the structure of the SISO ANC system is proposed in section 4.1. By contrast, a distributed source of noise can be modelled as a set of point sources distributed around the surface of the source and it is an important component of the slat noise. To cancel the distributed source of noise, a multiple set of detectors or receivers will be required, which leads to the realization of a multi-input or multi-output control structure. In this section, we use a simple single input, multi-output (SIMO) adaptive ANC system to illustrate.

Based on Figure 4.1.1, Figure B.1 presents a schematic diagram of a simple adaptive SIMO ANC system.
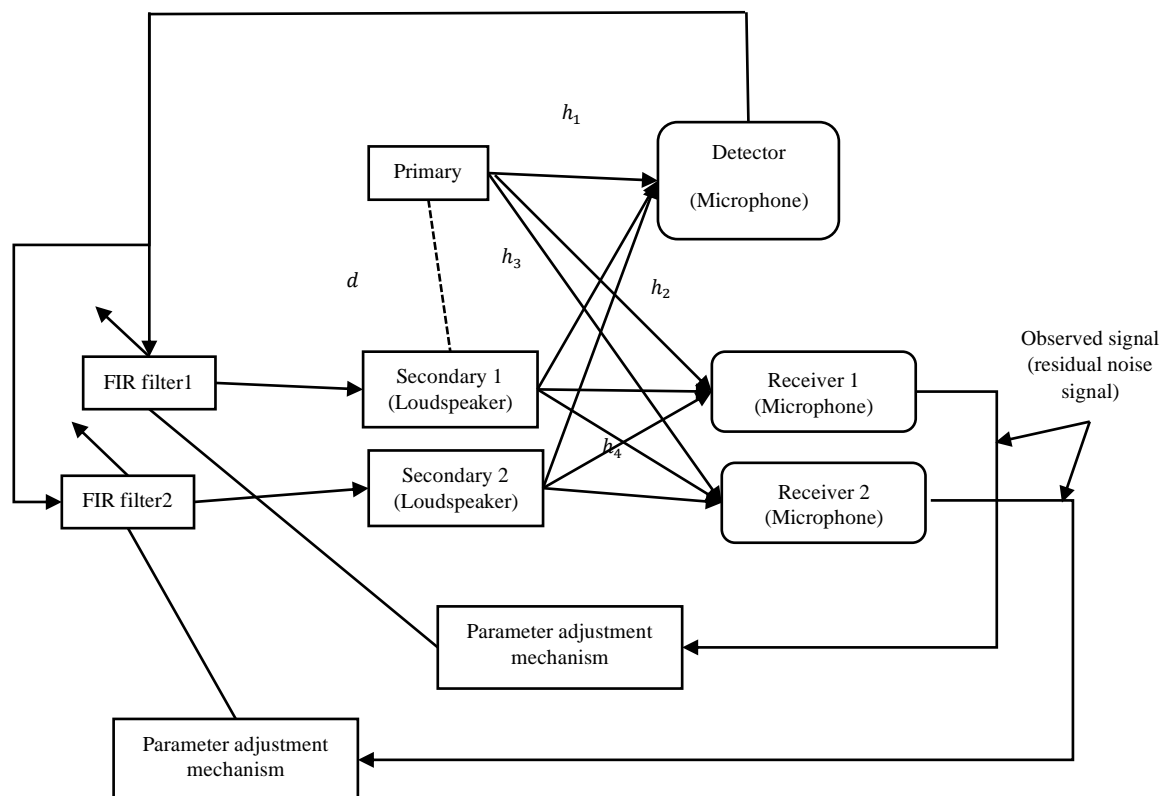
Figure B.1. Schematic diagram of the simple adaptive SIMO feedforward ANC system

All distances marked in Figure 1 are in the form of matrix and we will explain in the following section. In comparison with the SIMO adaptive ANC system (presented in Figure 4.1.1), the simple SIMO adaptive ANC system (presented in Figure 4.6.1) has two adaptive filters, two secondary sources, and two receivers.

Remark 1: In practice, there are other types of SIMO adaptive ANC system and this section aims to explain the difference of the SIMO adaptive ANC system in comparison with the SISO adaptive ANC system.

The expressions of $H_1(z)$, $H_2(z)$, $H_3(z)$ and $H_4(z)$ are specified as:

$$
\begin{cases}
H_1(z) = \dfrac{constant}{h_1} e^{-\frac{\ln Z}{T}t_1} = \dfrac{constant}{h_1} e^{-F_s \ln Z t_1} \\[2mm]
H_2(z) = \left[\dfrac{constant}{h_{21}} e^{-F_s \ln Z t_{21}}, \dfrac{constant}{h_{221}} e^{-F_s \ln Z t_{22}} \right]^T \\[2mm]
H_3(z) = \left[\dfrac{constant}{h_{31}} e^{-F_s \ln Z t_{31}}, \dfrac{constant}{h_{32}} e^{-F_s \ln Z t_{32}} \right] \\[2mm]
H_4(z) = \begin{bmatrix} \dfrac{constant}{h_{411}} e^{-F_s \ln Z t_{411}}, \dfrac{constant}{h_{412}} e^{-F_s \ln Z t_{412}} \\[2mm] \dfrac{constant}{h_{421}} e^{-F_s \ln Z t_{421}}, \dfrac{constant}{h_{422}} e^{-F_s \ln Z t_{422}} \end{bmatrix}
\end{cases}
\tag{1}
$$

Where:

h_{21}: the physical distance between secondary source 1 and detector

h_{22}: the physical distance between secondary source 2 and detector

h_{31}: the physical distance between primary source and receiver 1

h_{32}: the physical distance between primary source and receiver 2

h_{411}: the physical distance between secondary source 1 and receiver 1

h_{412}: the physical distance between secondary source 1 and receiver 2

h_{421}: the physical distance between secondary source 2 and receiver 1

h_{422}: the physical distance between secondary source 2 and receiver 2

Remark 2: In practice, the constant value may be different from each other and we need to adjust it based on the practical experiment.

The procedures of obtaining the K are same as the procedures in section 4.1.

The $\dfrac{H_4(z)\, H_1(z)}{H_3(z)\, H_2(z)}$ can be expressed as:

$$
\frac{H_4(z)\, H_1(z)}{H_3(z)\, H_2(z)} = \frac{\begin{bmatrix} \dfrac{constant}{h_1} e^{-F_s \ln Z t_1} \dfrac{constant}{h_{411}} e^{-F_s \ln Z t_{411}}, \dfrac{constant}{h_1} e^{-F_s \ln Z t_1} \dfrac{constant}{h_{412}} e^{-F_s \ln Z t_{412}} \\[2mm] \dfrac{constant}{h_1} e^{-F_s \ln Z t_1} \dfrac{constant}{h_{421}} e^{-F_s \ln Z t_{421}}, \dfrac{constant}{h_1} e^{-F_s \ln Z t_1} \dfrac{constant}{h_{422}} e^{-F_s \ln Z t_{422}} \end{bmatrix}}{\begin{bmatrix} \dfrac{constant}{h_{21}} e^{-F_s \ln Z t_{21}} \dfrac{constant}{h_{31}} e^{-F_s \ln Z t_{31}}, \dfrac{constant}{h_{21}} e^{-F_s \ln Z t_{21}} \dfrac{constant}{h_{32}} e^{-F_s \ln Z t_{32}} \\[2mm] \dfrac{constant}{h_{22}} e^{-F_s \ln Z t_{22}} \dfrac{constant}{h_{31}} e^{-F_s \ln Z t_{31}}, \dfrac{constant}{h_{22}} e^{-F_s \ln Z t_{22}} \dfrac{constant}{h_{32}} e^{-F_s \ln Z t_{32}} \end{bmatrix}}
\tag{2}
$$

Eq. (4.6.2) reflects that the expression of $\frac{H_4(z)}{H_3(z)}\frac{H_1(z)}{H_2(z)}$ is complicated, therefore, we only consider the condition that $\frac{H_4(z)}{H_3(z)}\frac{H_1(z)}{H_2(z)} = 1$, which is specified as:

$$|H_1(z)H_4(z)| = |H_2(z)H_3(z)| \tag{3}$$

Combine Eq. (4.6.2) and Eq. (4.6.3), one can obtain that:

$$\begin{bmatrix} \dfrac{1}{h_1}\dfrac{1}{h_{411}}, \dfrac{1}{h_1}\dfrac{1}{h_{412}} \\[2mm] \dfrac{1}{h_1}\dfrac{1}{h_{421}}, \dfrac{1}{h_1}\dfrac{1}{h_{422}} \end{bmatrix} = \begin{vmatrix} \dfrac{1}{h_{21}}\dfrac{1}{h_{31}}, \dfrac{1}{h_{21}}\dfrac{1}{h_{32}} \\[2mm] \dfrac{1}{h_{22}}\dfrac{1}{h_{31}}, \dfrac{1}{h_{22}}\dfrac{1}{h_{32}} \end{vmatrix} \tag{4}$$

According to the property of matrix, one can obtain that:

$$\begin{cases} h_1 h_{411} = h_{21}h_{31} \\ h_1 h_{412} = h_{21}h_{32} \\ h_1 h_{421} = h_{22}h_{31} \\ h_1 h_{422} = h_{22}h_{32} \end{cases} \tag{5}$$

Then, we can obtain that:

$$\frac{h_{411}}{h_{412}} = \frac{h_{421}}{h_{422}} = \frac{h_{31}}{h_{32}} = \frac{h_{21}}{h_{22}} \tag{6}$$

Now, we consider the number of output signal is M, then we can obtain the frequency-domain expressions of the acoustic path as:

$$\begin{cases} H_1(z) = \dfrac{constant}{h_1}e^{-\frac{\ln Z}{T}t_1} = \dfrac{constant}{h_1}e^{-F_s \ln Z t_1} \\[3mm] H_2(z) = \left[\dfrac{constant}{h_{21}}e^{-F_s \ln Z t_{21}}, \dots, \dfrac{constant}{h_{2m}}e^{-F_s \ln Z t_{2m}}\right]^T \\[3mm] H_3(z) = \left[\dfrac{constant}{h_{31}}e^{-F_s \ln Z t_{31}}, \dots, \dfrac{constant}{h_{3m}}e^{-F_s \ln Z t_{3m}}\right] \quad ,where\ m = 1, \dots, M \\[3mm] H_4(z) = \begin{bmatrix} \dfrac{constant}{h_{411}}e^{-F_s \ln Z t_{411}} & \cdots & \dfrac{constant}{h_{41m}}e^{-F_s \ln Z t_{41m}} \\[2mm] \vdots & \ddots & \vdots \\[2mm] \dfrac{constant}{h_{4m1}}e^{-F_s \ln Z t_{4m1}} & \cdots & \dfrac{constant}{h_{4mm}}e^{-F_s \ln Z t_{4mm}} \end{bmatrix} \end{cases} \tag{7}$$

The $\frac{H_4(z)}{H_3(z)}\frac{H_1(z)}{H_2(z)}$ can be expressed as:

$$\frac{H_4(z)}{H_3(z)}\frac{H_1(z)}{H_2(z)}$$

$$= \frac{\begin{bmatrix} \frac{constant}{h_1}e^{-F_s\ln Zt_1}\frac{constant}{h_{411}}e^{-F_s\ln Zt_{411}} & \cdots & \frac{constant}{h_1}e^{-F_s\ln Zt_1}\frac{constant}{h_{41m}}e^{-F_s\ln Zt_{41m}} \\ \vdots & \ddots & \vdots \\ \frac{constant}{h_1}e^{-F_s\ln Zt_1}\frac{constant}{h_{4m1}}e^{-F_s\ln Zt_{4m1}} & \cdots & \frac{constant}{h_1}e^{-F_s\ln Zt_1}\frac{constant}{h_{4mm}}e^{-F_s\ln Zt_{4mm}} \end{bmatrix}}{\begin{bmatrix} \frac{constant}{h_{21}}e^{-F_s\ln Zt_{21}}\frac{constant}{h_{31}}e^{-F_s\ln Zt_{31}} & \cdots & \frac{constant}{h_{21}}e^{-F_s\ln Zt_{21}}\frac{constant}{h_{3m}}e^{-F_s\ln Zt_{3m}} \\ \vdots & \ddots & \vdots \\ \frac{constant}{h_{2m}}e^{-F_s\ln Zt_{2m}}\frac{constant}{h_{31}}e^{-F_s\ln Zt_{31}} & \cdots & \frac{constant}{h_{21}}e^{-F_s\ln Zt_{2m}}\frac{constant}{h_{31}}e^{-F_s\ln Zt_{3m}} \end{bmatrix}} \qquad (8)$$

Then, we can obtain that:

$$\frac{h_{411}}{h_{21}} = \cdots = \frac{h_{4m1}}{h_{2m}} \qquad (9)$$

$$\frac{h_{411}}{h_{31}} = \cdots = \frac{h_{41m}}{h_{3m}} \qquad (10)$$

C. Two-dimensional 30P30N slat noise prediction and cancellation

The slat noise prediction is a challenging problem because of the complex physical phenomenon in the slat cove area. The Benchmark Problems for Airframe Noise Computations (BANC) series workshops continuously focusing on the research about the slat noise prediction. This case study is a trial to predict the slat noise of the modified (MD) 30P30N[46] following the procedures and tips in published documents and then use the proposed ANC system to cancel the noise.

Firstly, we introduce the physical configuration of MD30P30N (see Figure C.1)

Figure C.1. MD 30P30N three-element model geometry. (Khorrami et al., 2004; Murayama et al., 2014; Choudhari and Lockard, 2015)

The well-known MD 30P30N three-element model geometry configuration is designed by McDonnell-Douglas (now Boeing), corresponds to slat and flap deflections of 30 degrees each. The chord length of this model is 0.457m and the slat chord and the flap chord are 15% and 30% of the stowed chord, respectively. (Choudhari and Lockard, 2015). The Mach number is 0.17 and the Reynolds number based on the chord length is 1.7×10^6.

Secondly, consider the complex phenomenon at the slat cove area and potential problems of mesh generation for the MD30P30N model, we try to isolate the slat component to analyse. MD 30P30N slat part data can be obtained from UIUC Airfoil Database website (UIUC, 2016) and import it into the Excel software.

We firstly try the ANSYS mesh.

---

[46] The widely used model for slat noise prediction on BANC workshops.
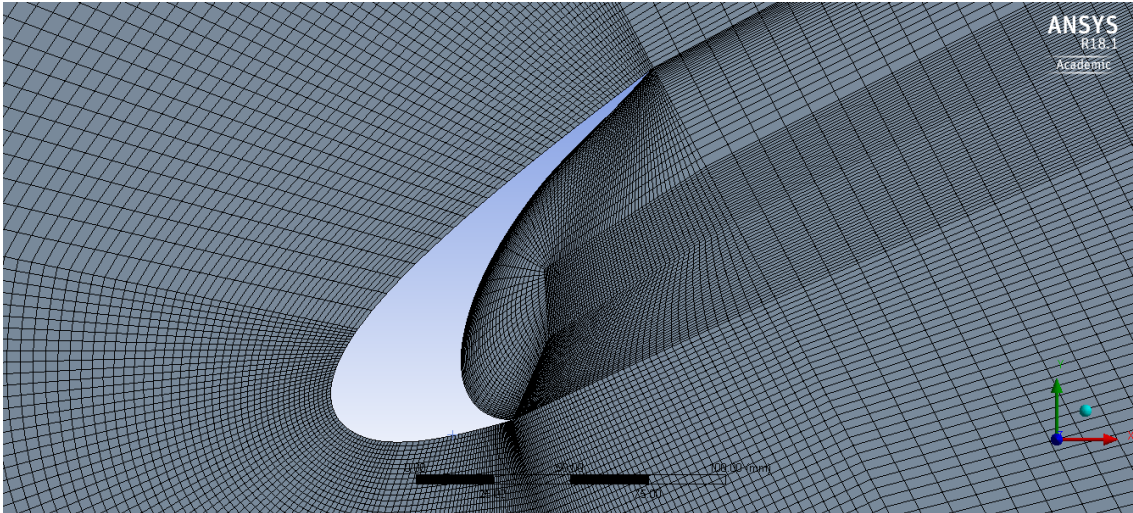
Figure C.2. Mesh for slat part of the MD 30P30N

Figure C.2 reflects that the mesh quality is not good because primarily mesh is not smoothing enough, large jumps across the sub-domain. Therefore, we decide to use ICEM software as the substitute for mesh generation and the procedures are summarized as follows.

Step 1: Data input

Import the data file into ICEM and follow the procedure: File>Imported Geometry> Formatted Point Data to open the data file[47].
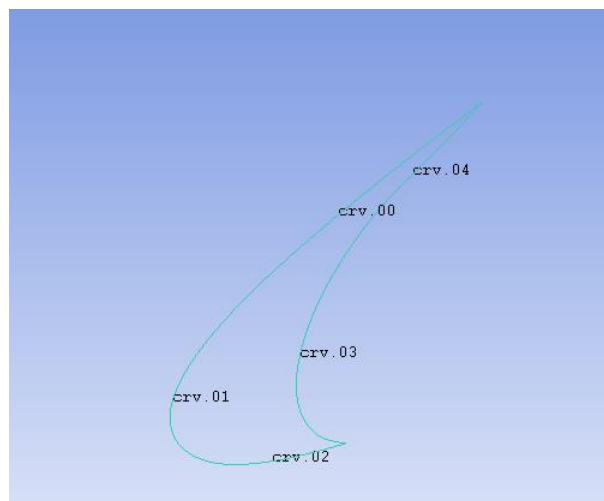
Figure C.3. Name for subset of slat curve

Step 2: Blocking

---

[47] To block the geometry conveniently, it is better to import data only.

From the perspective of the trailing edge, the slat geometry is 'symmetry'. In ICEM, the software will match edge to geometry automatically and it will cause a large error when using the line to match the curve, therefore, the line part and the curve part should be matched separately.
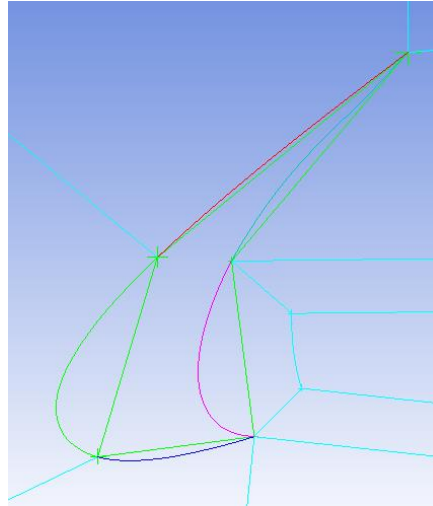
Figure C.4. Initial blocking strategy[48]

Step 3: Domain shape

Consider the shape of slat part, we try the O-mesh first.
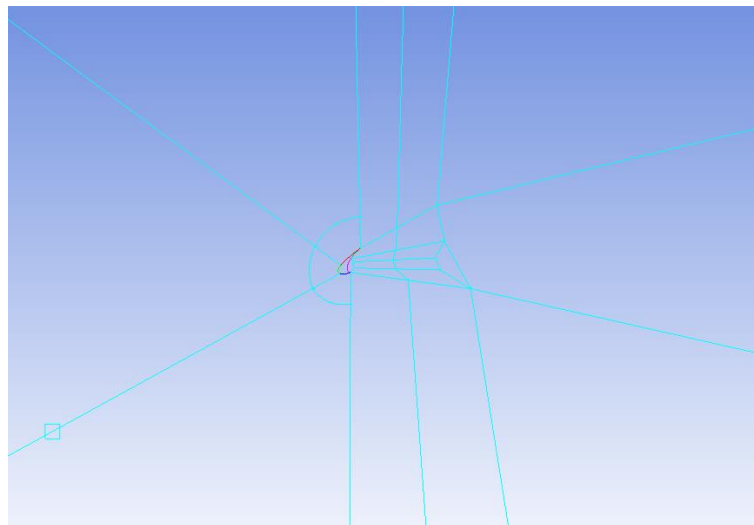
Figure C.5. O-mesh

It reveals that O-mesh is not suitable for slat part as in ICEM because the edge is line not curve, which conflicts with the initial thinking of using the O-type curve to match slat curve.

Then, we change to the H-mesh (i.e. Rectangular mesh).

---

[48] Here, it is important to check any blue line around slat, which definitely will cause failure for transform.
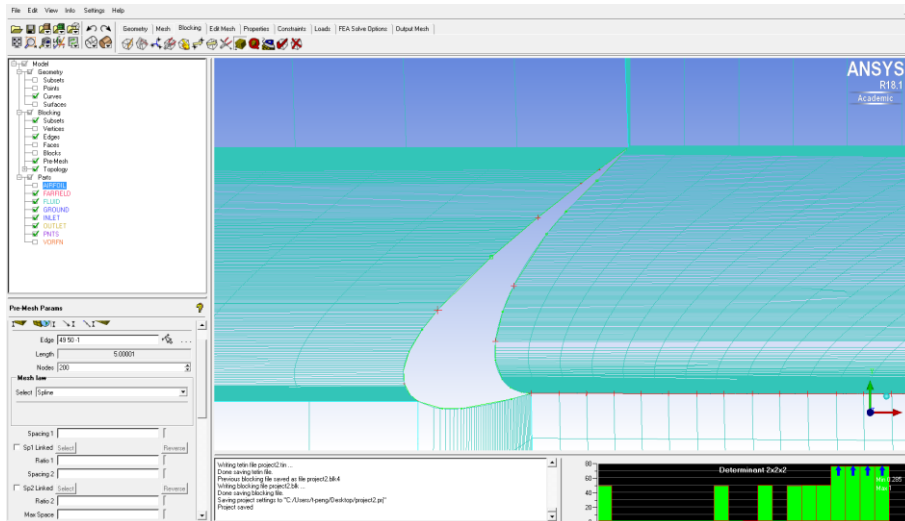
Figure C.6. H-mesh and quality check

Although slat cove part is well resolved but overall mesh quality is awful.

Finally, we choose the C-mesh as the potential optimal mesh type.
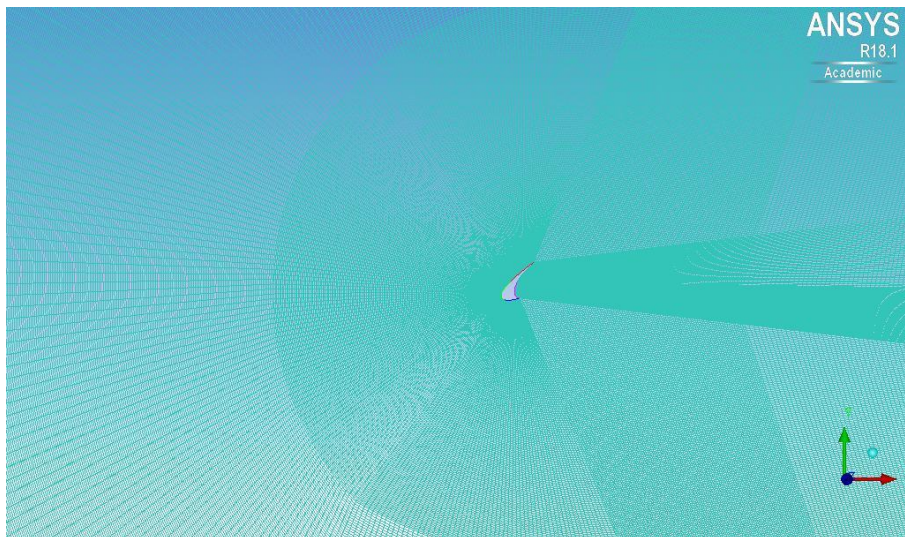
Figure C.7. Mesh

Mesh quality in Figure C.7 is good, however, there are still two problems existed. Firstly, the overall mesh is not smooth enough reflecting the interfaces between two adjacent blocks have not matched better. This might lead to jump in pressure coefficient calculation and will affect lift coefficient calculation. Secondly, Slat broadband noise generated due to the interaction between turbulent shear layer from slat trailing edge and main part leading edge. It is clear that these two sensitive parts, leading edge and trailing edge, have not resolved very well.

To solve the noise prediction at the slat leading-edge and trailing-edge parts, we amend the topology and present it in Figure C.8.
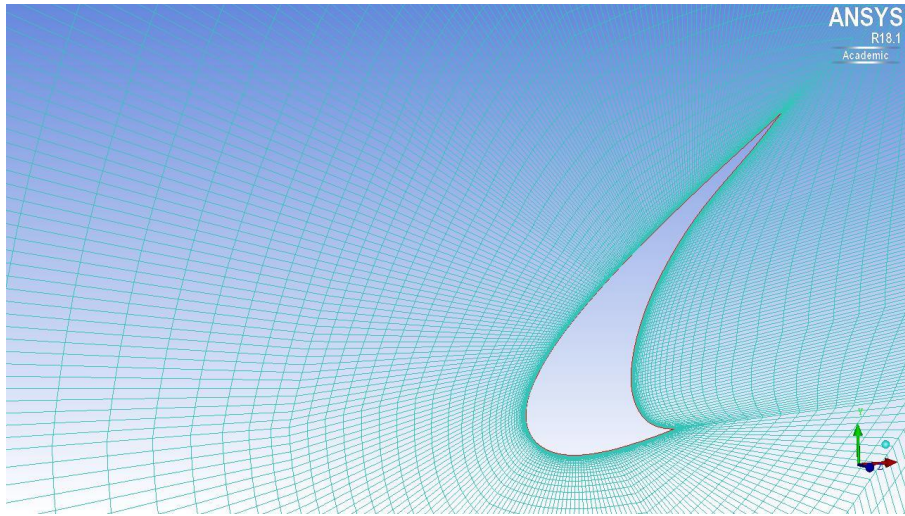
Figure C.8. Mesh

There are 62,000 points in this domain, 360 points for the slat part and y^+ value equals to one.

Based on literature review (Khorrami et al., 2004; Lockard and Choudhari, 2009), the two-equation SST $k - \omega$ method is selected as the turbulence model and the relevant numerical scheme setting is presented in Figure C.9.
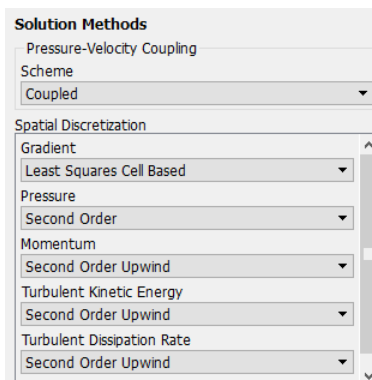
Figure C.9. Numerical scheme setting

Figure C.10 presents the contour Figure of the velocity magnitude.
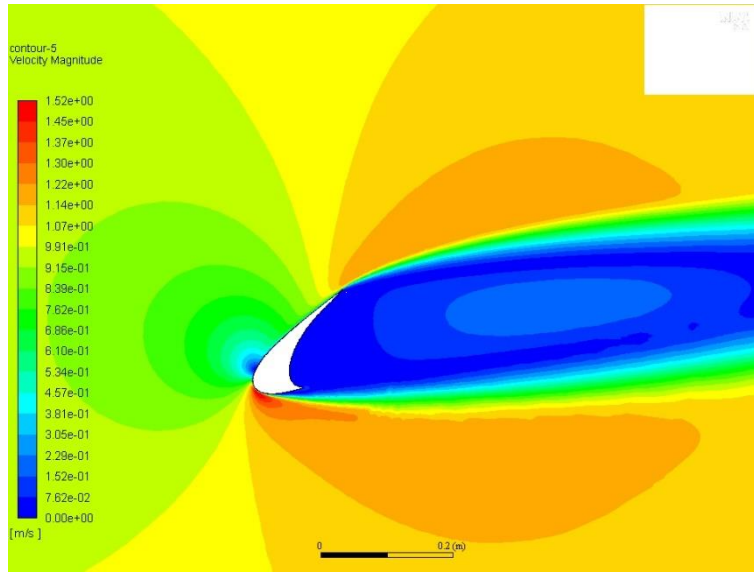
Figure C.10. Velocity magnitude for the slat part.

It is clear that high negative velocities occurring in the slat cove part and the bubble is too huge to affect the accuracy of prediction results. Meanwhile, the flow separation and reattachment points are not correct. Therefore, using single slat foil to predict slat noise is impossible but this case reflects the complex phenomenon in the slat cove area and it provides several experiences for the topology of the entire MD 30P30N.

Now, we decide to choose the entire MD30P30N to predict the slat noise. Figure C.11 presents the topology after several trial and errors.
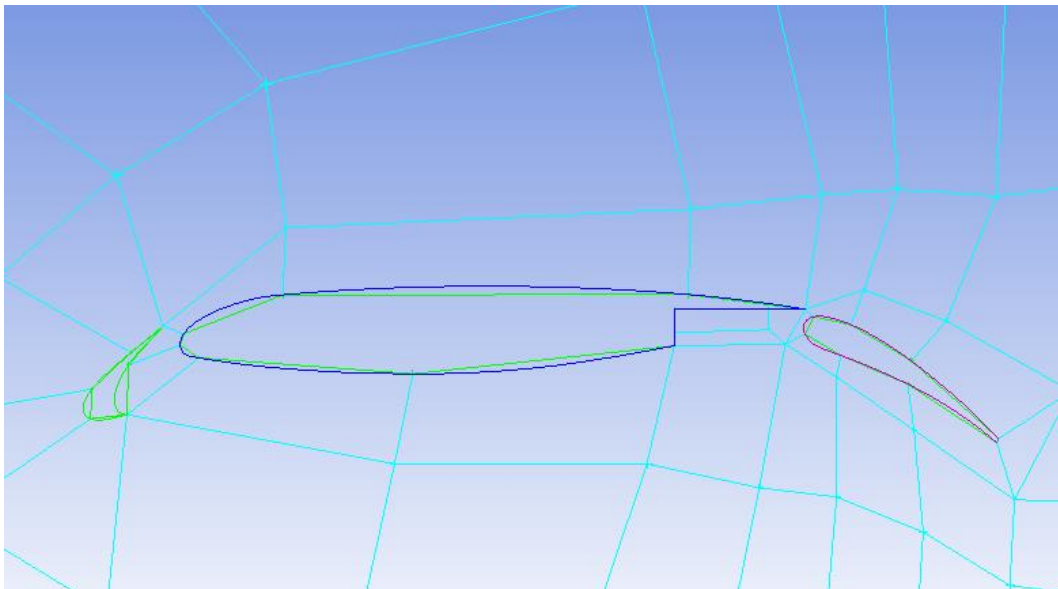
(a). Topology
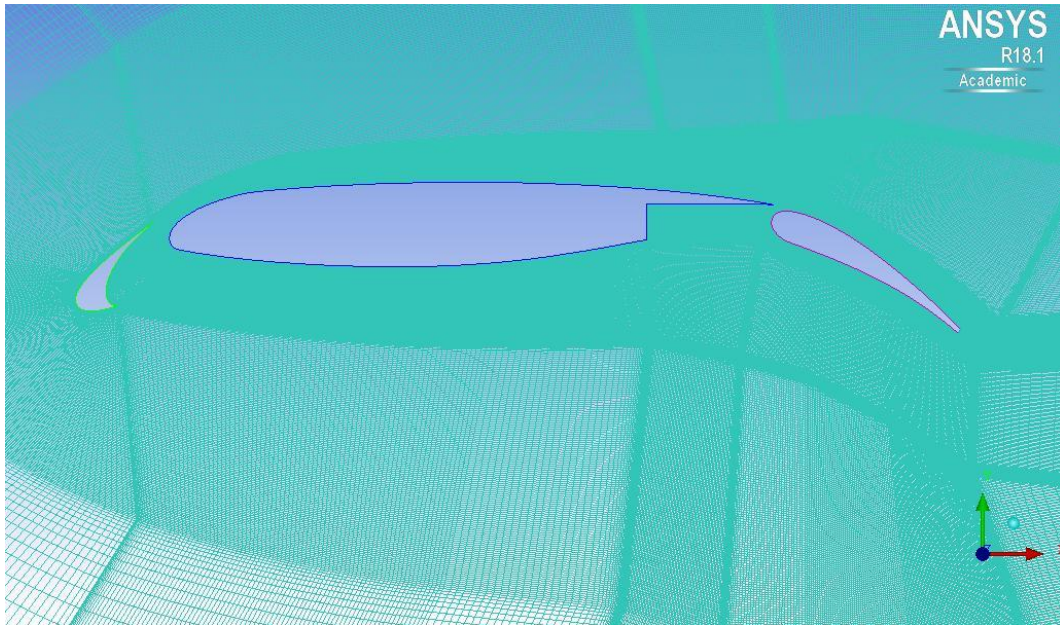
(b). C-mesh

Figure C.11. Mesh

There are totally 423,000 points with 152 points around slat part. There are 5,600 points at slat cove part. In Figure 11, there are totally 764,000 point in the domain with 204 points around slat part. For slat cove part, there are 9,000 points.

Flow filed approach: For this case, we select two turbulence models, the *SST k-ω* and the *transitional k-kl-ω*. The freestream velocity is 57.8 m/s. Reynolds number based on stowed chord is 1.8 million and dynamic viscosity is 1.79e-5. The numerical scheme is presented in Figure C.12.
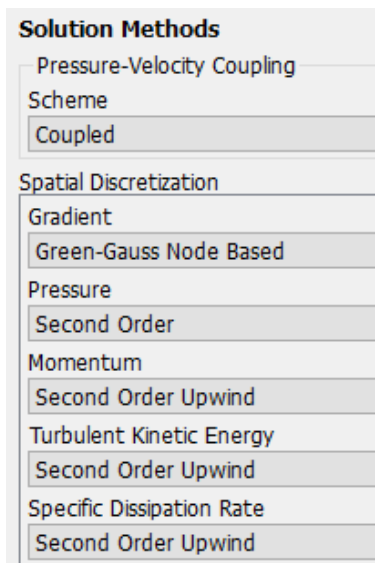
Figure C.12. The numerical scheme

Consider the accuracy of the noise prediction greatly depends on the unsteady flow field calculation and the slat part is complex, we run three types of mesh (see Table C.1) and compare the simulation results to the experimental results first.

Table C.1. Different mesh information

Name	Mesh 1	Mesh 2	Mesh 3
Total Nodes Number	423334	764670	1181670

Flow filed results: The surface pressure coefficient distribution is an important indicator of aerofoil aerodynamic behaviours and we compare it to the experimental data from JAXA wind tunnel test at Mach number equals to 0.17 and angle of attack is 8 degrees, extracted from paper by Li et al (2016).

The first condition is steady flow.
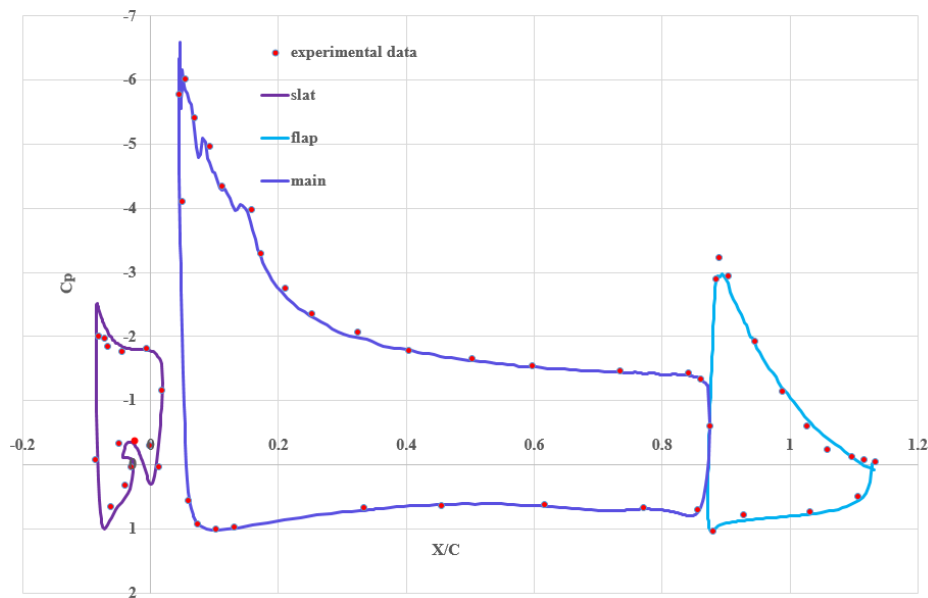
(a). Mesh 1 (*SST k-ω*)
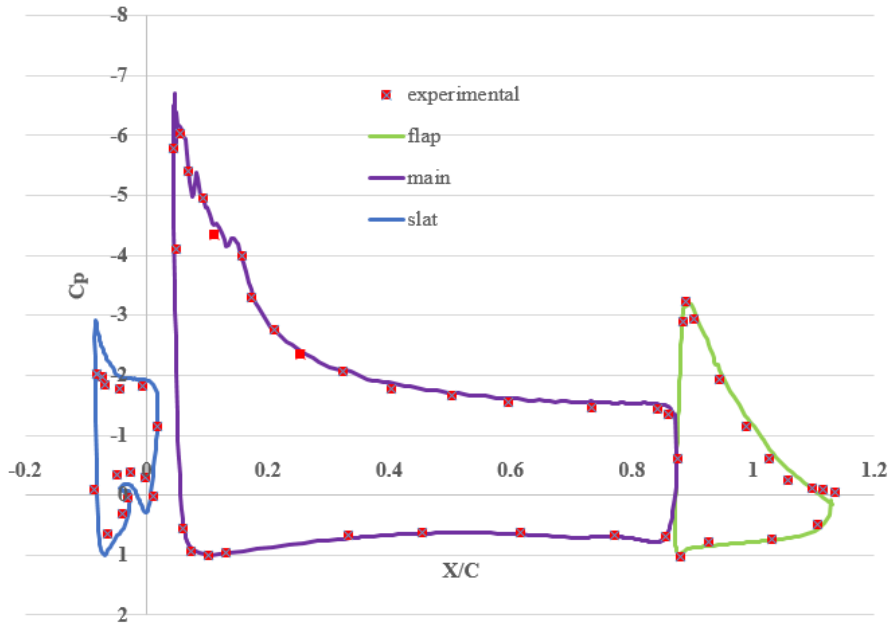
(b). Mesh 1 (*Transitional k-kl-ω*)

Figure C.13. Flow field results

It reveals that CFD simulation results are quite similar to JAXA's wind tunnel results at corresponding angle of attack. In Figure C.13a, MD 30P30N slat part and main part have a great agreement with experimental results. For flap part, between 0.83 to 0.85 parts, experimental results are higher than CFD results and the error is about 8%. In Figure C.13b, the *Cp* of flap part is in good agreement with experimental results and for other two parts, agreements with experimental results are also better.
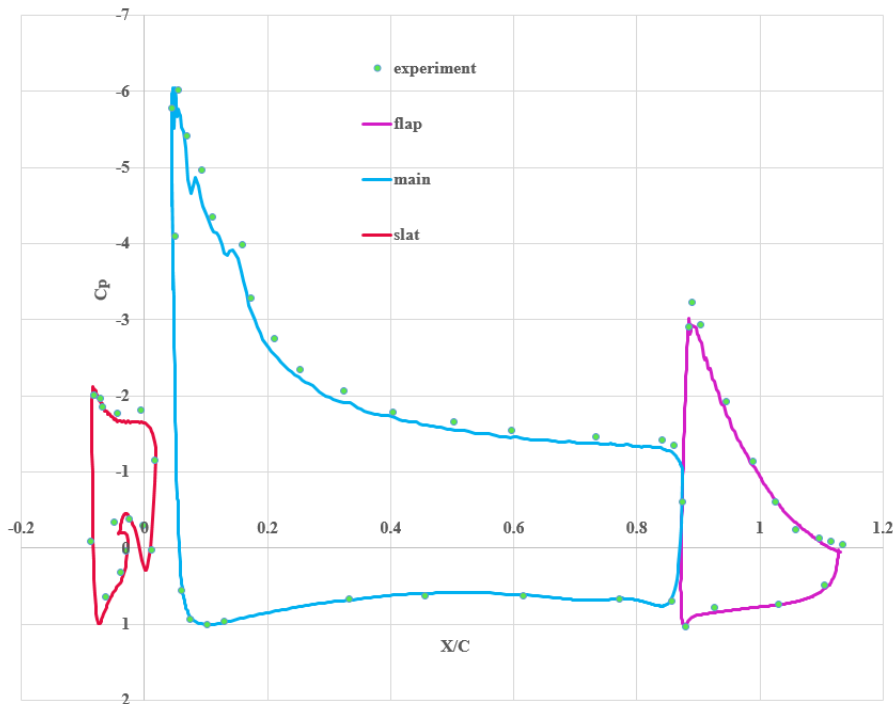
(a). Mesh 2 (*SST k-ω*)
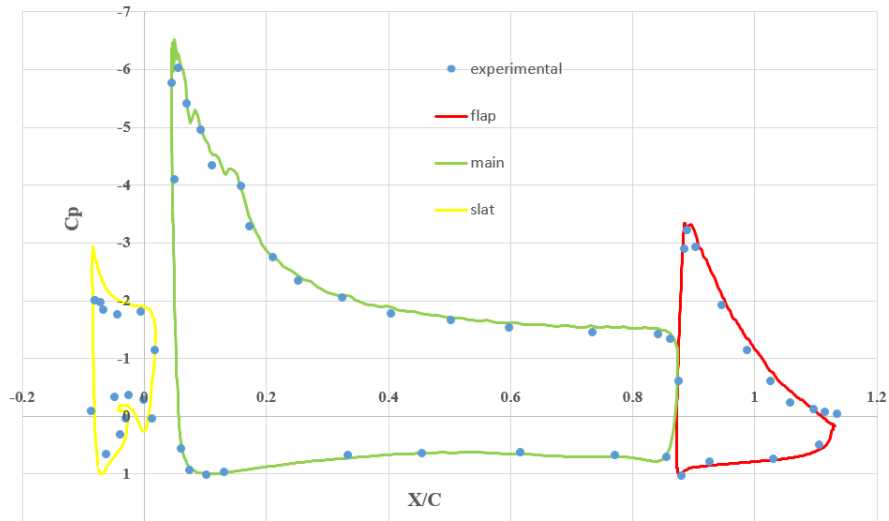
(b). Mesh 2 (*Transitional k-kl-ω*)

Figure C.14. Flow field results

In Figure C.14a, it is clear that compare with CFD results in Figure C.13a, disagreement for the slat part have greatly reduced and for the main part upper surface, experimental results are slightly higher than CFD results and for flap part, there is no distinct difference. For Figure C.14b, the error at the slap part might be lightly decreased compared with Figure C.13b while the rest are the same. It reflects after comparing Figure C.13a and Figure C.13b, increasing points at the slat cove part will improve the accuracy of final prediction for the slat part using *SST k-ω* turbulence model. However, the increased total points in the domain might make CFD results at the main part upper surface section slightly lower than experimental results. For the *transitional k-kl-ω* turbulence method, points increased cannot affect final prediction results.
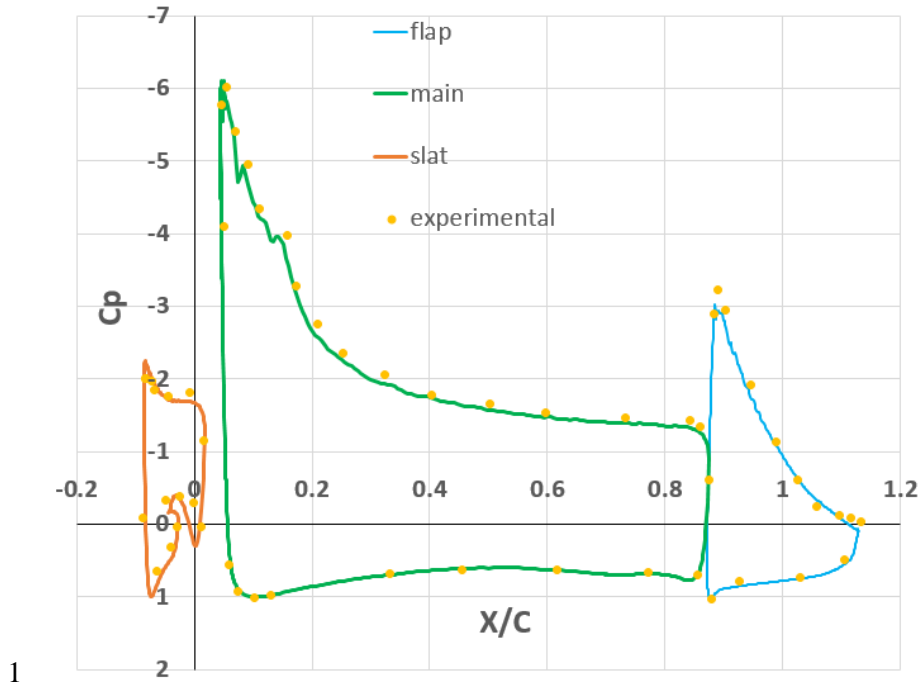
(a). Mesh 3 (*SST k-ω*)
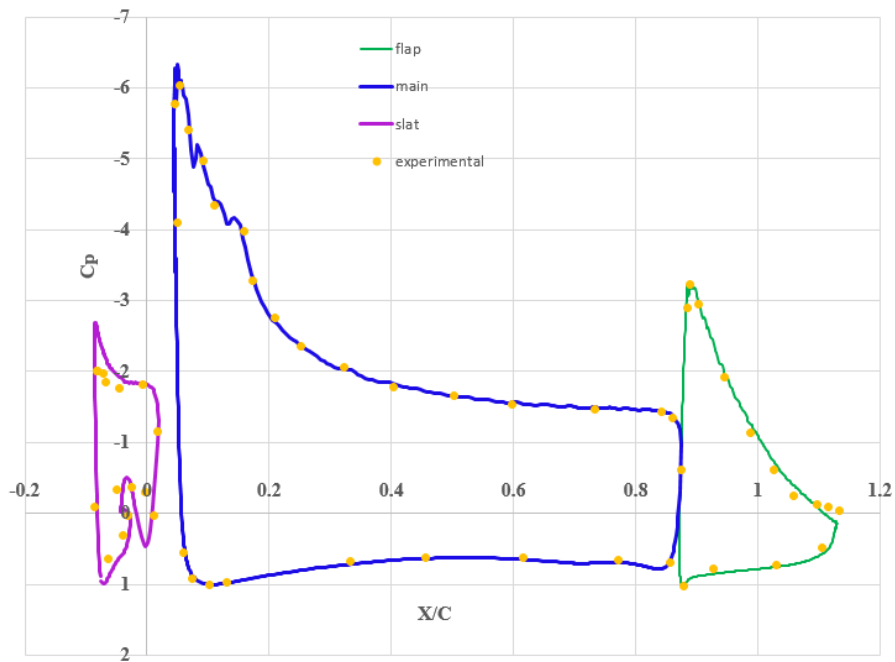
(b). Mesh 3 (*Transitional k-kl-ω*)

Figure C.15. Flow field results

The difference between mesh 2 and mesh 3 is that the grid points of whole domain have increased while

remain the amount of points at slat cove part. It increases the accurate which can reflect from Figure C.15a

compared with results in Figure C.14a. However, the error at flap part is still existed. Besides, from Figure C.15b, the result is the same.

The second condition is the unsteady flow. The simulation time is 12.219251381s with 170,000 time steps and time step size is 7.19e-4. Mesh 3 is used for unsteady flow simulation. The lift coefficient value for steady state flow simulation result is 2.90. Table C.2 summarizes lift coefficient characteristics for unsteady flow simulation by averaging over nearly 10,000 time steps.

**Table. C.2.** Mathematical characteristics of lift coefficient

Maximum Value	2.905
Average Value	2.89
Minimum Value	2.87

It can clearly see that average lift coefficient *Cl* value for unsteady state flow simulation is close to lift coefficient *Cl* value for steady state flow simulation. Therefore, Detached Eddy Simulation (DES) can be a reliable method to predict lift coefficient.

Figure C.16 and Figure C.18 show the contour of mean streamwise (U) and vertical (V) velocity for 8-degree AOA, extracted from time-accurate simulations by averaging 10,000 time steps. Figure C.17 and Figure C.18 display the contour of streamwise and vertical velocity for 8-degree AOA from PIV measurements and computational results by using CFL3D code (Khorrami et al., 2004). The ranges of velocity value in Figure C.16 and Figure C.18 are scaled based on ranges from PIV measurements published by Khorrami et al (2004).

The streamwise velocities at slat leading edge and trailing edge are accurately predicted by the computations (See dark red contour in Figure C.16). Besides, high negative velocities at cove part can be observed. This is imposed by the recirculating flow field. Meanwhile, compare two computational results from Figure C.16 and Figure C.17, it is clear that for both simulation results, the notable difference between measured and predicted velocities occurs at slat leading edge part. The streamwise contour shows that significant positive velocities penetrate towards cove wall. However, a clear vortex exists near slat leading edge in Figure C.16. It might indicate that turbulent flow is not fully simulated here.
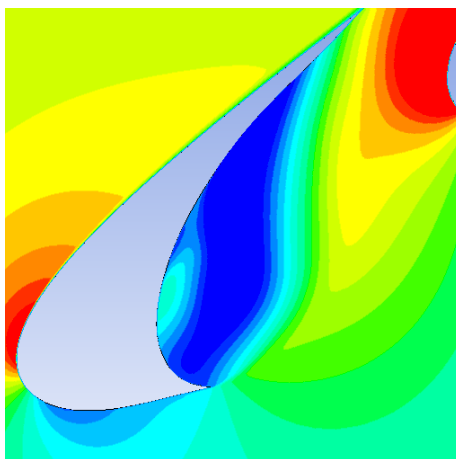
For mean vertical velocity, compared with PIV measurement results, the computed vertical velocity contour (Figure C.18) shows the proper acceleration at main foil leading edge and further into slat gap.
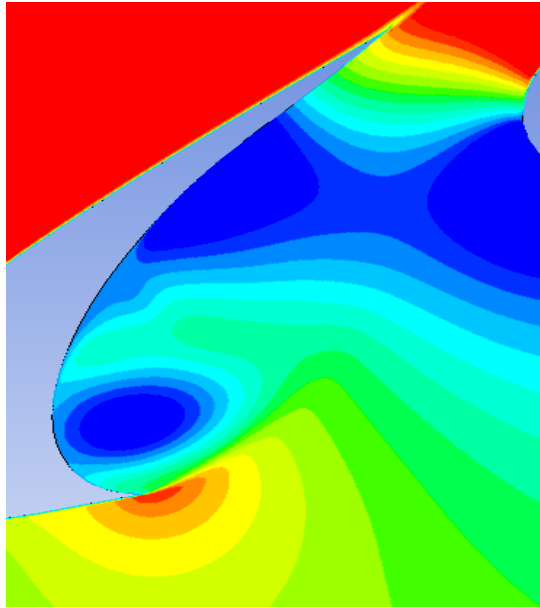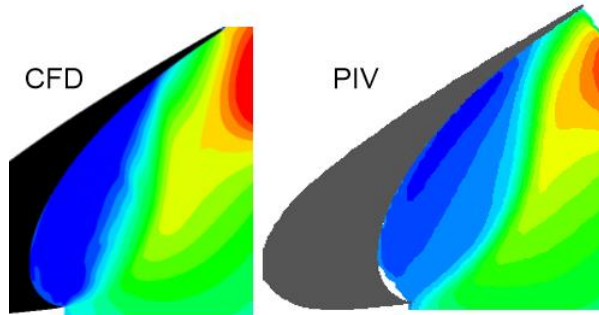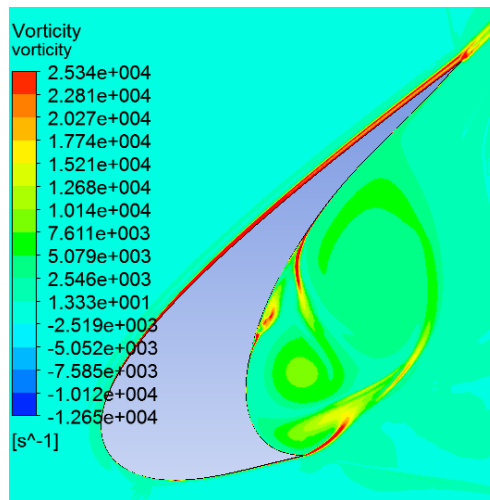
Figure C.16. Mean streamwise velocity
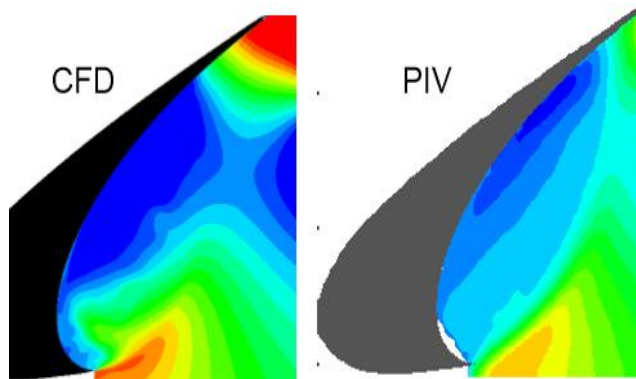
Figure C.17. Averaged streamwise velocity field for 8-degree AOA from CFD and PIV (Khorrami et al., 2004)
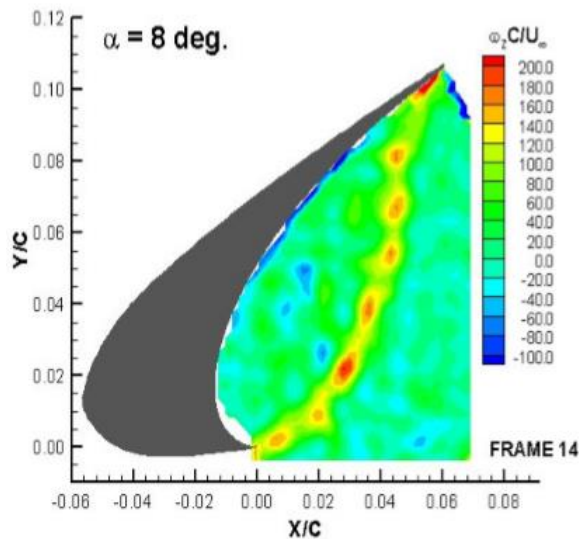

Figure C.18. Mean vertical velocity

Figure C.19. Averaged vertical velocity field for 8-degree AoA from CFD and PIV (Khorrami et al., 2004)

**Figure C.20.** Vorticity magnitude

Figure C.21. Measured Instantaneous vorticity field at 8-degree AoA (Khorrami et al., 2004)

The instantaneous vorticity plot from the 8-degree simulation is presented in Figure C.20, roughly corresponding to 9900 in the sampled record of 10,000 time steps. Figure C.21 shows the PIV measurement result captures individual vortices and their upward convection by the shear layer. The maximum and minimum values

140

of vorticity (Figure C.20) are scaled based on the corresponding value in Figure C.21. Compared with PIV results, vortex rolling-up is not seeing and the reattachment point is moving far away from slat trailing edge. For once-through flow, the time is 60 (the domain length) divide 57.8 (freestream velocity) and the value is roughly 1.04s. Simulation time for this unsteady flow is 12.223 seconds, which means during simulation time, 11 times through-flow had completed, and it indicates that time is enough. Therefore, the potential reason is for larger time step size. In general, both mean and instantaneous PIV measurements indicate that pattern of vortex structure at slat cove part is more chaotic than simulated flow results.

Consider the simulation results of the unsteady flow in the slat cove area are not good enough to match well with the experimental result. Therefore, we decide to use the inverse engineering approach to obtain the time-domain aeroacoustic data. The experimental data of the acoustic spectrum at the slat cove area can be obtained from the published documents (Lockard and Choudhari, 2009; Li et al., 2017). The experimental results reveal that the value of the Strouhal number based on the slat chord length falls within the range of $(1, 5)$, therefore, in Simulink, the sampling frequency is at least 4,000 Hz and the cancellation performance is presented in Figure C.22.
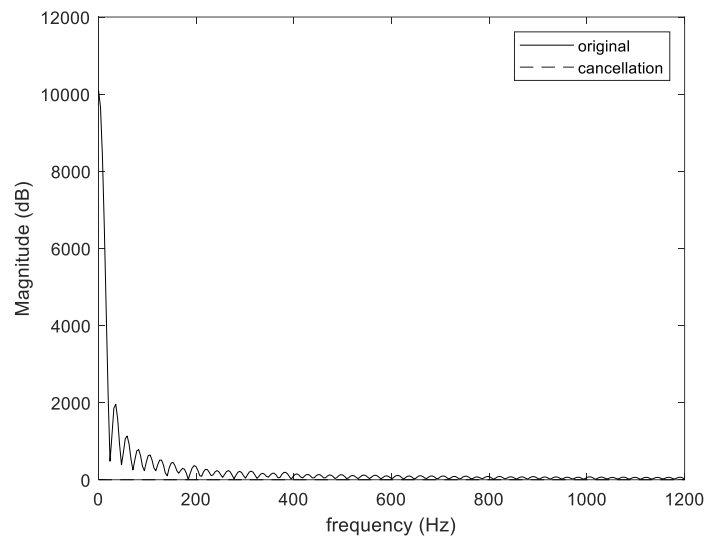
Figure C.22. Cancellation performance